Combined Two-Dimensional Electron Gas and Artificial Spin Ice Structures
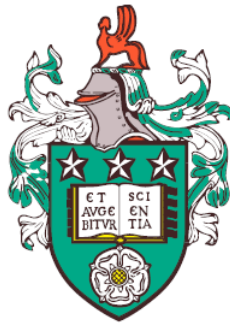
Susan Tania Riley

School of Electronic and Electrical Engineering

The University of Leeds

Submitted in accordance with the requirements for the degree of Doctor of Philosophy

June 2016

Acknowledgements

I would like to start by thanking my supervisors Prof. John Cunningham and Prof. Chris Marrows for all the invaluable support and guidance they have provided throughout this project. I am also very grateful to Prof. Edmond Linfield for all his support and the infectious enthusiasm he has shown towards my work. I would also like thank Prof. Giles Davies, Dr. Gavin Burnell and Dr. Chris Wood for the advice they have provided throughout the project.

An enormous amount of gratitude is owed to both Dr. Mark Rosamond and Dr. Sophie Morley for their assistance with sample fabrication and their numerous helpful discussions. No matter how many times I've found a novel method of annihilating a sample, they have always been there to (sometimes literally) help pick up the pieces.

I thank Dr. Lianhe Li for providing all the semiconductor wafers that were used in this thesis. I am also very grateful to Dr. Mannan Ali, Dr. Divyang Mistry, Dr. Joe Batley and Dr. Nick Porter for all the practical guidance they have provided in the lab.

Being welcomed so warmly into both the CM and IMP groups has played a key part in why I have enjoyed my time in Leeds so much. I thank Philippa, Rowan, Dan, Jo, Nathan, May, Mark, Ales, Helen, Alex, Dave, Chris, Matt and Burnie, to name but a few, for helping to fill my spare time with numerous pub trips, quizzes, pool games and much more. I also thank Robert and Fatma for so frequently turning my desk into something resembling a picnic table, as well as for the unbeatable office atmosphere.

I must also thank my parents for without their unwavering support I would not be in the position that I am today, and for that I am truly grateful. And last, but by no means least, I would like to thank Neil for all the love, support, and encouragement he has always provided during our time together.

Abstract

This thesis presents research into the electron transport properties of hybrid semiconductor / ferromagnetic structures. Periodic arrays of ferromagnetic stripes and artificial spin ice (ASI – arrays of geometrically frustrated nanomagnets) are patterned atop GaAs-AlGaAs wafers containing a two-dimensional electron gas (2DEG), and resistance measurements are performed under cryogenic temperatures and applied magnetic fields.

The effects of piezoelectric strain on the transport properties of 2DEGs are investigated by comparing the resistances of magnetic and non-magnetic stripes patterned atop a 2DEG. Piezoelectric strain manifests itself as electric commensurability oscillations in the longitudinal resistance of a 2DEG. These oscillations are independent of temperature and are caused by stress acting upon the edges of the stripes.

Transport measurements of combined 2DEG / ASI structures reveal the first observations of commensurability oscillations (COs) caused by ASI in the longitudinal resistance of a 2DEG. These oscillations are periodic on length-scales commensurate with the length of the individual nanomagnets that form the ASI. The COs are temperature dependent, but independent of the angle of applied magnetic field for our particular samples. Models based upon a Fourier analysis of Maxwell's equations help explain our results.

This thesis also addresses the thermally-activated magnetization dynamics behaviour of ASI. We show exactly how the proportion of each vertex type changes as an ASI is heated, and moves from an ordered state to a ground state. We compare

the results from two different alloys of PdFe and three different lattice spacings. The way in which arrays of ASI change to a ground state is dependent upon the material composition of the ASI, with little dependence upon the period of the ASI. A material with a large magnetization requires a higher temperature to cause any magnetic spins to flip, after which the ASI abruptly changes from an ordered state to a ground state.

List of abbreviations

2DEG	Two-dimensional electron gas
AFM	Atomic force microscope / microscopy
ASI	Artificial spin ice
CO	Commensurability oscillation
EBL	Electron-beam lithography
LED	Light-emitting diode
MBE	Molecular beam epitaxy
MFM	Magnetic force microscope / microscopy
Py	Permalloy
QHE	Quantum Hall effect
RPM	Rotations per minute
SdH	Shubnikov-de Haas
SEM	Scanning electron microscope / microscopy

Contents

Chapter 1

Introduction

1.1 Motivation

This thesis combines two distinct areas of physics: two-dimensional electron gases (2DEGs), a branch of semiconductor physics; and artificial spin ice (ASI), a branch of magnetism.

2DEGs, discovered in 1948 [1], are systems of free electrons that are strongly confined to two dimensions. They have proven to be a rich source of fundamental physical phenomena unobtainable in systems without confinement, such as the quantum Hall effect [2] and the fractional quantum Hall effect [3–5]. Four scientists have been awarded Nobel prizes following discoveries made using 2DEGs, and their use in transistors makes them indispensable to many technological devices used today.

In contrast to 2DEGs, the study of ASI is an up-and-coming area of research, having been invented barely ten years ago [6]. An ASI is an array of lithographically-patterned, interacting nanomagnets, geometrically arranged in a way that causes frustration – a phenomenon that occurs when it is impossible to minimise the energies between all pairwise interactions simultaneously. Like water ice, from which ASI gets its name, ASI violates the third rule of thermodynamics. This results in a non-zero entropy at a temperature of absolute zero, and a degenerate ground state [7]. Spin ice is of further interest to researchers with the discovery that magnetic monopole

defects can arise in these materials [8]. These quasiparticles occur when there is an imbalance of magnetic charge at a point where multiple nanomagnets meet, and this has potential applications in magnetricity – a form of electricity that utilises the flow of magnetic monopoles rather than electrons [9].

Research has previously been conducted on the transport properties of combined 2DEG / ferromagnetic stripe structures [10, 11]. They uncovered new phenomena relating to commensurability oscillations in the longitudinal resistance of the 2DEG, caused by the periodic nature of the magnetic field emanating from the ferromagnetic stripes. This work is also of interest owing to the potential use of these structures in applications such as magnetic storage devices [12] and magnetic field sensors [13]. This thesis extends the field of hybrid 2DEG / ferromagnetic structures to include combined 2DEG / ASI structures.

1.2   Thesis Outline

The broad aims of this thesis are twofold. First, we aim to determine how the transport properties of 2DEGs are affected by magnetic fields caused by ASI. The second objective is to enhance our understanding of the thermally-activated magnetization dynamics of ASI arrays – to ascertain to what extent the lattice spacing and material choice affect the magnetic configurations as ASI is heated.

Chapter 2 provides a brief overview of the key theoretical concepts and background material required to understand the results discussed in later chapters. It commences with a description of 2DEGs and their formation before moving on to derive equations related to the transport properties we will later discuss. There then follows a description of ASI and a review of the developments made in its ten-year history. Finally, we discuss the research that has already been undertaken in the field of combined 2DEG / ferromagnetic structures to provide a context into which this work can be placed.

Chapter 3 discusses the main experimental techniques used in this thesis.

Chapter 4 discusses the preliminary transport measurements undertaken on combined 2DEG / ferromagnetic structures. Here we show the differences that can be made on the transport properties by measurements with or without illumination, and we also provide an in-depth analysis on the role that piezoelectric strain can potentially have on our results.

Chapter 5 focuses on the transport measurements obtained on combined 2DEG / ASI structures. We show and discuss the first observed commensurability oscillations caused by ASI.

Chapter 6 discusses the thermal measurements undertaken on ASI on SiO_2 wafers. We show, for the first time, how the proportion of each vertex type changes as the ASI is heated as it progresses from an ordered to a ground state array. We also compare the results obtained using different materials and lattice spacings.

Finally, chapter 7 summarises this thesis and offers suggestions for further work.

Chapter 2

Background Theory

2.1 Two-Dimensional Electron Gases (2DEGs)

2.1.1 2DEG Formation in a GaAs/AlGaAs heterostructure

A two-dimensional electron gas (2DEG) is a thin sheet of electrons whose motion is strongly confined to a two-dimensional plane and forbidden in the third dimension perpendicular to the sheet [14]. They are commonly found in semiconductor heterostructures, graphene [15] and MOSFETs (metal oxide semiconductor field effect transistors) [16].

2DEGs were first introduced in 1948 by Shockley and Pearson during the production of the silicon MOSFET [1]. When a voltage is applied to a metal electrode fabricated atop a silicon oxide insulating layer it results in band bending at the boundary between the SiO_2 and the p-type doped Si substrate, creating an inversion layer of charge carriers which forms the 2DEG. This discovery paved the way for the modern day transistor but this material system was not ideal for the study of quantum mechanical effects owing to the strong Coulomb scattering by charged impurities at the SiO_2-Si interface [17–19]. Advances in Molecular Beam Epitaxy (MBE) growth techniques, allowing the fine-tuning of the growth process of crystalline semiconductors down to an atomic scale, has enabled the production of consistently high quality,

high mobility 2DEGs at the interfaces of type III-V semiconductor heterostructures.

The first observation of a 2DEG at the interface of a GaAs-AlGaAs heterostructure semiconductor was made in 1979 [20]. In a GaAs-Al$_x$Ga$_{1-x}$As heterostructure, where x is typically 0.3 [21], Al atoms in AlGaAs replace some of the Ga atoms in the crystal. GaAs-AlGaAs has remained a popular choice of material for the study of 2DEGs owing to GaAs and AlGaAs having very different band gap energies ($\sim$1.4eV for GaAs but $\sim$2eV for AlGaAs) which allows a 2DEG to form at the interface between the two layers, whilst at the same time GaAs and AlGaAs also have a very similar crystal structure but with an almost identical lattice spacing that minimizes electron scattering and enables high electron mobilities of the order 10^6 cm^{2}V^{-1}s^{-1} to be reached [14]. Figure 2.1 shows how technological advances have allowed the electron mobility obtainable in a 2DEG to increase significantly over time, with an improvement of three orders of magnitude between 1978 and 2007.

Figure 2.2 shows how a 2DEG is formed in a semiconductor heterostructure. When two materials with different Fermi energies are combined, as is the case for GaAs and AlGaAs, n-type dopant electrons move from the conduction band of the material with the higher potential energy into the conduction band of the other material in order to equalize the Fermi energies. For GaAs and AlGaAs, electrons move from AlGaAs to GaAs. This electron migration results in each material becoming charged: AlGaAs becomes positively charged whereas GaAs becomes negatively charged. The charge imbalance induces an internal electric field which opposes any further movement of charge carriers and equalizes the Fermi energies of the two materials. The conduction and valence bands of both materials bend to compensate for the motion of the electrons, and the conduction band dips below the Fermi energy to form a quantum well. It is in this quantum well, located at the interface of GaAs and AlGaAs, that the pool of electrons known as a 2DEG accumulates. The electrons remain trapped in the quantum well owing to Coulomb attraction preventing the electrons moving into the GaAs and band edge discontinuity preventing electrons moving into the AlGaAs [23].
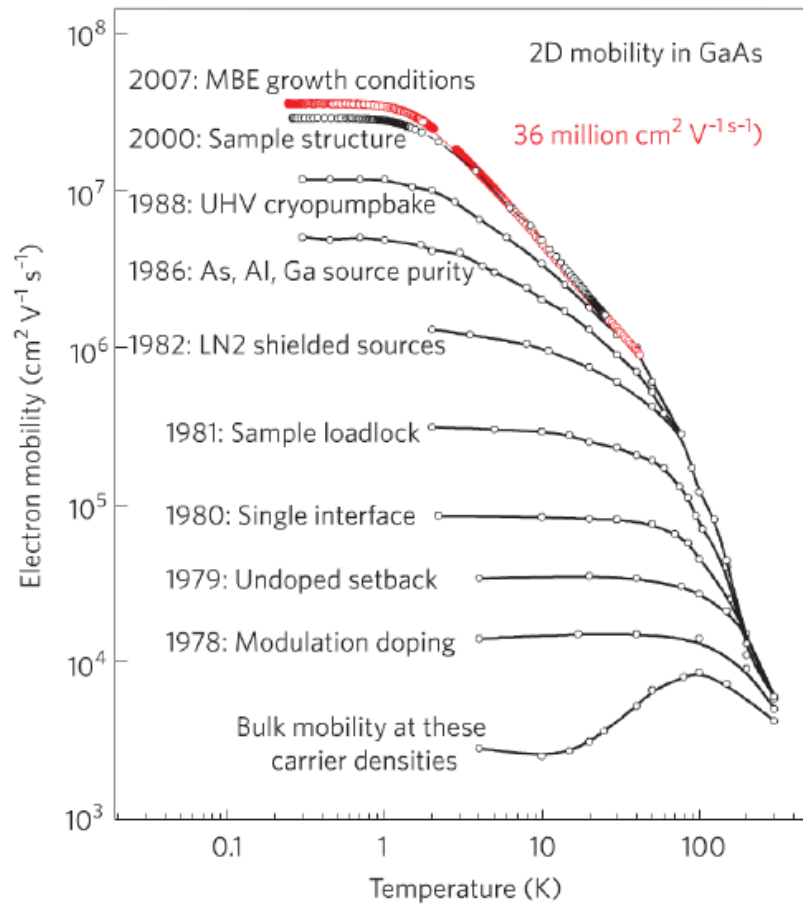
Figure 2.1: The progress made in electron mobility in 2DEG since 1978, along with the key technological advances that enabled each improvement [22]
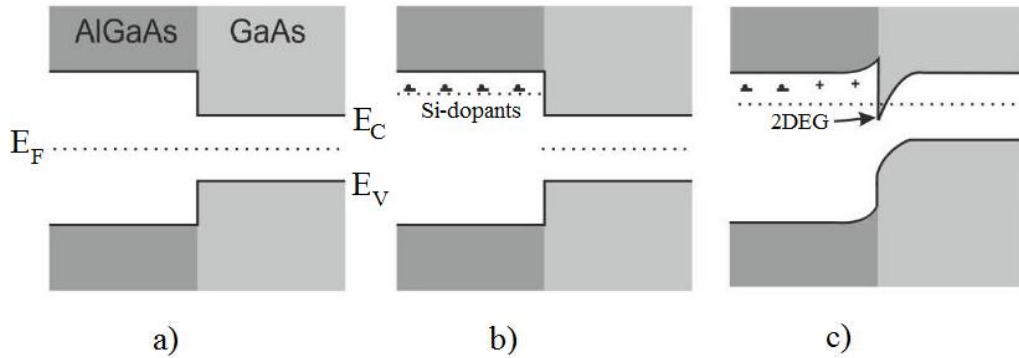
Figure 2.2: The formation of a 2DEG in a GaAs-AlGaAs semiconductor heterostructure [24]. Part a) shows the band diagram that would occur if the AlGaAs was undoped. In part b), the AlGaAs is n-type doped with Si atoms and the Fermi energies of the two materials are unequal. In part c), electrons have travelled from the AlGaAs conduction band to that of the GaAs to equalize the Fermi energies, resulting in the conduction and valence bands bending. A 2DEG forms within the quantum well in the region below the Fermi energy at the interface of the two materials.

The structure of a typical GaAs-AlGaAs wafer is shown in figure 2.3. Using MBE, a high quality GaAs layer is grown upon a GaAs substrate. An AlGaAs spacer layer is then deposited atop this GaAs layer and it is at this interface that the quantum well containing the 2DEG is formed. Doped AlGaAs is the next layer to be grown, with Si donor atoms integrated into the AlGaAs layer using a modulation doping method first introduced in 1978 [25]. It is from these Si atoms that the free electrons accumulating in the 2DEG originate, while the spacer layer reduces the ionized impurity scattering caused by the remaining free electrons in the doped layer [26]. Finally, a thin GaAs capping layer is grown. The purpose of this layer is twofold: to prevent the AlGaAs from being exposed to air and oxidising, and to allow further deposition of material upon the 2DEG wafer without affecting the doped AlGaAs layer.
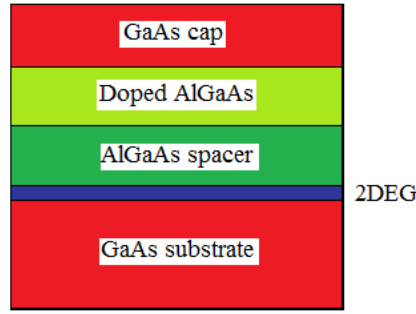
Figure 2.3: Schematic of a 2DEG grown in a GaAs-AlGaAs wafer using molecular beam epitaxy (MBE).

2.1.2 Landau Levels

The energy of an electron located in the conduction band of a semiconductor, when no electric field is present, is

$$E(k) = \frac{\hbar^2 k^2}{2m^*},$$ (2.1)

where k is Fermi wavevector, $(\hbar k)$ is the crystal momentum, and m^* is the effective mass of the electron. In GaAs, the effective mass of the electron has a value of $0.067 m_e$, where m_e is the mass of an electron. This results in a continuous spectrum of energy for the electrons in a semiconductor so, in the absence of a magnetic field and at zero temperature, the density of states is also continuous and all states up to the Fermi energy are filled [14].

However, when a 2DEG is subjected to an applied perpendicular magnetic field B, the electrons are made to move in circular orbits by the Lorentz force. This prevents the free movement of electrons and causes the energy spectrum to become discrete with energy levels at values of [14]

$$E_n = (n - 1/2)\hbar\omega_c,$$ (2.2)

where n is an integer representing the band number. The cyclotron frequency, ω_c is given by

$$\omega_c = \frac{eB}{m^*}.$$ (2.3)
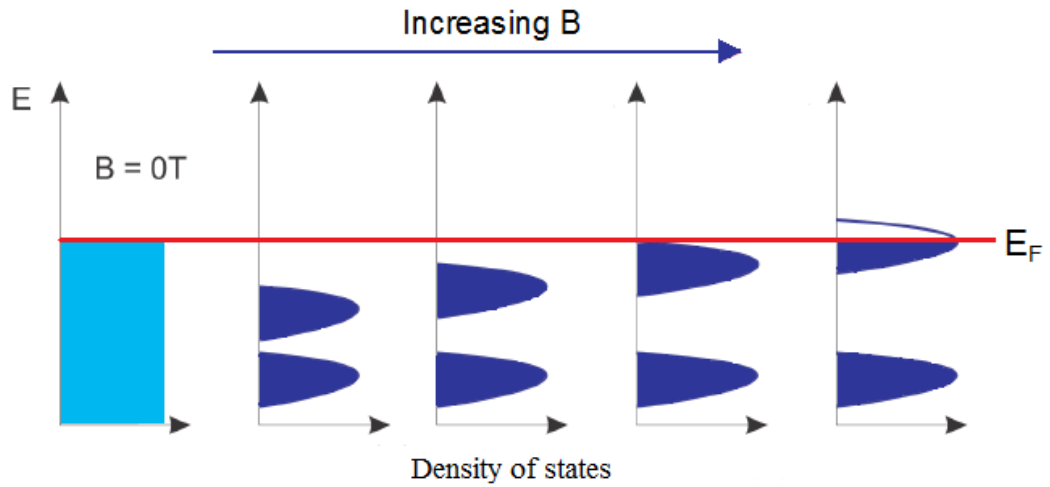
Figure 2.4: The formation of Landau levels in an increasing magnetic field [27]. In the absence of a magnetic field, electrons in a 2DEG occupy all states up to the Fermi energy but, when a magnetic field is applied perpendicular to a 2DEG, the states split into discrete layers called Landau levels. The distance between Landau levels is directly proportional to the magnetic field strength.

These discrete energy levels are called Landau levels. Energy states outside the Landau levels are localised so no conduction occurs, and hence a current can only flow in the extended states within Landau levels [27]. For a perfect system with no scattering, each Landau level is a δ-function with a single energy. However, a 2DEG will contain impurities and defects which will scatter electrons and lead to the Landau levels broadening into non-δ-like functions.

Figure 2.4 demonstrates the formation of Landau levels and the effects of an increasing magnetic field. It can be seen from equations 2.2 and 2.3 that the energy of a Landau level is directly proportional to the magnetic field. Therefore, doubling the applied magnetic field also doubles the energy gap between Landau levels so they spread apart.

2.1.3 The Quantum Hall Effect

When an external magnetic field is applied perpendicular to an electric current flowing through a conducting material, it induces a voltage transverse to the current. This is called the Hall voltage and the effect, discovered in 1879, is the Hall effect [28].

The quantum Hall effect (QHE) is the quantum mechanical version of this classical Hall effect. In the presence of low temperatures and high magnetic fields, the Hall resistance in a 2DEG is precisely quantized with values of h/Ne^2, regardless of the material properties of the conductor such as the sheet density or mobility of electrons [2], where N is an integer representing the number of filled Landau levels. This discovery allowed the fine structure constant to be calculated to previously unprecedented levels of accuracy, as well as providing a definition of the ohm only in terms of Planck's constant and the charge of an electron [29].

The QHE results from Landau levels formed in the presence of a perpendicular magnetic field; when the Fermi energy is between Landau levels the Hall resistance remains unchanged due to the lack of conduction in this area. In plots of Hall voltage (or resistance) against field, the QHE manifests itself as a series of plateaus embedded in an otherwise sloped line with a constant positive gradient, as shown in figure 2.5. This graph can be used to determine properties of the semiconductor such as the sheet density. The Hall voltage, V_H, across a conductor of thickness d, in terms of the current I, magnetic field B, carrier density n, and electron charge e is

$$V_H = \frac{IB}{ned}. \tag{2.4}$$

For a two-dimensional system, the sheet density, n_s, is the product of the carrier density and thickness

$$V_H = \frac{IB}{n_s e}. \tag{2.5}$$

which leads to the sheet density of a 2DEG in terms of the Hall voltage and applied field

$$n_s = \frac{IB}{V_H e}. \tag{2.6}$$
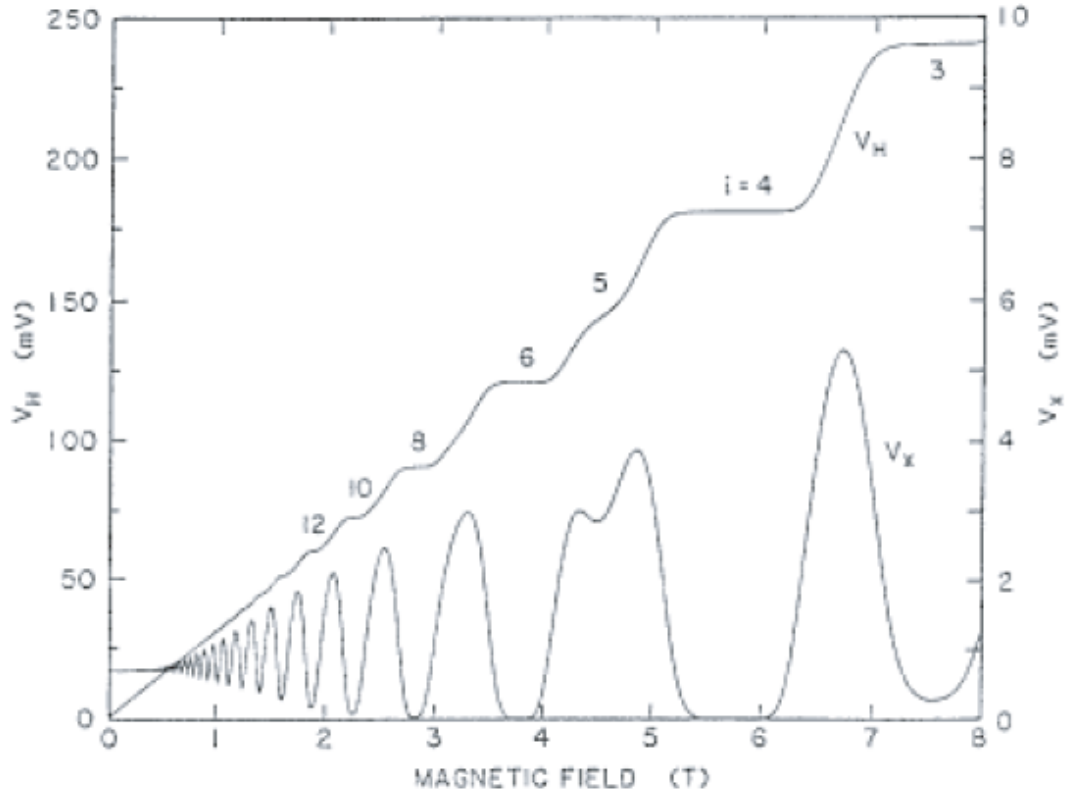
Figure 2.5: The Quantum Hall effect and Shubnikov-de Haas oscillations shown here [21] are obtained through resistance measurements of a 2DEG at cryogenic temperatures under the influence of an applied magnetic field. The Hall voltage is obtained through taking the resistance of two terminals across the current, whereas the longitudinal resistance is obtained from resistance measurements using Ohmic contacts parallel to the direction of the current.

2.1.4 Electron Transport Properties

The mobility of electrons in a 2DEG can be calculated using Shubnikov-de Haas (SdH) oscillations. SdH oscillations form in the longitudinal resistance, R_L, of a 2DEG when it is under the influence of an applied perpendicular magnetic field. The electrical conductivity, σ, which is also the inverse of ρ, the resistivity, of a 2DEG is the product of the sheet density, charge e, and mobility μ:

$$\sigma_L = n_s e \mu = \frac{1}{\rho_L}, \tag{2.7}$$

where we use the standard definition of resistivity

$$\rho = \frac{RA}{L}. \tag{2.8}$$

Since we are dealing with a two-dimensional system, the resistivity is the resistance per square, so with the width of the structure, W, and the distance between contacts of L:

$$\rho_L = \frac{R_L W}{L}. \tag{2.9}$$

For a two-dimensional system both the resistance and the resistivity have identical units, ohms [21].

Upon combining and rearranging equations 2.7 and 2.9, we form an expression for the mobility

$$\mu = \frac{L}{n_s e R_L W}. \tag{2.10}$$

From the mobility and the sheet density, the electron mean free path, l, can be calculated. The mean free path is defined as the average distance an electron travels before being scattered by an obstacle such as an impurity or defect in the material

$$l = v_F \tau, \tag{2.11}$$

where v_F is the Fermi velocity, a function of the Fermi energy, and τ is the scattering time. The Fermi energy, E_F, can be expressed as

$$E_F = \frac{1}{2} m^* v_F^2, \tag{2.12}$$

while the Fermi energy can also be written in terms of the Fermi wave vector, k_F

$$E_F = \frac{\hbar^2 k_F^2}{2m^*},$$ (2.13)

where k_F is dependent upon the sheet density

$$k_F = \sqrt{2\pi n_s}.$$ (2.14)

If we combine and rearrange equations 2.12 and 2.13, we obtain this expression in v_F

$$v_F = \frac{\hbar k_F}{m^*}.$$ (2.15)

To determine the scattering time, we have to consider the force the electrons experience as a result of the applied field, along with the law of conservation of momentum. The electrons experience a force, F, due to an electric field, $\mathcal{E}$ of

$$F = -e\mathcal{E}.$$ (2.16)

Through equating the electron's momentum due to the applied field with the momentum due to its mass and velocity we obtain

$$-e\mathcal{E}\tau = m^* v_d$$ (2.17)

$$\Rightarrow v_d = -\frac{e\mathcal{E}\tau}{m^*},$$ (2.18)

where v_d is the drift velocity. By using the relationship between μ, v_d and $\mathcal{E}$ and equation 2.18, we can then produce a formula for the scattering time:

$$\mu = |\frac{v_d}{\mathcal{E}}|,$$ (2.19)

$$\Rightarrow \tau = \frac{m^* \mu}{e}.$$ (2.20)

Finally, we obtain an expression for the electron mean free path by substituting equations 2.15 and 2.20 into 2.11:

$$l = \frac{\hbar \mu k_F}{e} = \frac{\hbar \mu \sqrt{2\pi n_s}}{e}.$$ (2.21)

2.2   Spin Ice

2.2.1   Frustrated Systems

Geometrical Frustration

A frustrated system occurs when the topology of a structure prohibits the simultaneous satisfaction of all pair-wise interactions. In the general case, an interaction is considered satisfied when it results in its lowest possible energy state. For a system consisting of several interacting magnets, satisfaction arises when magnets converging at a point are arranged exclusively with opposite poles facing one other.

When considering a scenario in which there are never more than two magnets meeting at a point, it is trivial to arrange them in a manner which facilitates north-south pole interactions and avoids frustration. However, when three magnets coincide at a vertex there are, excluding rotational symmetries, four possible combinations (three north poles meeting; three south poles; two north poles and one south pole or one north pole and two south poles) and three simultaneous pair-wise interactions to satisfy. Since forming an arrangement in which two like-poles do not interact is unavoidable, the three-magnet structure is inherently frustrated.

If we extend this system to form an array of interlinked three-magnet vertices it results in a long range disorder with a residual ground state entropy that remains even at the temperature limit of absolute zero. Therefore, we create a system with a macroscopically degenerate ground state, breaking the third rule of thermodynamics.

Frustration in Water Ice

Water ice is the classic example of frustration occuring in nature. After experiments conducted on water ice from 1933 discovered a non-zero entropy indicative of frustration [7, 30], Pauling devised an explanation [31] in terms of the hydrogen bond positions within the tetrahedral structure of water ice and their relation to the 'ice rules' first proposed by Bernal and Fowler [32].

Water ice has a structure consisting of interlinked tetrahedra, each containing

four hydrogen ions (protons) bonded to a central oxygen ion, shown in figure 2.6. The frustration arises through the interactions between the four positively charged protons. For each individual proton it is energetically favourable for it to be positioned close to the negatively charged oxygen ion. However, due to the strong repulsive forces that would be encountered through all the protons being positioned in this manner, it is favourable for the system as a whole to have a proton configuration comprising two short range covalent bonds and two long distance hydrogen bonds. This compromise of a two-in/two-out formation is known as the 'ice rules', and produces the lowest possible energy state for this structure.
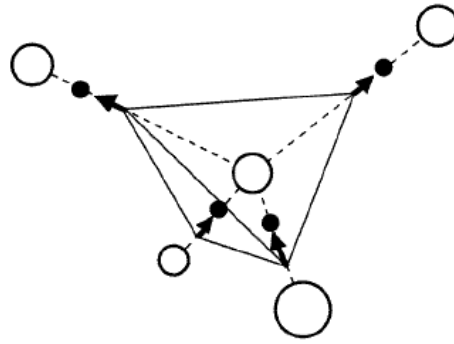
Figure 2.6: The structure of water with the large white circles representing oxygen ions and small black circles representing the protons [33]. The arrows directed towards/away from the centrally located oxygen ion represent the covalent/hydrogen bonds, respectively, between that oxygen ion and its nearest hydrogen ions, hence demonstrating the two-in/two-out formation governed by the ice rules.

2.2.2 Spin Ice

In 1997, the pyrochlore $Ho_2Ti_2O_7$ was found to be the first material with ferromagnetic interactions to exhibit geometrical frustration [34]. This discovery prompted a range of experiments studying the properties of the family of rare earth oxide materials belonging to the type $R_2T_2O_7$ with R being a rare earth metal such as dysprosium [35] or holmium [36], and T a transition metal such as titanium [37] or tin [38].

Figure 2.7: A comparison of the structures of water ice and spin ice [40]. Both materials require a two-in/two-out formation to obtain the ground state.

With a structure analogous to water ice, from which it takes its name, pyrochlore spin ice consists of rare earth metal ions positioned at the vertices of interlinked tetrahedra connected at their corners, surrounding an oxygen io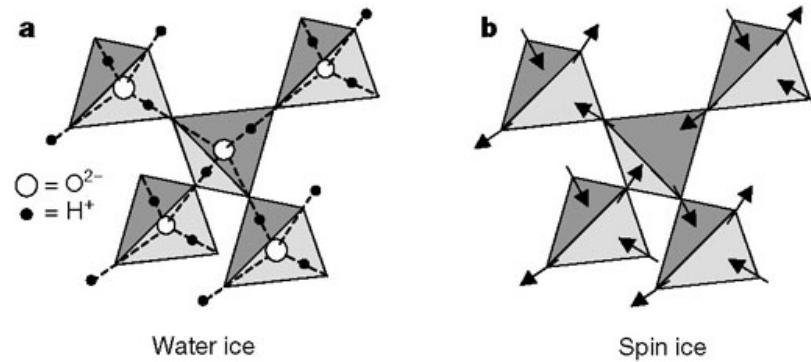n located in the centre of each tetrahedron. The frustration in pyrochlore spin ice arises due to the competing magnetic interactions between the spins of the rare earth metals. These spins are confined along the $\langle 111 \rangle$ axes between each vertex and the centre of the tetrahedron since the strongly anisotropic crystallographic environment results in the maximum magnitude of the magnetic moment vector aligning parallel to this axis [39]. Each spin, which is Ising-like in nature, can point either towards or away from the centre of the tetrahedron and the ground state configuration requires the two-in/two-out 'ice rules' formation of two spins pointing towards the centre and two spins pointing outwards. The geometric similarities between water ice and pyrochlore spin ice are demonstrated in figure 2.7.

2.2.3   Magnetic Monopoles

Researchers have been looking for the elusive magnetic monopole ever since their existence was predicted by Dirac in 1931 [41]. Despite the ubiquity of particles with a single electric charge, there have been no observations of magnetic particles with

a single net charge to date, in spite of the extensive searches that have taken place [42]. Rather than searching for a monopole as an elementary particle, more success has been had in finding and creating magnetic monopoles as emergent particles, i.e. particles that manifest themselves in strongly interacting frustrated systems. It was first shown in 2008 that emergent magnetic monopoles could be formed in pyrochlore spin ice at vertices violating the ice-rules with a three-in / one-out or vice versa configuration [8].

Emergent monopoles have now been observed in pyrochlore spin ice using magnetic neutron scattering [43] and muons [9], and directly observed in ASI using x-ray photoemission electron microscopy [44] and MFM [45]. These magnetic monopole defects in ASI are connected by small tubes that join magnetic monopoles with opposite charges, known as Dirac strings [46, 47] or Nambu strings in square ASI [48]. One of the most exciting potential applications of emergent monopoles is in 'magnetricity', a flow of magnetic charge analogous to the electric charge current used in electricity and first demonstrated by Giblin *et al.* in a $Dy_2Ti_2O_7$ crystal [49].

Emergent magnetic monopoles do not violate Maxwell's equation $\nabla \cdot \mathbf{B} = 0$ since there are no sources or sinks of magnetic flux. Substituting in $\mathbf{B} = \mu_0(\mathbf{H} + \mathbf{M})$ gives $\nabla \cdot \mathbf{M} = -\nabla \cdot \mathbf{H}$. Emergent monopoles are monopoles of the field $\mathbf{H}$ therefore Maxwell's equations will still hold until the discovery of an elementary magnetic monopole.

2.2.4 Artificial Spin Ice

Artificial spin ice (ASI) arrays, first fabricated by Wang *et al.* in 2006 [6], are two-dimensional regular arrays of frustrated ferromagnetic nanomagnets which replicate the frustrations of the three-dimensional pyrochlore spin ice and water ice. These lithographically produced ASI structures can be made up of either isolated or connected bar magnets [50]. The bar magnets have a large enough volume to be thermally stable at room temperature whilst still being small enough to be single domain. Like water ice, ASI has a degenerate ground state arising from the frustration between
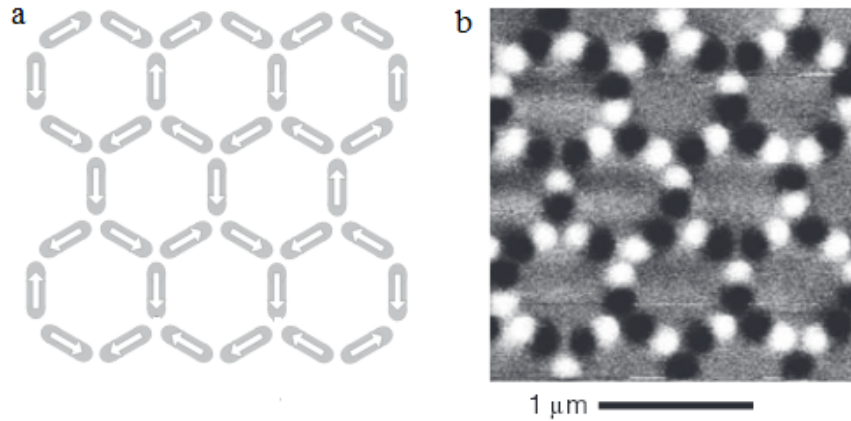
Figure 2.8: A schematic (a) illustrating the nanomagnet configuration of this kagome artificial spin ice and the corresponding MFM image (b) where the black and white dots show the north and south poles of each magnet [52].

elements. However, it has been shown that long-range ground state ordering can be obtained in square ASI by using thermal annealing during the growth process [51].

The most commonly investigated types of ASI are kagome (honeycomb) and square. In kagome ASI there are three magnets meeting at each vertex, as demonstrated in figure 2.8, resulting in $2^3 = 8$ possible magnetic configurations and three simultaneous pairwise interactions to satisfy. The minimisation of energy requires the magnetic spin configurations at each vertex to be the ice-rule obeying two-in/one-out or one-in/two-out. There is an inherent magnetic charge present at each vertex in kagome ASI as a result of presence of an odd number of magnets interacting at each vertex, which can be seen in figure 2.9. The charge is $Q = \pm q$ for ice rule obeying vertices or $\pm 3q$ otherwise.

Square ASI, shown in figure 2.10, comprises four magnets at each vertex. Each vertex has six different pairwise interactions of which at least two must be frustrated due to the geometry of the system. There are $2^4 = 16$ possible magnetic configurations and these are divided into four types, labelled type I - IV, in order of increasing magnetostatic energy, as shown in figure 2.11. The two-in/two-out configurations, corresponding to types I and II, obey the ice rules and so have the minimum amount
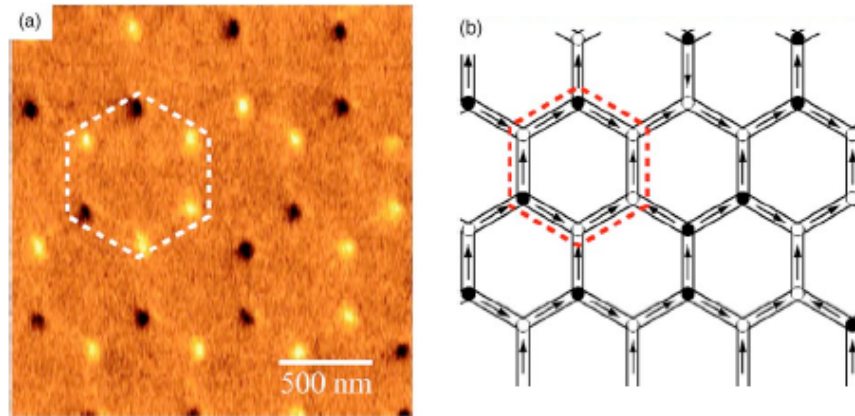
Figure 2.9: An MFM image (a) of connected kagome artificial spin ice where the black and yellow dots show the net charge at each vertex; the corresponding diagram (b) shows the orientations of the spins in the individual magnets [53].

of magnetostatic energy, analogous to the hydrogen ion arrangement in water ice.

Figure 2.11 also shows the percentage of each vertex type that would be expected if the system consisted of independent, non-interacting vertices by considering the amount of different configurations within each type. For a random arrangement of spins, the ice rule obeying two-in/two-out vertex configurations would be expected to make up a total of 37.5% of all vertices [6]. However, it has been found that Type I and II vertices can make up over 70% of all vertices, showing that interactions do take place and that ice rule obeying configurations are favoured. Moreover, the proportions of each vertex type are dependent upon the lattice spacing. When the distance between the magnets increases, the vertex type proportions tend towards those expected for the random distribution of vertex types shown in figure 2.11 owing to the interactions between vertices becoming weaker with distance [6]. As with the kagome ASI, some vertex types can have a net charge; types I and II both have no overall charge with $Q = 0$ due to the equal contributions of in and out spins whereas, for types III and IV, $Q = \pm 2q$ and $\pm 4q$ respectively.
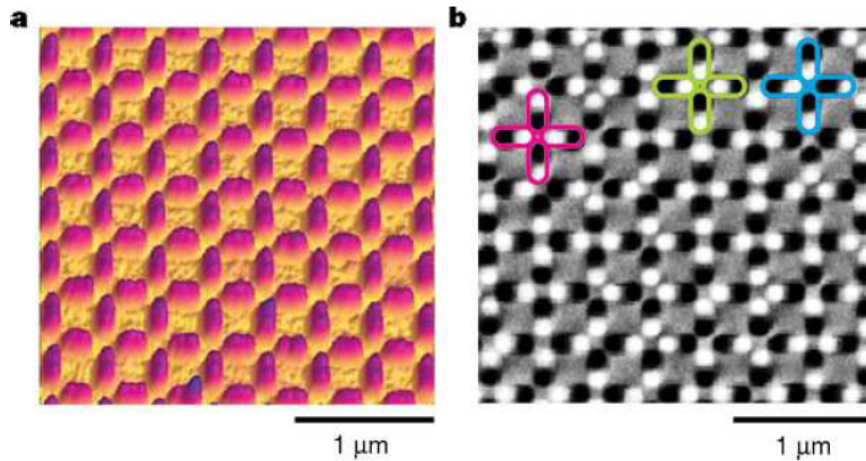
Figure 2.10: AFM (a) and MFM (b) images of an array of square ASI [6]. The vertices highlighted in pink, blue and green show type I, II and III configurations, respectively.
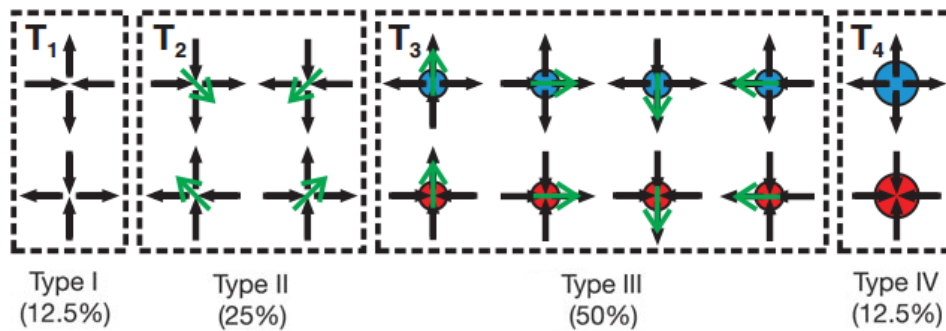
Figure 2.11: The sixteen different combinations for square ASI grouped according to their type [54]. The types are labelled in order of increasing magnetostatic energy. Types I and II obey the ice rules and are two-in/two-out formations with the lowest magnetostatic energy, type III is a three-in/one-out (or vice versa) configuration while type IV has a four-in or four-out spin arrangement. The percentages show the relative proportion of vertices of each type that would be expected to occur in a random non-interacting system. The magnetic charges of types III and IV are denoted by red and blue circles whereas the net dipole moments of types II and III are shown by green arrows

2.2.5 Thermal Studies of ASI

There have been many recent studies into the thermal behaviour of ASI – focusing on the use of heat to obtain long-range ground state ordering. Morgan *et al.* provided the first evidence of this by thermalizing the ASI during the fabrication process [51]. However, this is a one-shot method of achieving the ground state.

Other groups have shown that heating the ASI to above the nanoislands' blocking temperature can consistently provide ground state ordering [52, 55]. This work was undertaken on permalloy nanomagnets, which had a Curie temperature of 800°C and required heating to temperatures of 545°C to observe dynamics. This high temperature limits the accessability of the thermal dynamics, so further work has focused upon achieving the ground state at lower temperatures. The magnetization reversal energy barrier is given by $E = KV$, where V is the volume and K is the shape anisotropy constant, which is dependent upon the magnetization of the elements. E is the energy barrier that has to be overcome to flip the magnetic moment of each nanoisland. Lowering this, by either reducing the magnetization strength of the magnets or reducing the volume, can lower the temperature at which dynamics are observed.

Farhan *et al.* investigated the effects of different volumes on the thermal dynamics of ASI [56]. They used permalloy magnets of constant length and width but with thicknesses between 0 nm and 20 nm and found that, for elements of size 470 nm × 170 nm × 3 nm they could use a photoemission electron microscope (PEEM) to observe the dynamics of this sample over a period of hours at 350 °C.

Work has also been undertaken on using different materials to achieve thermalization at lower temperatures. Kapaklis *et al.* use δ-doped PdFe to obtain dynamics at temperatures of 100 K [57]. More recently, Drisko *et al.* have used $FePd_3$ to observe dynamics that commenced at 110°C [58].

In this thesis, we will compare the thermal dynamics that arise from two PdFe samples fabricated using different ratios of Pd and Fe. Heating the samples in incremental temperature steps has allowed us to be the first group to observe exactly

how the proportion of each vertex type changes as the samples progress towards the ground state for each material.

2.3 Combined Magnetic/Semiconductor Structures

2.3.1 One-dimensional modulations

The study of hybrid semiconductor/ferromagnet devices has been of considerable interest for many years. This interest arises from their potential use in applications such as magnetic storage devices [12, 59] and magnetic field sensors [13, 60, 61].

The theoretical framework regarding the electron transport properties of a 2DEG subjected to periodic magnetic [62–64] and electric fields [65] is now well established. When a low magnetic field B is applied perpendicular to a 2DEG subjected to a weak, periodic potential, extra oscillations periodic in $1/B$ occur in the longitudinal resistance. This effect occurs at a lower magnetic field than Shubnikov-de Haas oscillations (below 0.5 T [66]), with a different period and much weaker temperature dependence [65]. It is only the z component of the magnetic field at the 2DEG that affects the magnetoresistance oscillations.

These oscillations, known as commensurability oscillations (COs) occur when the cyclotron diameter at the Fermi level and the period of the magnetic modulation are commensurate. An electron travelling in a uniform magnetic field experiences a force causing it to move with a curved trajectory about a guiding centre. COs from a periodic potential are caused by this resonance in the $\mathbf{E} \times \mathbf{B}$ drift of the cyclotron orbit centre [67]. In a periodic field, the guiding centre drifts over time and when the electron is drifting sideways its longitudinal resistance is high. Neither electric nor magnetic modulations affect ρ_{xy} since an equal number of cyclotron orbits drift along $y > 0$ and $y < 0$ – hence the Hall resistance always remains unchanged [68].

Figure 2.12 shows the classical electron orbits under the conditions of CO maxima and minima. The first diagram shows the path of an electron following an orbit called a 'snake orbit' at the 0 T field line between two ferromagnetic stripes [68].

The electron travels sideways across the Hall bar, and when an electron is drifting completely sideways its longitudinal resistance is at a maximum. The angle ϕ is the angle at which the electron crosses the line of zero magnetic field. When the electron crosses the line of zero magnetic field at an angle of ϕ_{max}, the snake orbit breaks free from the zero field contour to result in cyclotron orbits [68], as shown in the second diagram. The angle ϕ_{max} is given by:

$$\cos[(\pi - \phi_{max})/2] = Ql_b, \qquad (2.22)$$

where $Q = 2\pi/a$ and $l_b = \sqrt{\hbar k_F/eb}$ and b is the effective magnetic field gradient at the 0 T field line. When ϕ_{max} equals zero, the snake orbits disappear completely and only closed cyclotron orbits remain. These are demonstrated in the third diagram of Figure 2.12, and when these occur the COs have a resistance minimum.
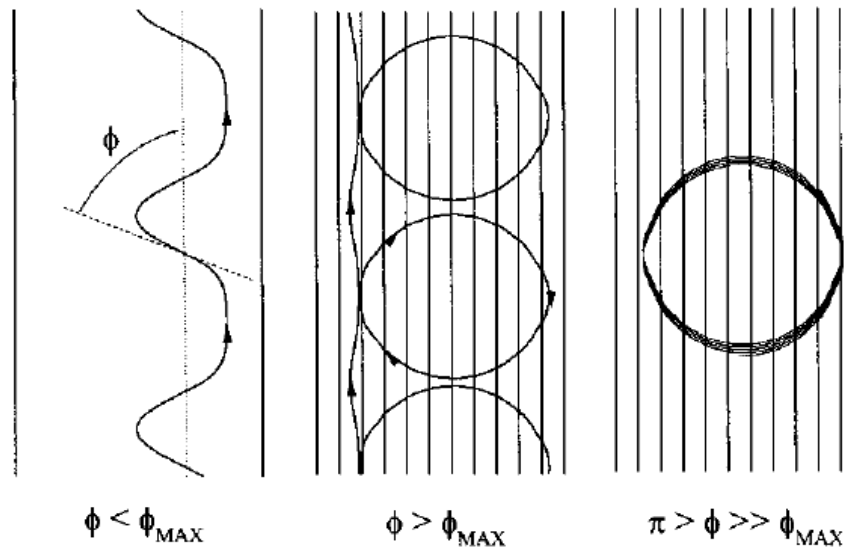
Figure 2.12: The classical electron orbits in a 2DEG under one-dimensional periodic magnetic modulations, from [10]. The solid vertical lines represent the centres of the stripes. The dashed line in the first diagram indicates the line where B_z equals 0. The CO resistance is a maxima in the first diagram, and a minima in the last diagram, with the middle diagram showing the mid-way stage between the two extremes.

When induced by a periodic magnetic field, COs oscillate with minima in ρ_{xx}

appearing at magnetic fields given by [69]:

$$2R_c = \frac{2\hbar k_F}{e|B_0|} = (\lambda + \frac{1}{4})a, \tag{2.23}$$

where R_c is the cyclotron radius, $k_F = \sqrt{2\pi n_s}$, B_0 represents the external magnetic field, a is the periodicity and λ is an oscillation index – a sequence of positive integers starting at 0 and increasing in steps of 1. Physically, λ is the number of periods of magnetic stripes that are encompassed by the electrons travelling in closed orbits.

Oscillations induced by a weak electrical modulation have a very similar expression, with minima in ρ_{xx} expected when:

$$2R_c = \frac{2\hbar k_F}{e|B_0|} = (\lambda - \frac{1}{4})a. \tag{2.24}$$

Therefore, electric and magnetic modulations are completely out of phase, so ρ_{xx} minima for electric modulations and ρ_{xx} maxima for magnetic modulations would be expected to occur at identical B_0 values.

Both electric and magnetic modulations can be expected to occur together since having magnetic elements deposited on the surface of a semiconducting substrate will result in both magnetic oscillations, and electric oscillations caused by the gates on the heterostructure. The two oscillations can be either in-phase or out-of-phase.

In-phase oscillations introduce a phase shift ϕ in the magnetoresistance oscillations, where the phase shift is related to the amplitude of the electric potential modulation, V_0:

$$tan\phi = \frac{2\pi V_0}{ak_F\hbar\omega_0}. \tag{2.25}$$

The magnetoresistance R_{xx} relative to the resistance at no magnetic field R_0 can be given by [62]:

$$\frac{\Delta R_{xx}}{R_0} = \frac{ak_F}{2\pi^2}\frac{\hbar\omega_0}{\hbar\omega_c}\frac{\hbar\omega_0}{E_F}(1+\delta^2)[1 - A(T/T_A)+$$

$$[A(T/T_A) - 2e^{-\pi/\omega_c\tau_f}A(T/T_c)\cos(\frac{2\pi E_F}{\hbar\omega_c})]$$

$$\times \sin^2(\frac{2\pi R_C}{a} - \frac{\pi}{4} + \phi)], \quad (2.26)$$

where $\omega_0 = eB_0/m^*$, B_0 is the strength of the weak 1D periodic modulation of the magnetic field, $\omega_c = eB/m^*$, $\delta = 2\pi V_0/ak_F\hbar\omega_0 = \tan(\phi)$, $A(x) = x/\sinh(x)$ and $T_c = \hbar\omega_c/2\pi^2 k_B$.

If a magnetically modulated heterostructure is exposed to light, the pulses ionize DX centres in the AlGaAs layer between the stripes of magnetic materials. This results in an electric modulation that is $\pi/2$ out of phase with the magnetic modulation [62]. In this case, the magnetoresistance relative to the resistance at zero magnetic field is given by:

$$\frac{\Delta R_{xx}}{R_0} = \frac{ak_F}{2\pi^2}\frac{\hbar\omega_0}{\hbar\omega_c}\frac{\hbar\omega_0}{E_F}(G + \delta^2 F - 2e^{-\pi/\omega_c\tau_f}A(T/T_c)\cos(\frac{2\pi E_F}{\hbar\omega_c})D), \qquad (2.27)$$

$$D = \delta^2 - (\delta^2 - 1)\sin^2(\frac{2\pi R_c}{a} - \frac{\pi}{4}), \qquad (2.28)$$

$$G = [1 - A(T/T_a)]/2 + A(T/T_a)\sin^2(2\pi R_c/a - \pi/4), \qquad (2.29)$$

and

$$F = [1 - A(T/T_a)]/2 + A(T/T_a)\cos^2(2\pi R_c/a - \pi/4). \qquad (2.30)$$

In out-of-phase modulation, the phase factor ϕ is absent from the equations, so changing δ does not change the position of the maxima and minima of the resistivity as a function of B. Figures 2.13 and 2.14 show examples given by Peeters and Vasilopoulos [62] demonstrating in-phase and out-of-phase modulations. In these examples, taken at 4.2 K with $n_s = 3 \times 10^{11}$ cm^{-2}, $a = 300$ nm, $B_0 = 0.02$T and $V_0 = 0.2$ meV, the out-of-phase oscillations are shown to be dampened in comparison with the in-phase oscillations. The out-of-phase oscillations increase in amplitude as V_0 increases and it is at $V_0 = 0.5$ meV that the magnitude of the resistivity oscillations are similar to the in-plane oscillations at 0.2 meV.

An example of COs in a resistance against applied magnetic field graph is shown in figure 2.15. Here we compare the magnetoresistance measurements for a 2DEG under a one-dimensional periodic magnetic potential caused by stripes made from one of two materials, Co and Ni, for different angles of applied magnetic field. Without
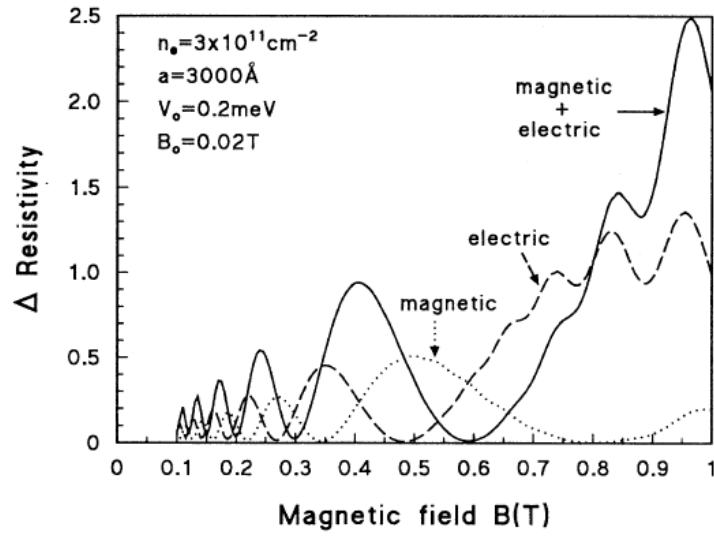
Figure 2.13: The magnitude of combined magnetoresistance oscillations (solid line) for in-phase magnetic (dotted line) oscillations and electric (dashed line) oscillations [62]. The combined electric and magnetic oscillation is shifted by a phase factor ϕ.

Figure 2.14: Out-of-phase combined magnetoresistance oscillations for different values of V_0, but the same parameters as the oscillations shown in Figure 2.13, [62]. These oscillations are dampened, so a V_0 of 0.5 meV is required to obtain the same magnitude of oscillation as was obtained for 0.2 meV in the in-phase example.

Figure 2.15: Magnetoresistance measurements for a 2DEG with a periodic magnetic modulation caused by cobalt and nickel stripes [68]. Measurements 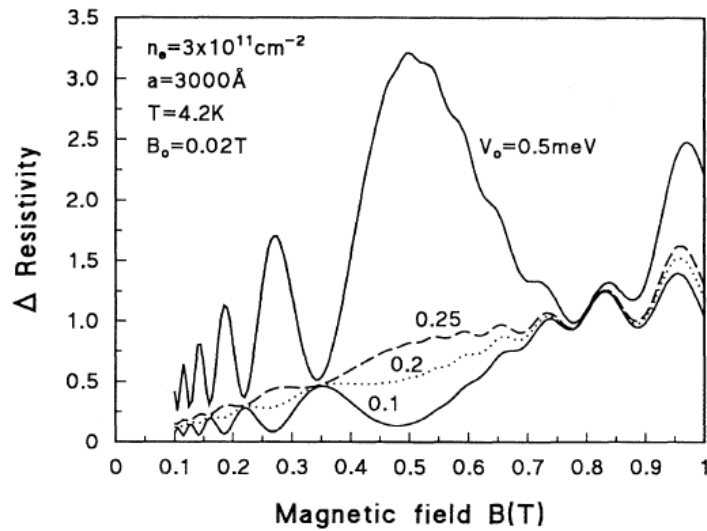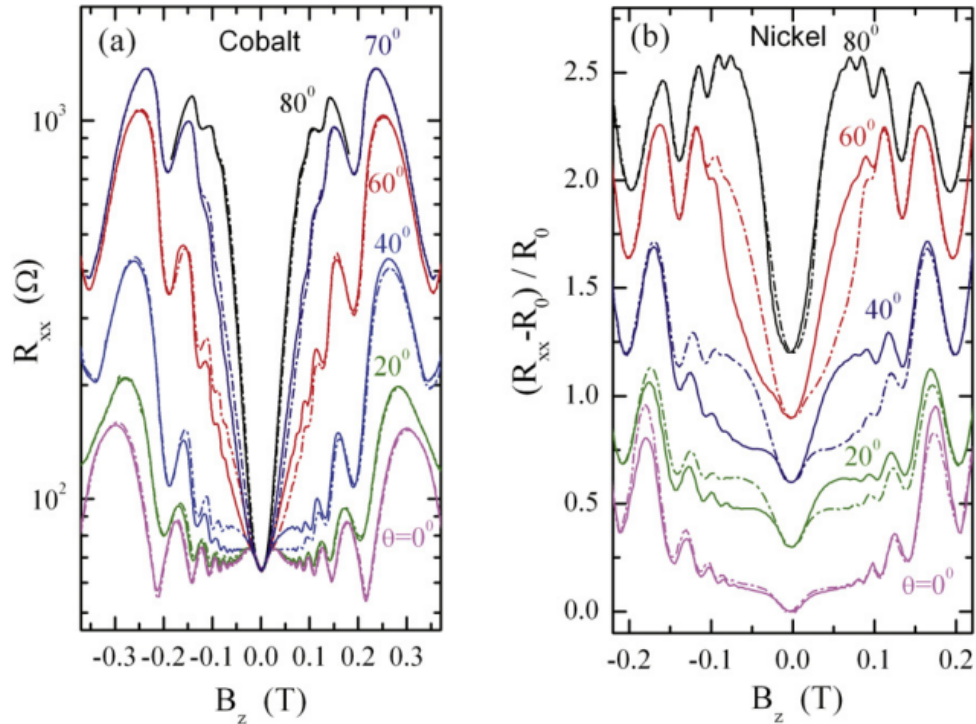were taken at a temperature of 4.2 K at different angles of applied magnetic field with respect to the normal. The magnetoresistance is symmetric about 0 T and the COs become more apparent as the B field angle increases. Clear hysteretic effects can be observed in the Ni sample. For these samples: period = 400 nm, stripe width = 200 nm, stripe height = 160 nm, 2DEG depth = 35 nm

the periodic potential caused by the ferromagnetic stripes, there would be no oscillations present at these low fields. The magnetoresistance becomes stronger and has more oscillations as the angle of applied magnetic field tends towards being in-plane. Simulations show that the amplitude of the stray field at the 2DEG increases as the angle of applied magnetic field becomes more in-plane [10], which will be discussed in more detail in Chapter 5. The discrepancies between the forward and backward field sweeps show that Ni is a more hysteretic material than Co.

2.3.2 Two-dimensional modulations

One of the first pieces of experimental work on the effects of modulations in two dimensions was performed by Gerhardts *et al.* and used a two-step holographic technique [70]. The experiment used a split laser beam reflected from two mirrors to produce an interference line pattern and thus a grating potential with electric modulation in one direction. The magnetoresistance resistivity components ρ_{xx} or ρ_{yy} were then measured. Next, the experiment made use of the persistent photoconductivity effect in Si doped AlGaAs structures at low temperatures, by rotating the sample by $90°$ and performing a second illumination of the sample. This produced a grid potential with electric modulation in both the x and y directions simultaneously, and the magnetoresistance measurements were repeated. The magnetoresistance measurements were found to be significantly dampened in two-dimensions, compared with the oscillations obtained from the one dimensional modulations in the same sample with the same period [70].

This is not the result that would be expected by simply expanding the standard semi-classical theory regarding one dimensional modulations. For a one-dimensional system, a modulation with potential energy $V(x) = V_x \cos(2\pi x/2)$ results in the resistivity ρ_{xx} of [71]:

$$\frac{\Delta\rho_{xx}(V_x)}{\rho_0} = (\frac{\pi l}{a})^2(\frac{V_x}{E_F})^2 J_0^2(\frac{2\pi R_c}{a}) \qquad (2.31)$$

where J_0 is a Bessel function of the first order, ρ_0 is the resistivity at zero applied magnetic field, and l is the mean free path. There would be no effect expected in ρ_{yy} for a system with a modulation in this direction. However, for a system with a one dimensional modulation with potential energy $V(y) = V_y \cos(2\pi y/2)$, equation 2.31 would be altered accordingly with all instances of x changed for y and there would be no effect expected in the ρ_{xx} direction.

For a system with a two dimensional potential energy $V(x,y) = V_x \cos(2\pi x/2) + V_y \cos(2\pi y/2)$, this semiclassical model would expect to generate oscillations in ρ_{xx} according to equation 2.31, with V_y having the same effect on the oscillations in ρ_{yy}

[71]. However, there has been little experimental confirmation of this expected result [71], as seen in the work by Gerhardts *et al.* described above [70].

Grant *et al.* have performed simulations on conduction in a two-dimensional electron gas subject to a weak two-dimensional potential from a lateral surface superlattice, which can help explain the results obtained by Gerhardts *et al.* [71]. They found that V_x and V_y do not contribute independently to the conduction, and instead the introduction of V_y suppresses the oscillations in ρ_{xx} rather than inducing oscillations in ρ_{yy} [71]. They explained this in terms of the drift of the guiding centre of cyclotron motion along contours of an effective potential, whereby the trajectories could drift or be pinned and the pinning suppressed the magnetoresistance [71]. In one dimension, the guiding center of cyclotron motion difts along contours of an effective potential, but the coupling of motion along x and y reduces the stability of COs and the motion of the electrons becomes chaotic at low magnetic fields [71]. Furthermore, COs are harder to observe in two-dimensional potentials because the cyclotron drifts need to be anti-symmetric in each direction to be observed, therefore different V_x and V_y potentials are required.

These effects are shown in the simulations performed by Grant *et al.*. They solved the classical equations of motions for electrons moving in a two dimensional potential energy with V_x constant at 1 meV and V_y changing from 0 to V_x. The results of the longitudinal resistivity against applied magnetic field simulations are shown in Figure 2.16. The main features are the lack of any COs in ρ_{yy} regardless of the value of V_{yy} and the suppression of the COs in ρ_{xx} as V_{yy} increases. In fact, there are no COs present at all when $V_x = V_y$, showing that the potentials need to be anti-symmetric for COs to be present in the magnetoresistance. Similar results would be expected for modulations caused by a periodic magnetic field [71].

Another effect of a two dimensional lattice atop a 2DEG has been found to be the splitting of each Landau band into subbands [72]. For a cosine potential on a lattice with a square symmetry each Landau band splits into p subbands which are
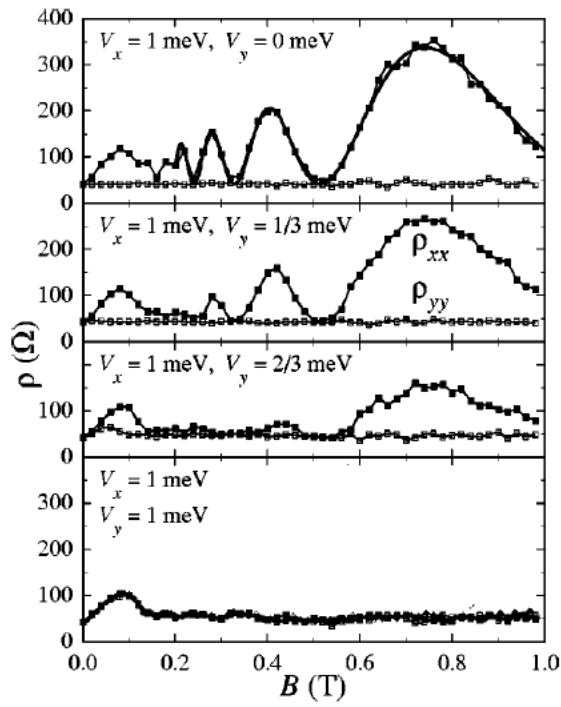
Figure 2.16: Simulated longitudinal resistance for square two-dimensional superlattices with $V_x = 1$ meV and V_y between 0 and V_x [71]. Each graph shows the COs present in ρ_{xx} and the flatter plot of ρ_{yy}.

q fold degenerate, where:

$$\frac{a^2}{2\pi l^2} = \frac{p}{q}. \tag{2.32}$$

The overall width of these Landau bands has the same oscillatory dependence on the Landau levels and the magnetic field as for a one-dimensional lattice, so any observed magnetoresistance oscillations in a two-dimensional lattice have the same period in $1/B$ as the oscillations that would occur in a one-dimensional array [72].

There have also been magnetoresistance measurements performed on 2DEGs subjected to a two dimensional magnetic modulation by Ye *et al.* [11, 73]. In these devices, arrays of Dy dots were fabricated on top of a NiCr layer atop a GaAs-AlGaAs heterostructure. The NiCr gate was used to both improve the adhesion of the ferromagnetic dots to the surface and allow the carrier density to be controlled. Several magnetoresistance against applied magnetic field measurements were performed, where the field was swept to successively higher maximum values to increase the stray field of the Dy dots. Magnetic commensurability oscillations were observed in these samples, where the oscillations increased in magnitude as B_{max} increased, as shown in Figure 2.17. Furthermore, the minima positions of the COs were in close agreement with the positions expected from equation 2.23 for the one-dimensional modulations [11, 73]. Moreover, when varying the gate voltage to alter the carrier density, the experimental minima of the oscillations shifted according to equation 2.23 too [11].

Research to date has investigated the electron transport properties of 2DEGs in the presence of periodically modulated electric [67, 74] and magnetic fields. For periodically modulated magnetic fields, the magnetoresistance properties of irregular arrays of ferromagnetic dots [75], regular arrays of ferromagnetic dots [11] and regular arrays of ferromagnetic stripes [76–78] have all been studied. The creation of a periodically modulated magnetic field at the 2DEG is not limited to the use of ferromagnetic structures, as studies of the magnetoresistance properties of combined semiconductor / Type II superconducting stripes have shown [79]. However, there has so far been limited research into combined ASI and 2DEG structures. The work
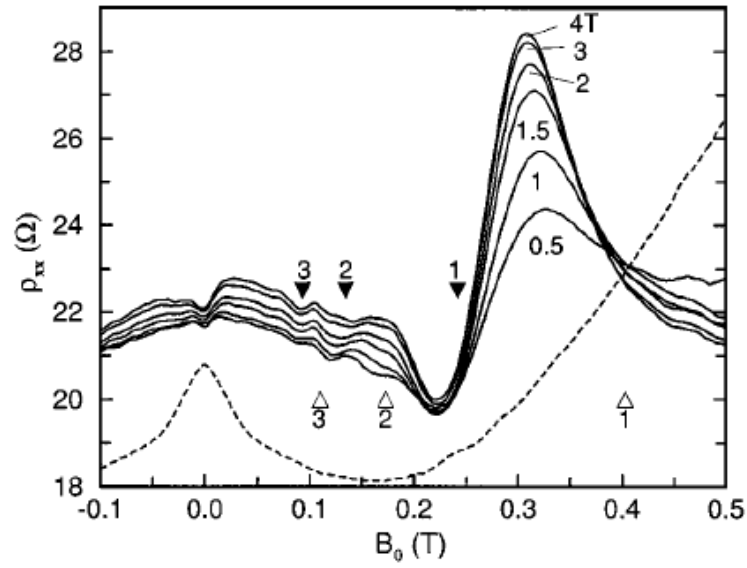
Figure 2.17: Magnetoresistance against applied magnetic field for a two dimensional array of Dy dots [11]. As the maximum field that the magnet is swept to increases, the COs increase in magnitude. The filled triangles mark the positions of predicted magnetic CO minima, whilst the empty triangles mark the positions of predicted electric CO minima. The dashed line shows the magnetoresistance of an unpatterned reference device.

that has been undertaken has focused upon the Hall resistance of single ASI vertices on a GaAs-AlGaAs heterostructure, observing a hysteresis loop in the Hall resistance attributed to the magnetization reversal of the magnetic elements [80, 81]. In this thesis, we investigate the effects on the longitudinal resistance of combined 2DEG/ASI structures, aiming to observe and understand the first examples of commensurability oscillations in these devices.

Chapter 3

Experimental Methods

3.1 Introduction

This chapter discusses the general fabrication and characterisation methods used in this thesis to make the Hall bars and ASI, focusing on reviewing the principles behind each technique and outlining the fabrication steps undertaken during the manufacture of the devices. We also provide an overview of the characterisation techniques used to image the ASI, which allows both a means of assessing the quality of the final structures and the ability to view the magnetic configuration of individual elements of the ASI.

All samples used in this project were fabricated using the cleanroom facilities in the School of Electronic & Electrical Engineering at the University of Leeds, with the electron-beam lithography performed by Dr. Mark Rosamond and molecular beam epitaxy (MBE) by Dr. Lianhe Li. Scanning electron microscopy (SEM) was also undertaken in the School of Electronic & Electrical Engineering whereas atomic force microscopy (AFM) and magnetic force microscopy (MFM) were performed using the facilities in the School of Physics & Astronomy.

The samples used in chapter 6 were fabricated by Dr. Sophie Morley and Dr. Mark Rosamond and the particulars of those samples are discussed further in that chapter.

3.2 Fabrication of Hall Bars

3.2.1 Molecular Beam Epitaxy

Molecular beam epitaxy (MBE) is a thin-film deposition technique developed in 1968 at Bell Telephone Laboratories [82], and is a popular method of fabricating semiconductors owing to its ability to produce thin, uniform wafers with few defects.

A heated substrate is placed into the MBE chamber and the material to be deposited is heated below until it sublimes, producing a beam of particles that are absorbed onto the hot surface of the substrate. Since this happens under ultra-high vacuum conditions, with pressures less than 10^{-10} mbar, the mean free paths of the resulting gaseous particles are several times larger than the distance between the source material and the substrate. A shutter between the source material and the substrate controls the amount of material that is deposited. This process occurs sufficiently slowly that the atoms arriving at the substrate have time to order themselves into a crystalline monolayer structure before the next layer is formed.

The wafers fabricated in this project consisted of a GaAs substrate with a 1 μm high-quality layer of GaAs deposited on top. A 40 nm spacer layer of AlGaAs was then deposited above the GaAs layer, and the 2DEG formed at the interface between these two layers. A 40 nm thick Si doped layer of AlGaAs, with a doping level of 1.33 $\times$ 10^{18} cm^{-3}, was then deposited to provide the electrons that formed the 2DEG. Finally, a 10 nm GaAs layer was deposited to act as a capping layer to protect the AlGaAs layer from oxidation.

3.2.2 Photolithography

Photolithography is a similar technique to electron-beam lithography, which will be discussed in section 3.3.1. It is used to transfer a fixed geometric pattern from a mask to a substrate using ultraviolet radiation and light-sensitive resist.

The positive resist S1813 is spin-coated onto the 2DEG wafer at several thousand RPM and then baked for 3 minutes at 180°C for 3 minutes to remove any excess

solvent from the resist. A mask containing the structure pattern as a series of opaque and transparent shapes is then aligned with the wafer and exposed to UV light for a few seconds. The substrate is then developed by washing in MF319 for one minute. For a positive resist such as S1813, exposure to UV light leads to the polymer chains in the resist breaking, so the MF319 developer dissolves away the regions of the resist that were exposed to the UV light.

After the photolithography process, the wafer can either be acid etched to form Hall bars, or undergo thermal evaporation to deposit material in the gaps left by the exposed resist.

3.2.3   Thermal Evaporation

Thermal evaporation is a physical vapour deposition process, used after photolithography, to deposit material onto a substrate with atomic level accuracy. The sample is screwed to a metal plate and placed inside either the Leybold thermal evaporator, or Edwards 306A bell jar thermal evaporator. A resistive boat or crucible containing the metal to be deposited is placed directly underneath the sample, in order to minimise shadowing effects, and heated by passing a high current through the boat. The resulting vapour condenses onto to the sample and, when the required thickness is reached, a shutter is moved between the boat and the sample to prevent further deposition.

The evaporation process is undertaken under vacuum conditions with a base pressure of the order of 10^{-7} mbar. This both minimises contamination of the material through oxidation, and allows the vapour particulates to travel in a straight line towards the sample. The thickness of the deposited material is measured using a pre-calibrated quartz crystal monitor located within the chamber next to the sample.

Thermal evaporation results in a layer of deposited material covering the entire surface of the substrate. To remove the excess material, leaving just the desired features, requires a process known as lift-off. The sample is soaked in a solvent that dissolves the non-developed resist and thus removes any material attached to that

resist. For the S1813 resist, acetone is used as the solvent. Samples are typically left to soak overnight, but either ultrasonic agitation or heating the acetone can speed up this process. The sample is then washed in acetone and IPA before being dried using N_2 gas. Optical microscopes and atomic force microscopy (AFM) can then be used to check the quality and thickness of the sample's metallic structures.

Thermal evaporation was used in this thesis to deposit the AuGeNi required for our Ohmic contacts, and to deposit the Ti/Au crosses that were used to form alignment markers.

3.2.4 Annealing

Annealing is a technique used to form low resistance Ohmic contacts on a semiconducting substrate, by heating metals to a temperature whereby they diffuse through the semiconductor to the 2DEG.

The Ohmic contacts used for all samples in this thesis are fabricated using an alloy of AuGeNi thermally evaporated onto the surface of a GaAs-AlGaAs wafer. The wafer is placed into a rapid thermal annealer and after several vacuum-nitrogen purge cycles, used to eradicate oxygen and other possible contaminants from the chamber, the chamber is heated to a temperature of 395°C for 50 seconds. At this temperature, the Ga from the GaAs dissolves into the Au and then the Ge diffuses into the GaAs, substituting for the Ga atoms that dissolved into the Au. This results in a highly doped, low resistance region that extends all the way to the 2DEG to form a stable Ohmic contact.

The temperature is an important variable to consider when undertaking annealing – too low and the metals do not diffuse to form the contact but too high and the surface of the contact breaks up too much to allow wires to be bonded to it. 395°C was chosen after experiments were undertaken to decide the optimum temperature that would allow a good quality Ohmic contact to be made whilst simultaneously minimising the surface break-up. Figure 3.1 demonstrates how the temperature affects the break-up of the Ohmic contacts.
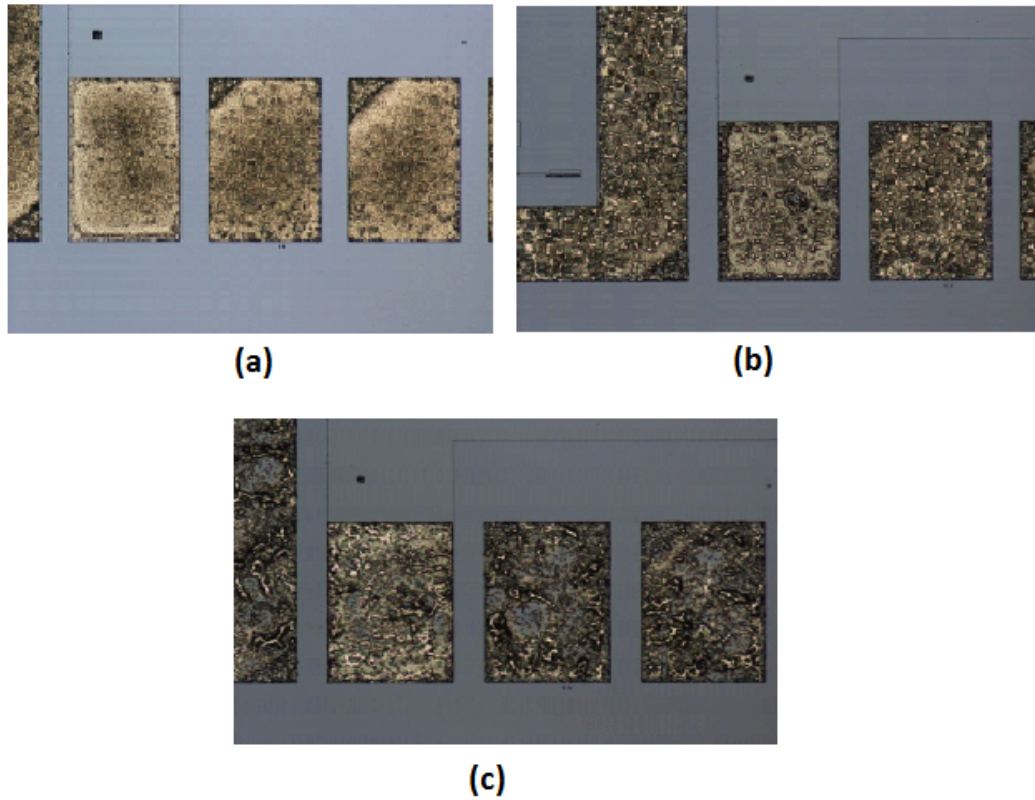
Figure 3.1: The break-up of Ohmic contacts with respect to temperature. Diagrams a, b and c show, respectively, the surface quality of the Ohmic contacts after being annealed at 355°C, 395°C and 445°C for 50 seconds each. At 355°C, the AuGeNi has not fully diffused with the substrate whereas at 445°C regions have completely diffused to leave a broken-up, rough surface that is difficult to bond to. 395°C is a good compromise between obtaining low resistance contacts and having a high quality bonding surface.

3.3 Fabrication of Artificial Spin Ice

3.3.1 Electron-beam Lithography

Electron-beam lithography (EBL) is a technique developed in the late 1960s [83–85] for fabricating structures on a nanoscale. Whilst EBL is a more time-consuming process than photolithography (section 3.2.2), the use of electrons rather than UV light allows smaller structures of less than 10nm [86] to be fabricated.

The process used to fabricate ASI (and other nanostructures) using EBL and electron-beam evaporation (see section 3.3.2) is shown in figure 3.2. First, the polymer resist ZEP 520A is spin-coated onto the GaAs-AlGaAs substrate at several thousand RPM to ensure an even and thin layer of approximately 100nm of resist across the whole substrate. The substrate is then baked at 180°C for 3 minutes to dry the sample and remove any excess solvent from the resist. The resist is exposed to a 100kV electron beam whose position is controlled using computer software in order to write the predetermined pattern. The sample is then developed by washing in amyl acetate. Since ZEP 520A is a positive resist the exposure to the electron beam breaks the polymer chains in the resist, and so the exposed regions dissolve away in the amyl acetate. The ASI material can then be deposited into these gaps using electron-beam evaporation.

3.3.2 Electron-beam Evaporation

Similar to the thermal evaporation process discussed in section 3.2.3, electron-beam (e-beam) evaporation is another vapour deposition process which instead uses a highly focussed beam of electrons to heat the deposition material under vacuum conditions. A water-cooled crucible containing the source material is placed below the sample attached to a metal plate in a Leybold e-beam evaporator. A filament located below the crucible produces an electron beam through thermionic emission, which is then directed using magnetic fields onto the surface of the source material. This heats the material until it melts and evaporates, or sublimes, and the resulting vapour condenses onto the sample at a typical rate of approximately 3 $Ås^{-1}$.

E-beam evaporation has the advantage over thermal evaporation that the temperatures obtainable are not limited by the melting point of the boat; this allows materials with high melting points to be deposited. However, with the heating being very localised, care must be taken to not bore through the material and damage the crucible. If a magnetic material is used as the source material, the magnetic field from the material can have an effect on the position of the magnetically-controlled location
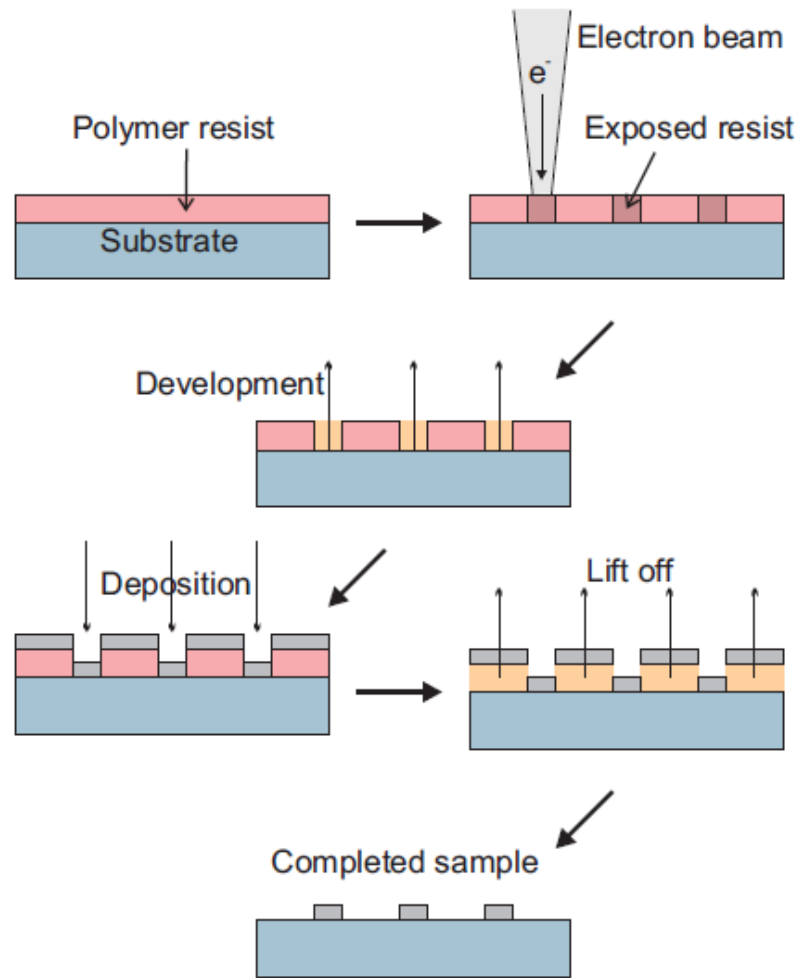
Figure 3.2: The fabrication process of ASI using e-beam lithography (figure taken from [87]). A substrate covered in a thin layer of an electron-sensitive resist is subjected to a beam of electrons in the locations where ASI is to be formed. The sample is then developed in a solvent that removes the exposed resist. Electron-beam evaporation deposits the NiFe across the sample, followed by the lift-off process where the remaining resist is removed by a solvent to leave just the ASI structure.

of the electron beam so the position of the beam has to be frequently monitored to ensure it does not stray from the material.

Following the e-beam evaporation process, lift-off is again used to remove excess material and obtain the required features. The samples are soaked in cyclopentanone

heated to 50°C to dissolve the unexposed ZEP 520A resist, followed by rinsing in acetone and IPA and drying in N_2 gas.

In this project, e-beam evaporation was used to deposit the $Ni_{80}Fe_{20}$ material for the stripes and ASI that were patterned on top of a 2DEG.

3.4 Microscopy Scanning Techniques

3.4.1 Scanning Electron Microscopy

The Scanning Electron Microscope (SEM) first became commercially available in 1965 [88], almost 40 years after the idea of such a technique was first proposed [89]. An SEM uses a focused beam of electrons to image a sample at a nanometer scale.

Electrons emitted under vacuum from a tungsten filament cathode are focused by magnetic lenses into a high energy electron beam. This electron beam passes through the scan coils, a set of plates of different potentials to deflect the beam, and the electrons are then raster scanned across the surface of the sample.

When the beam of electrons reaches the sample, it can either collide with the sample's electrons to form secondary electrons, collide with the sample's atoms to create backscattered electrons, or pass straight through the material. Detectors located in the sample chamber use the secondary and backscattered electrons to form an image of the topography of the sample.

3.4.2 Atomic Force Microscopy

Atomic Force Microscopy (AFM) is a scanning probe microscopy technique used to study the topology of nanostructures, including their height and roughness. AFM was first developed in 1986 by G Binnig *et al.* [90] as a continuation of the work on a scanning tunnelling microscope by the same group [91].

In AFM, an atomically sharp tip of diameter ~10 nm is attached to the underside of a cantilever that has a laser beam reflected off its back towards a photodetector. In tapping mode, which has been used for measuring all the samples in this thesis, the

cantilever vibrates at its resonant frequency and the tip is then brought close to the surface of the sample. As the cantilever moves closer to the sample, the oscillations begin to decrease in amplitude as a result of the long distance van der Waals and electrostatic forces that the tip experiences. This amplitude decrease causes the position of the laser on the photodetector to be altered. An amplitude set point is chosen by the user which corresponds to a fixed height above the sample and, so, a particular oscillation amplitude. The tip is then raster-scanned across the sample and a proportional integral feedback loop keeps the tip at the set height above the sample, moving the tip up and down as the topography dictates in order to maintain this set height. The up and down motion is recorded by the laser/photodetector combination and so a line-by-line image is produced which shows the topography of the sample and measures the heights of the features.

AFM measurements can also be carried out in contact mode where the tip is raster-scanned across the sample while remaining in contact with its surface. The up/down motion of the cantilever as it crosses peaks and troughs in the surface is recorded by the laser/photodiode to produce the image. However, in contact mode the tip is more likely to crash into tall structures than in tapping mode and the force used is also greater, meaning there is more risk of damage to the sample.

3.4.3   Magnetic Force Microscopy

In 1987, it was found that an image of the magnetic profile of a sample could be produced by using a magnetised tip during AFM - a technique known as Magnetic Force Microscopy (MFM) [92]. After each line from the topographical image has been produced by AFM, the tip is raster-scanned a further time across the sample. The user defined height of the MFM scan is at a greater height than that used for the AFM image, but the tip still follows the topography of the sample to maintain the fixed height. The tip, which is magnetised normal to the plane of the sample, is either attracted to or repelled by the stray field from the magnetic sample. This results in an up and down motion that is recorded by the laser and photodetector,

thus allowing the magnetic configuration of the sample to be mapped with the north and south poles represented by areas of dark and light contrast.

Since the magnetic tips interact with the stray field of the sample, MFM is an invasive microscopy technique which could result in the sample's magnetic properties being altered by the tip [93]. To minimise this risk, a tip with a lower coercivity can be used, or the scan height can be increased.

All AFM and MFM measurements performed in this project were undertaken using the Veeco Nanoman AFM probe located in the School of Physics & Astronomy with the probe in tapping mode. The tips used were Bruker MESP tips, coated in a Co-Cr film, with a coercivity of 400 Oe and a magnetic moment of 1×10^{-13} emu.

3.5 Low Temperature Transport Measurements

The magneto-transport measurements undertaken in this work were performed using an Oxford Instruments continuous-flow He cryostat, a schematic of which is shown in figure 3.3. This can reach a base temperature of 1.4 K and attain perpendicular magnetic fields of 8 T.

The sample is secured into a brass head which is then mounted onto the end of the sample stick. This stick is then loaded into the cryostat until the sample is in the centre of a superconducting solenoid placed in a liquid helium bath. To reduce the expenses incurred by liquid helium boiling off too quickly, the helium is surrounded by a liquid nitrogen jacket. The temperature of the sample is controlled using the needle valve, to adjust the flow of helium, and the heater located below the sample.
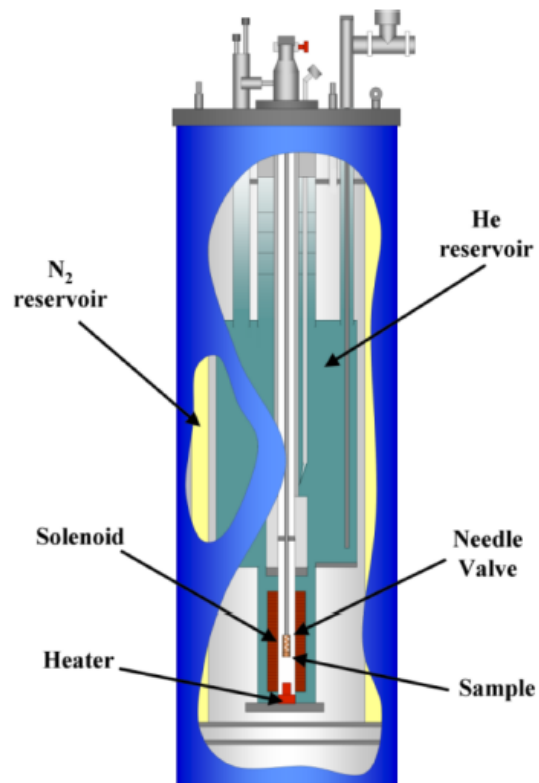
Figure 3.3: A schematic of an Oxford Instruments cryostat [94].

Chapter 4

Characterisation of 2DEGs

4.1 Introduction

This chapter discusses preliminary transport measurements performed on 2DEG wafers; these experiments were undertaken to confirm that the wafers showed standard 2DEG behaviour and to discuss the calculations of the sheet density, mobility and mean free path length for the wafer. Measurements were taken both under illumination and in the dark to demonstrate how the mobility and sheet density changed. This chapter also briefly reviews the experimental procedure used both here and in chapter 5. Finally, the effects of a periodic piezoelectric strain on the transport measurements of the 2DEG are discussed. Strain occurs whenever two different materials are placed in contact and undergo a temperature change, so an understanding of these properties is fundamental to this project. We then discuss how to these effects were minimized – first by investigating the temperature dependence of strain, and then by altering the wafer axis about which the stripes and ASI were aligned.

4.2 Experimental Set Up

Transport measurements of the samples were taken in an Oxford Instruments cryostat, using 4-point resistance measurement techniques. A Keithley 6221 current

source supplied the current, whereas Keithley 2182A nanovoltmeters were used to measure the resulting voltage. The equipment was controlled with a program developed by Dr Gavin Burnell using Labview software. All measurements were taken using a DC current, where the current was routinely flipped for each data point to prevent an emf caused by thermoelectric effects.

This chapter, and chapter 5, show the results obtained from a total of 15 samples. A sketch of the samples used in this project is shown in Figure 4.1. The sketch also shows the circuit configuration used, using measurements of the reference section as an example. Each section has dimensions 300 μm by 100 μm, with the stripes being represented in the figure by the red lines and the ASI by the red squares.

The currents used in this project ranged from 500 nA to 2 μA, although the current was always constant during each experiment. The magnetic field sweep rate was 0.15 T/min, but at each data point the magnet would pause to allow the measurement to be taken. Data points were typically 0.002 T apart for applied magnetic fields up to 0.5 T and 0.02 T apart for magnetic fields above 0.5 T. The magnetic field was calibrated to within 0.01 T; this was measured by performing Hall bar measurements of the Quantum Hall effect, since at 0 T the resistance is known to be 0 Ω.

Figures 4.2 and 4.3 show SEM images of some of the stripes and ASI patterned onto the substrate. The stripes had width 200 nm, period 500nm and the length spanning the width of the Hall bar, whereas the ASI elements had length 200 nm, width 80 nm and period 500 nm. There was some uncertainty of the periodicity of the stripes and ASI owing to the quality of the lift-off of $\pm$ 5 nm.

4.3 Transport Properties of 2DEGs

Transport measurements were first performed in the dark on a plain Hall bar, that is with no stripes or ASI patterned atop, to verify that the well established SdH oscillations and QHE were present. The reproduction of these standard results both verified that our experimental procedure was correct, and allowed us to assess the
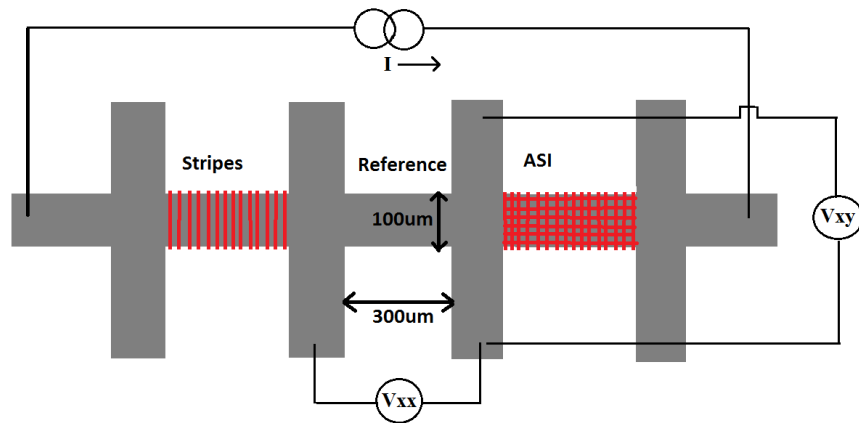
Figure 4.1: A sketch of the Hall bars used, along with the circuit configuration demonstrating the measurements of the Hall and longitudinal voltage of the reference section. The red lines represent the stripes and the red squares represent the ASI sections.
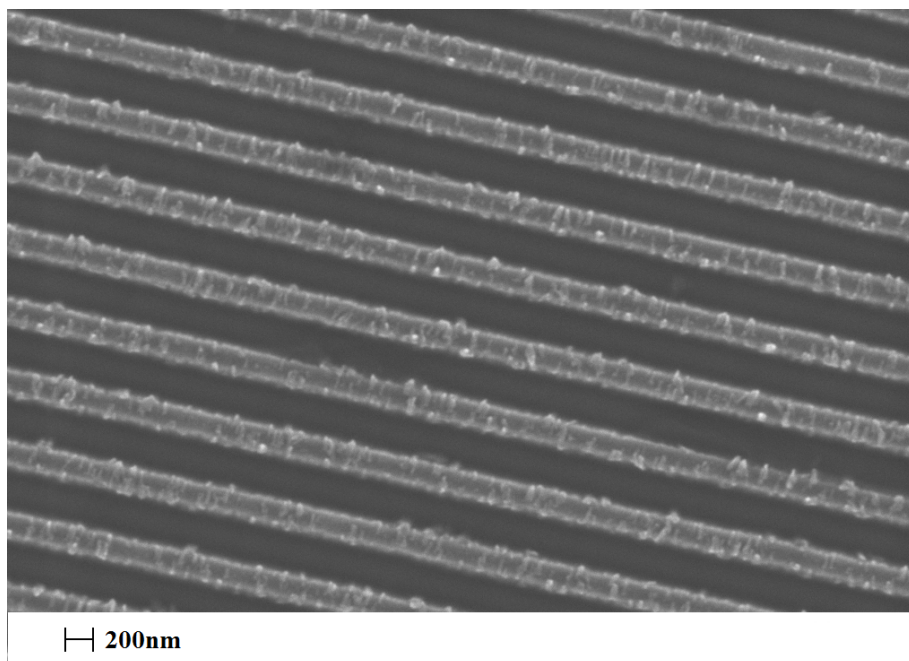

Figure 4.2: An SEM image of the striped section, with stripes of width 200 nm and period 500 nm
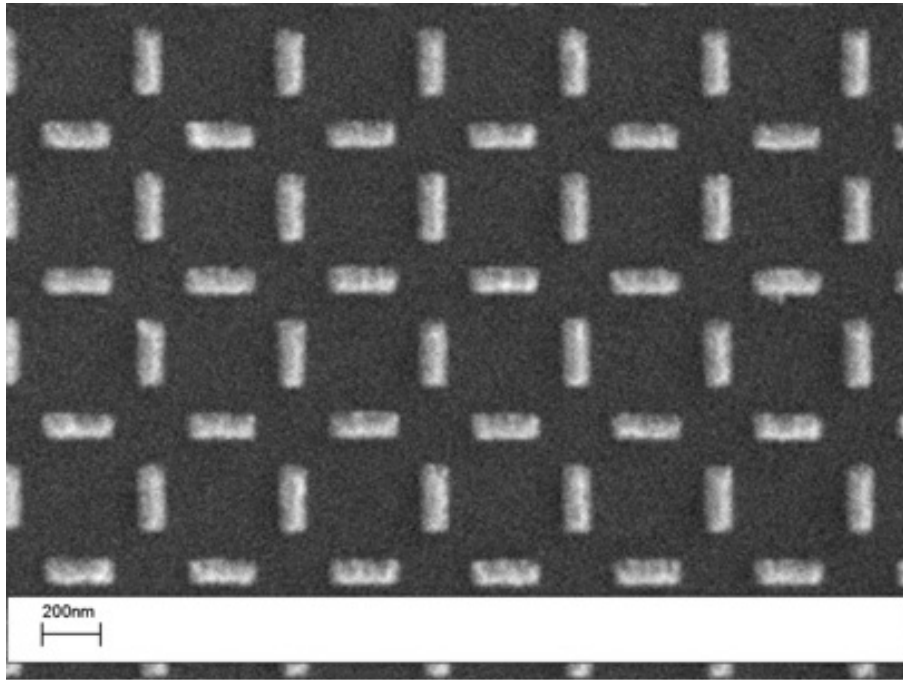
Figure 4.3: An SEM image of the ASI section, with elements of length 200 nm, width 80 nm and period 500 nm.

quality of the 2DEG. The results from one such experiment are shown in figure 4.4. As expected, plateaus in the Hall resistance occur at the same magnetic fields as the troughs in the longitudinal resistance. These troughs reach 0 Ω while at high magnetic fields, and at 0 T the Hall resistance is also 0 Ω.

From figure 4.4 it is possible to calculate the sheet density and mobility of the wafer to provide an indication of the quality of the 2DEG. We can also calculate the mean free path length, from which an appropriate periodicity of stripes and periodicity of ASI to be deposited can be decided. Using equation 2.6:

$$n_s = \frac{IB}{V_H e},$$ (4.1)

and, taking the data obtained at a field of 0.05 T using a current of 500 nA, we obtain a sheet density, n_s, of:
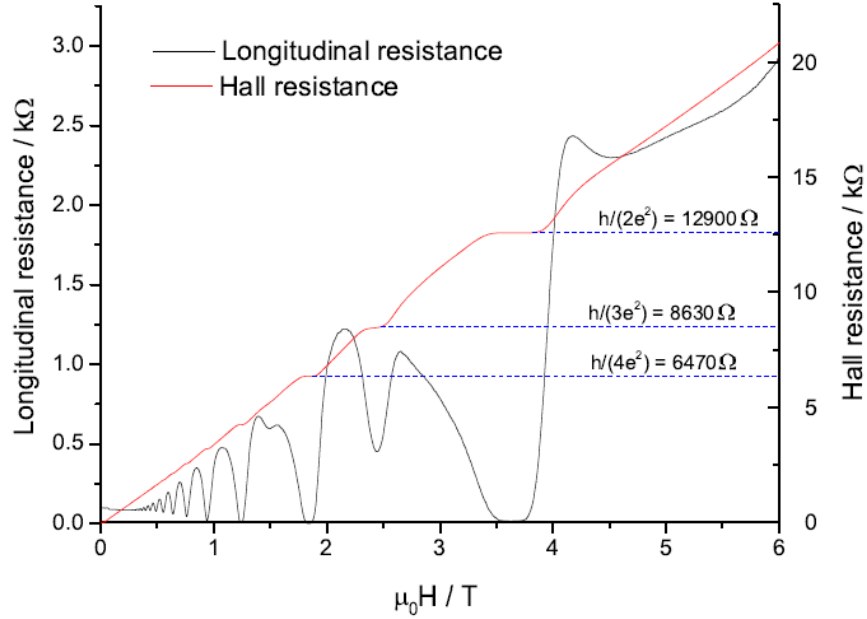
Figure 4.4: The SdH oscillations (black) and QHE (red) results obtained during transport measurements on a plain Hall bar. The blue dashed lines at the location of the Hall resistance plateaus show the predicted resistances for the quantisation of the Hall data matching the experimental data, with the predicted figures given in ohms to three significant figures. The smaller troughs in the longitudinal resistance at 1.5T and 2.5T are caused by Zeeman spin-splitting of the Landau levels at high magnetic fields, a phenomenon resulting in the fractional quantum Hall effect (FQHE).

$$n_s = \frac{500 \times 10^{-9} \times 0.05}{80.9 \times 10^{-6} \times 1.6 \times 10^{-19}} = 1.93 \times 10^{11} \text{cm}^{-2}. \tag{4.2}$$

We can then calculate the mobility of this sample, using this sheet density and equation 2.10

$$\mu = \frac{L}{n_s e R_L W}. \tag{4.3}$$

The Hall bar used here has a channel of length 300 μm and width 100 μm between successive Ohmic contacts so the mobility in the dark is:

$$\mu = \frac{300 \times 10^{-6}}{1.93 \times 10^{11} \times 1.6 \times 10^{-19} \times 106 \times 100 \times 10^{-6}} = 911,000 \text{cm}^{-2}\text{V}^{-1}\text{s}^{-1}. \quad (4.4)$$

These values for the sheet density and mobility are indicative of a good quality 2DEG; we aimed to have a sheet density of the order of 1×10^{11} cm^{-2} and a mobility above 400,000 cm^{-2}V^{-1}s^{-1} for all our samples.

We can now calculate the mean free path using equation 2.21:

$$l = \frac{\hbar \mu k_F}{e} = \frac{\hbar \mu \sqrt{2\pi n_s}}{e}. \quad (4.5)$$

Using the values for n_s and μ obtained above, converted into SI units, the mean free path becomes:

$$l = \frac{1.055 \times 10^{-34} \times 91.1 \times \sqrt{2\pi \times 1.93 \times 10^{15}}}{1.6 \times 10^{-19}} = 6.61 \mu m. \quad (4.6)$$

So the mean free path – the average distance that an electron would travel before being scattered – for this wafer is $\approx$6.6 μm. This calculation of the electron mean free path length enables us to choose an appropriate periodicity for the stripes and ASI that will be deposited upon our Hall bars. It is imperative that the period of our features is smaller than the mean free path to allow the electrons to be affected by the magnetic fields caused by our features. Previous work on combined stripes and 2DEG structures has used a period of 500 nm with a 2DEG at a depth of 35 nm [10]; this is also a suitable period to use for our work given that the electrons in our wafer with this periodicity of stripes would be affected by an average of 13 stripes so any commensurability effects will be clear.

Plateaus in the Hall resistance are known to occur at precisely quantised values of h/Ne^2, where N is an integer number representing the number of filled Landau levels, regardless of the properties of the conducting material. By substituting $N = 1$, 2, 3... we can therefore predict the values in the Hall resistance where plateaus will be present. Figure 4.4 gives these predicted resistances for N values of 2, 3 and 4 ($N = 1$ gives a resistance of 25.6 kΩ, which would require an applied field greater than

6 T to observe) and shows that the plateaus in our Hall resistance data correspond well with the predicted values.
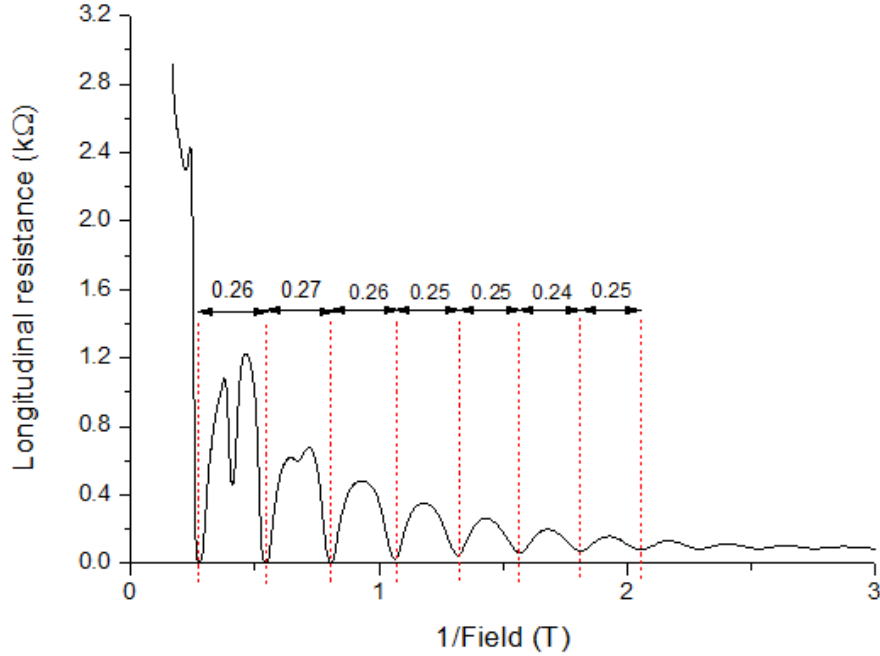

Figure 4.5: The longitudinal resistance of the plain Hall bar against $1/B$. The dashed lines show the distances between successive minima of $1/B$ with the regularity of the oscillations indicating that the SdH oscillations are periodic in $1/B$.

The energy separation of Landau levels is proportional to B but the density of states at the electrochemical potential oscillates as 1/B. The oscillations in the longitudinal resistance are caused by the Landau levels and these oscillations are periodic in 1/B. Figure 4.5, a graph of longitudinal resistance against 1/B, proves that in our samples, SdH oscillations are indeed periodic in 1/B. The period of the SdH oscillations provides another method for calculating the sheet density of the wafer. Combining

$$E_n = (n + 1/2)\hbar\omega,$$

and

$$\omega = \frac{eB}{m},$$

gives

$$E_n = (n + 1/2)\frac{eB\hbar}{m}, \tag{4.7}$$

which, when rearranged, forms

$$\frac{1}{B} = (n + 1/2)\frac{e\hbar}{mE_n}. \tag{4.8}$$

For a fixed Fermi energy, the difference between successive $1/B$ minima is:

$$\Delta(\frac{1}{B}) = \frac{1}{B_{n+1}} - \frac{1}{B_n},$$

$$\Delta(\frac{1}{B}) = ((n+1) + 1/2)\frac{e\hbar}{mE_F} - (n + 1/2)\frac{e\hbar}{mE_F},$$

$$\Delta(\frac{1}{B}) = \frac{e\hbar}{mE_F}. \tag{4.9}$$

Then, by using

$$E_F = \frac{\hbar^2 k_F^2}{2m},$$

and

$$k_F = \sqrt{2\pi n_s},$$

equation 4.9 becomes

$$\Delta(\frac{1}{B}) = \frac{e}{\pi\hbar n_s} = \frac{2e}{hn_s}, \tag{4.10}$$

so we obtain for the sheet density, n_s:

$$n_s = \frac{2e}{h\Delta(\frac{1}{B})}. \tag{4.11}$$

Equation 4.11 shows that it is possible to calculate the sheet density of a 2DEG using just the fundamental constants and the period of the SdH oscillations. Using this equation, and the period of oscillations shown in figure 4.5, the sheet density for this sample is calculated to be 1.93×10^{11} cm^{-2}. Therefore, using two different methods we have calculated the sheet density of our 2DEG to be the same value to three significant figures, so we can be confident that our calculations are correct using either method.

4.4 Dark and Light Transport Measurements

The illumination of GaAs-AlGaAs wafers has been shown to increase the sheet density and mobility of heterostructures [95–97]. Using the same device, we investigated the effects of illumination on our samples by performing transport measurements in the dark, followed by the same measurements after the sample had been exposed to a red laser light for 20 seconds, and comparing the longitudinal resistances from each measurement. Both experiments were undertaken at 1.5 K using a current of 500 nA, and the results are shown in figure 4.6.
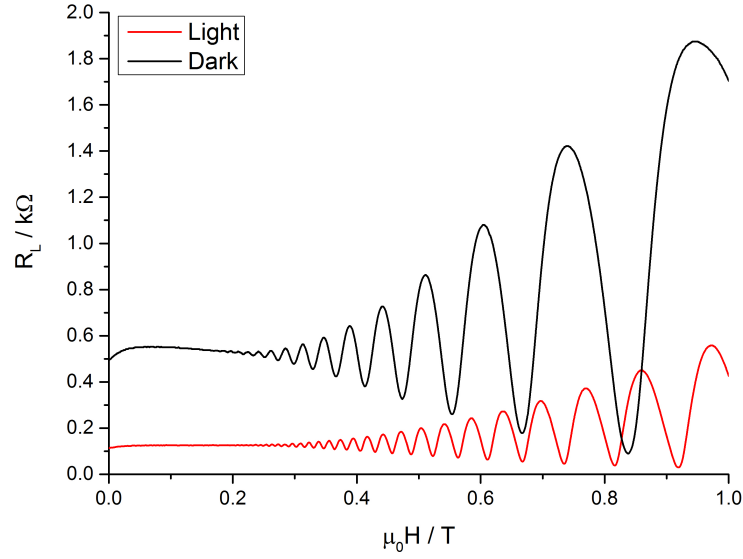
Figure 4.6: A comparison of longitudinal resistance measurements taken with and without illumination on the same reference sample.

Figure 4.6 shows that the resistance for the sample after illumination is up to five times lower than the resistance obtained in the dark, and with approximately twice as many oscillations within the same field range. The sheet density, mobility and electron mean free path length in the dark are 1.57×10^{11} cm^{-2}, $217{,}000$ cm^{-2}V^{-1}s^{-1} and 1.42 μm respectively, whereas these figures for the sample after illumination are 3.54×10^{11} cm^{-2}, $423{,}000$ cm^{-2}V^{-1}s^{-1} and 4.16 μm. The illumination has had the effect of more than doubling the sheet density, increasing the mobility by approximately a factor of two and almost trebling the mean free path length.

Once illuminated, these enhancements of a 2DEG's characteristics are known to last for days, even after the removal of the optical excitation source, as long as the temperature of the system stays below 77 K [98, 99]. This effect is known as persistent photoconductivity and it occurs when a sample is illuminated under either red ($h\nu > E_g$) or infrared light ($h\nu < E_g$) [100]. The absorption of the red light generates more electron-hole pairs in the 2DEG, which consequently increases the number of free

electrons and hence increases the sheet density of the wafer. The slow relaxation of the excess conductivity is caused by energy barriers that cannot be overcome by the carriers at low temperatures [101]. DX centres are defects that lead to the effect of persistent photoconductivity. The DX centre is a highly localized and negatively charged defect centre which is stongly coupled to the crystal lattice. It is also the lowest energy state of the donor atom in AlGaAs [102]. When an electron is captured to this level, it results in a relaxation of the crystal lattice. At low temperatures, the capture rate is extremely low, resulting in persistent photoconductivity [102].

Unless stated otherwise, due to equipment constraints, samples in the following experiments were not illuminated prior to the measurements.

4.5 Piezoelectric Strain

4.5.1 The Onset of Piezoelectric Strain Effects

The deposition of material on top of a 2DEG is known to induce unavoidable electrostatic modulations in longitudinal resistance measurements, whether the deposited material is superconducting [103] or ferromagnetic [10, 104, 105]. The minima of these oscillations are expected to occur at applied magnetic field values of

$$2R_c = \frac{2\hbar k_F}{e|B_0|} = (\lambda - \frac{1}{4})a.$$ (4.12)

Electrostatic modulation is caused by the piezoelectric strain that arises from the differential contraction of the substrate surface and the deposited material when the sample is cooled [106]. With these effects too large to ignore, it was necessary to understand their properties and try to minimise the oscillations caused by piezoelectric strain. To determine how significant the effects of piezoelectric strain was on our samples, we fabricated two sets of devices on the same GaAs-AlGaAs wafer. On one set we deposited ASI and stripes made from Ti, and on the other set we used NiFe for the stripes and ASI. We then performed longitudinal resistance against applied magnetic field measurements on these samples at temperatures of 1.4K, with the

results shown in figure 4.7. Any oscillations caused by the piezoelectric strain would be apparent in both the Ti and NiFe samples, whereas magnetic commensurability oscillations would only be found in the NiFe samples.

It is clear from figure 4.7 that piezoelectric strain has a significant affect on our results. This is demonstrated by the almost identical oscillations occuring in the longitudinal resistance for Ti and NiFe samples, and the lack of any extra oscillations in the NiFe samples that could be attributed to magnetic commensurability oscillations. We can conclude from this that piezoelectric strain is the dominant effect present in these samples, and any magnetic oscillations are being stifled by the strain. It is necessary to verify that these oscillations are attributable to piezoelectric strain effects. Using equation 2.24:

$$2R_c = \frac{2\hbar k_F}{e|B_0|} = (\lambda - \frac{1}{4})a,$$

and rearranging to form

$$B_0 = \frac{2\hbar\sqrt{2\pi n_s}}{ea(\lambda - \frac{1}{4})}, \tag{4.13}$$

it is possible to predict at which applied field the minima of these strain-induced oscillations occured.

First, the sheet density, n_s, is required. This can be calculated using SdH oscillations, as was demonstrated in section 4.3. Using the reference section of the Hall bar, the SdH oscillations were confirmed to be periodic in $1/B$ in figure 4.8 and a sheet density of 3.24×10^{15} m^{-2} was obtained.

The location of strain minima can be predicted using equation 4.13. The initial results, using a period, a, of 500 nm and sheet density, n_s, of 3.24×10^{15} m^{-2} are shown in table 4.1 and presented graphically in figure 4.9. The predicted and actual values for B_0 show little correlation, implying that either the sheet density or the period are incorrect.
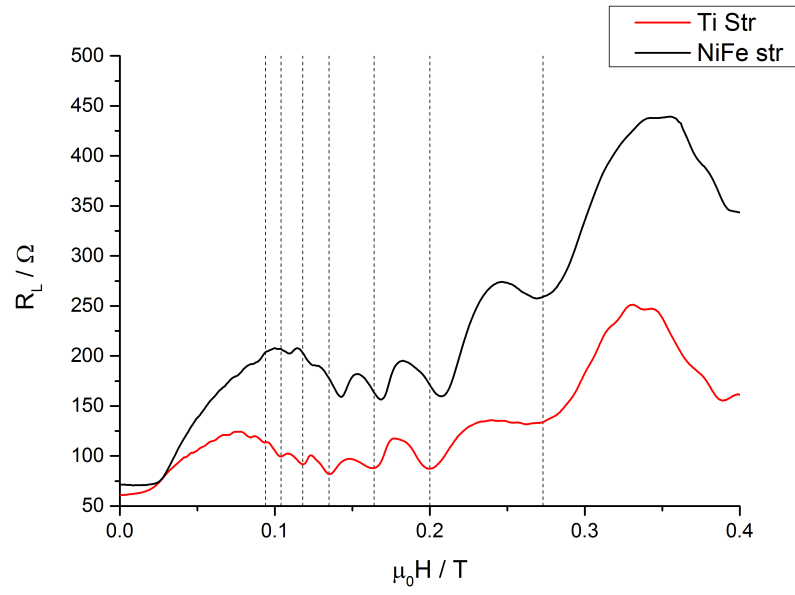
(a) Piezoelectric strain in the striped sections of Ti and NiFe samples.
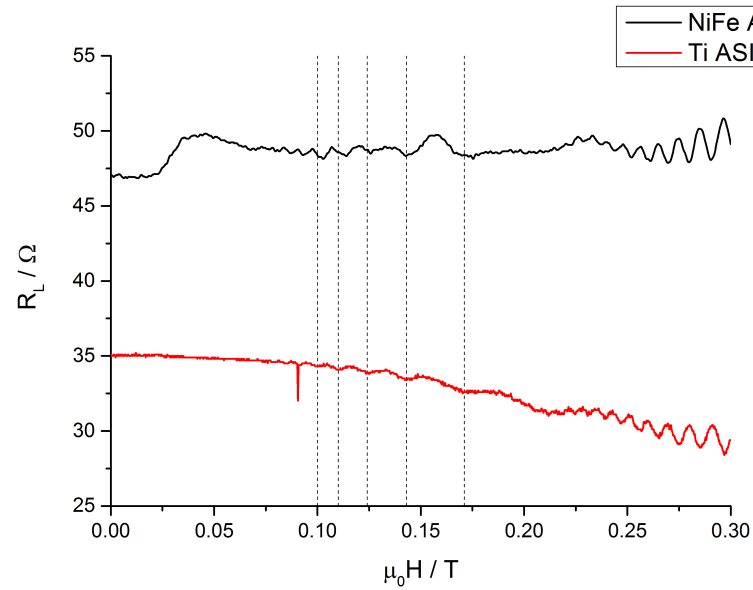
(b) Piezoelectric strain in the ASI sections of Ti and NiFe samples.

Figure 4.7: The dominance of piezoelectric strain effects over magnetic effects is shown through the comparison of Ti and NiFe transport measurements. There is little difference in the oscillations in the longitudinal resistance between the non-magnetic Ti stripes and the ferromagnetic NiFe stripes, showing that effects other than the magnetic commensurability effects must be dominating. The dashed lines show the locations of the minima of the Ti oscillations.
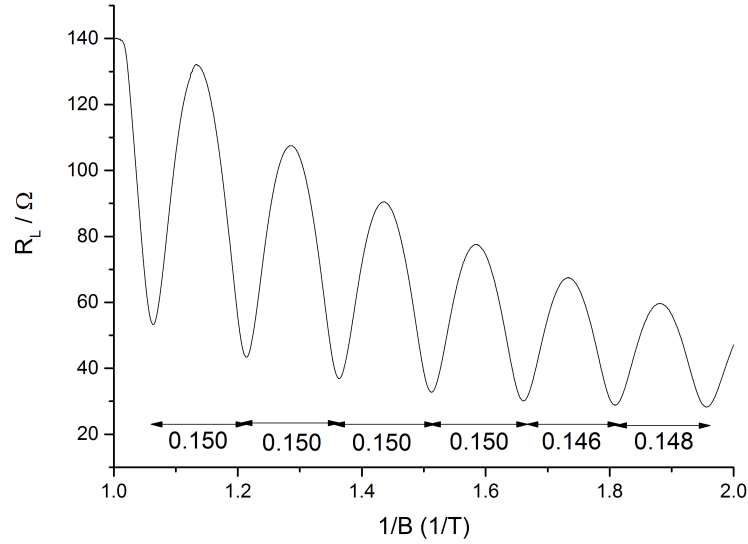
Figure 4.8: The regularity of SdH oscillations shows that they are periodic in $1/B$.

λ	predicted B_0 / T	actual B_0 / T
1	0.502	-
2	0.215	0.200
3	0.137	0.163
4	0.100	0.135
5	0.079	0.118

Table 4.1: The predicted values for the locations of oscillation minima caused by piezoelectric strain in the Ti striped sample. A sheet density of 3.24×10^{15} m^{-2} and period of 500 nm are used for these calculations. The actual values of oscillation minima are also shown for comparison. The predicted values and actual values for the minima show little resemblance.
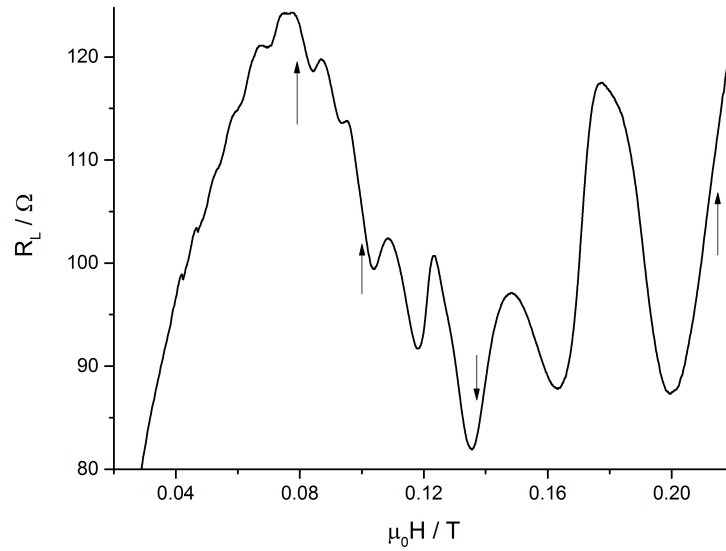
Figure 4.9: The longitudinal resistance of Ti stripes with arrows showing the locations of the predicted minima for commensurability oscillations caused by piezoelectric strain. The predictions are a poor match for the data, indicating that either the period (500 nm) and/or the sheet density (3.24×10^{15} m^{-2}) used to obtain these predictions are incorrect.

Similar effects, where the observed oscillations are very clear but the predicted locations of the minima do not match the experimental data, have been noticed previously [107]. In this paper, Ni stripes with a width of 250 nm and period 500 nm and Nb stripes of width 317 nm and period 950 nm were deposited upon GaAs-AlGaAs wafers with a 100 nm deep 2DEG. In these samples, they observed electrostatic strain effects with periods of the width of the stripes, rather than the distance between successive stripes. They explain that in this case it is the stress at the edges of the stripes caused by the different thermal expansion coefficients of GaAs-AlGaAs and the Ni or Nb which give rise to the periodic modulations observed [107].

Using this technique for our samples, we recalculated the predicted oscillation minima using a period of 200 nm (the width of the stripes) rather the 500 nm

λ	predicted B_0 / T	actual B_0 / T
1	1.25	-
2	0.537	-
3	0.342	-
4	0.251	-
5	0.198	0.200
6	0.164	0.163
7	0.139	0.135
8	0.121	0.118
9	0.107	0.104
10	0.0965	0.0938
11	0.0875	0.0843
12	0.0800	0.0766

Table 4.2: The predicted values for the locations of oscillation minima caused by piezoelectric strain in the Ti striped sample. A sheet density of 3.24×10^{15} m^{-2} and period of 200 nm are used for these calculations. The actual values of oscillation minima are also shown for comparison. The predicted values and actual values for the minima are a much better match than the predictions given in table 4.1, but there is still room for improvement with an average discrepancy of 2.8 % between the predicted and actual values.

period of the stripes used previously. These results are shown in table 4.2 and are presented graphically in figure 4.10.

We find that using a period of 200 nm, the predicted oscillation minima are indeed a better match for the observed data, but with an average discrepancy between the two values of almost 3 % so there is still room for improvement. The sheet density used above was that of the reference section but the sheet density of the striped section could be lower than that of the reference section owing to partial depletion of the 2DEG. Calculating the sheet density of the striped section using SdH oscillations
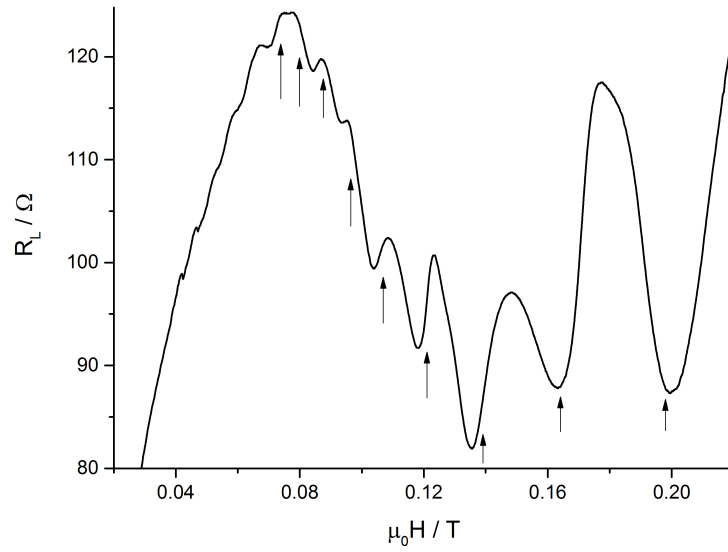
Figure 4.10: The longitudinal resistance of Ti stripes with arrows showing the locations of the predicted minima for commensurability oscillations caused by piezoelectric strain. The predictions are a better match for the data than those found in figure 4.9 although the predicted and actual minima do not correlate perfectly with one another. There is an average residual difference of ≈ 2.8 % between these values, indicating that either the period (200 nm) and/or the sheet density (3.24×10^{15} m^{-2}) used to obtain these predictions were slightly incorrect.

λ	predicted B_0 / T	actual B_0 / T
1	1.23	-
2	0.528	-
3	0.336	-
4	0.246	-
5	0.195	0.200
6	0.161	0.163
7	0.137	0.135
8	0.119	0.118
9	0.105	0.104
10	0.0948	0.0938
11	0.0860	0.0843
12	0.0787	0.0766

Table 4.3: The predicted values for the locations of oscillation minima caused by piezoelectric strain in the Ti striped sample. A sheet density of 3.13×10^{15} m^{-2} and period of 200 nm are used for these calculations. The actual values of oscillation minima are also shown for comparison. The predicted values and actual values for the minima are a better match than the predictions given in tables 4.1 and 4.2, particularly at small applied magnetic fields, with an average discrepancy of just 1 % between the predicted and actual values.

gives a density of 3.13×10^{15} m^{-2} and using this result, with a stripe period of 200 nm, provides the predictions for oscillation minima given in table 4.3 and figure 4.11.

While these predicted minima, using a sheet density of 3.13×10^{15} m^{-2} and period of 200 nm, are closer to the locations of the actual minima than before, there is still a discrepancy of approximately 1 % between these values. Plotting the longitudinal resistance against 1/B, as shown in figure 4.12, shows that the strain oscillations are not precisely periodic in 1/B. With the formula used to calculate the predicted minima (equation 2.24) requiring a period of 1/B, our predictions for the minima
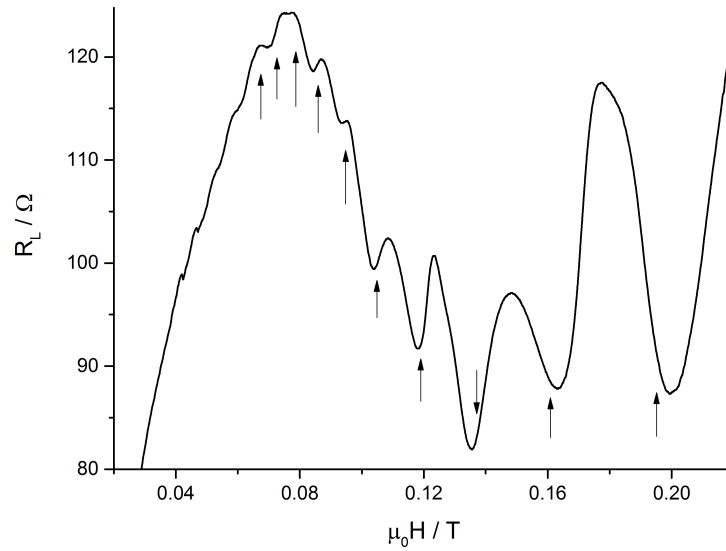
Figure 4.11: The longitudinal resistance of Ti stripes with arrows showing the locations of the predicted minima for commensurability oscillations caused by piezoelectric strain using a period of 200 nm and sheet density of 3.13×10^{15} m^{-2}

positions do not precisely match the actual values.

The effects of strain are far more apparent in the striped samples than in the ASI samples; this can be attributed to the size of the individual elements. With the ASI having dimensions 250 $\times$ 100 $\times$ 100 nm and the stripes spanning the width of the Hall bar with dimensions 200 μm $\times$ 200 nm $\times$ 100 nm, the stripes are significantly larger than the ASI. This continuous length of material will have a greater effect on the piezoelectric strain than the smaller ASI, which can be considered in this case to behave like fragmented stripes, since the differential contractions between the substrate and the material will be greater for larger materials.
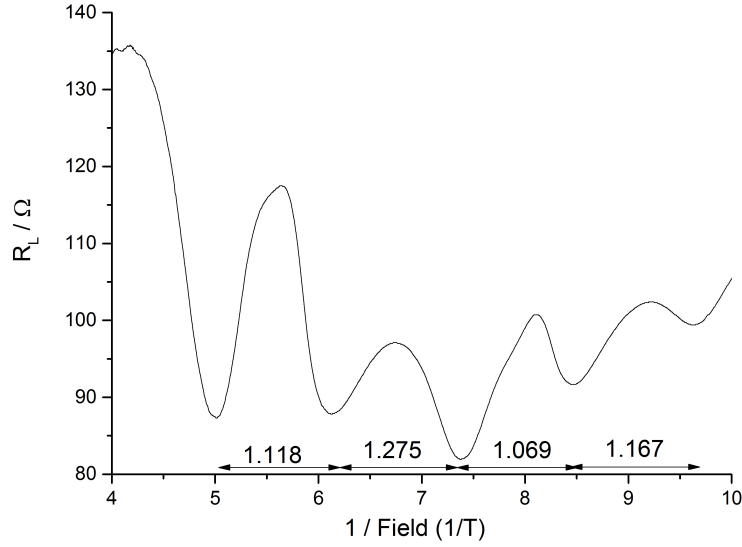
Figure 4.12: The strain oscillations in the Ti sample show that the 1/B periodicity is not exact. This explains why the predicted minima in the strain-induced oscillations do not correlate precisely with the actual locations of the strain minima.

Equation 2.26 can be re-written in terms of measureable parameters to allow the value of the modulation amplitude, V_0 to be obtained and to predict where the oscillations will occur. Equation 2.26 becomes [103]:

$$\frac{\Delta R_{xx}}{R_0} = [\frac{ak_F}{4\pi^2}(\frac{\hbar\omega_0}{E_F})^2(\frac{l_e}{l_m})^2 + (\frac{V_0}{E_F})^2(\frac{l_e^2}{aR_c})]\times$$

$$[1 - A(T/T_A) + A(T/T_A)\sin^2(\frac{2\pi R_C}{a} - \frac{\pi}{4} + \phi)]. \quad (4.14)$$

The first term in the first pair of square brackets relates to magnetic commensurability oscillations, and the phase angle,ϕ, also requires a magnetic effect. Therefore, since we are dealing with purely electrostatic interactions for the Ti material, equation 4.14 can be simplified to:

$$\frac{\Delta R_{xx}}{R_0} = [(\frac{V_0}{E_F})^2(\frac{l_e^2}{aR_c})] \times [1 - A(T/T_A) + A(T/T_A)\sin^2(\frac{2\pi R_C}{a} - \frac{\pi}{4})], \quad (4.15)$$

where l_e is the electron mean free path, $A(x) = x/sinh(x)$ and $4\pi^2 k_B T_A = \hbar\omega_c ak_F$ with $\omega_c = eB/m^*$. Using $n_s = 3.24 \times 10^{15}$ m^{-2} and period of 500 nm, and taking a

first estimate of V_0 to be 0.1 meV in keeping with the results of previous work [103] and [62], we obtain the results in Figure 4.13. These oscillations are not in the same locations as the experimental results shown previously. Predicted oscillations using $n_s = 3.13 \times 10^{15}$ m^{-2} and a period of 200 nm are shown in Figure 4.14. However, these oscillations also do not fit the experimental data, although it is a better fit than that provided by the 500 nm period. This is not due to our estimate of V_0, since this factor only affects the magnitude of the amplitude of the oscillations, not the locations of the oscillations. Furthermore, there are predicted minima in tables 4.2 and 4.3 which are not found in the experimental data. It is not known why neither the oscillations predicted by equation 4.15, nor the oscillations predicted using the other methods detailed above, do not match the experimental data.
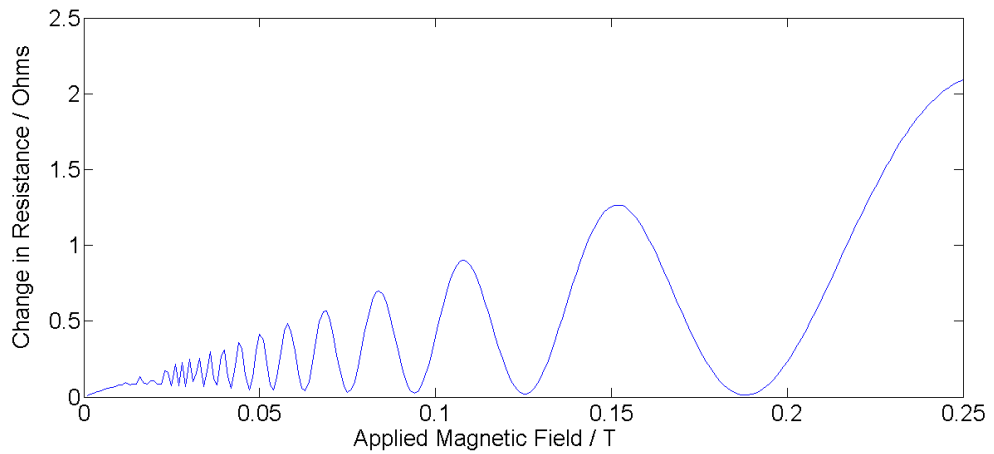

Figure 4.13: The predicted strain oscillations in the Ti sample using $n_s = 3.24 \times 10^{15}$ m^{-2} and period of 500 nm and equation 4.15. It is clear that the oscillations in this figure do not match the experimental oscillations.

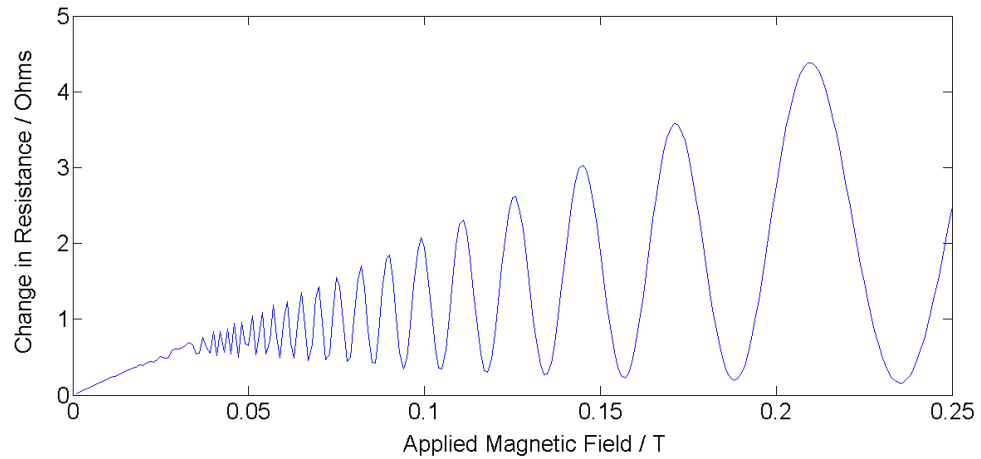**Figure 4.14:** The predicted strain oscillations in the Ti sample using $n_s = 3.13 \times 10^{15}$ m^{-2} and period of 200 nm and equation 4.15. The oscillations in this figure do not match the experimental oscillations, but are a better fit than the 500 nm oscillations.

4.5.2 Thermal Properties of Strain

While the causes of piezoelectric strain are well documented, a literature search did not uncover information relating the effects of strain with temperature. Figure 4.15 shows the results from experiments measuring the longitudinal resistance against magnetic field, conducted on the reference and striped sections at different temperatures. We have chosen to use the striped section here rather than ASI section since the strain effects are more apparent, as shown in figure 4.7. SdH oscillations are highly affected by the temperature that the measurement is conducted at - clear SdH oscillations are present at 1.4 K but doubling the temperature to 2.8 K removes these oscillations at low fields completely. However, piezoelectric strain oscillations are more resistant to the effects of an increase in temperature. Tripling the temperature from 1.4 K to 4.2 K has dampened these oscillations, with more noticeable effects occuring at the lower applied magnetic fields, but strain induced oscillations are still clearly observable at higher fields.

We can explain these results by considering the origin of these oscillations. SdH

oscillations are a quantum effect that is directly related to the 2DEG whereas piezo-electric strain oscillations are a classical effect which indirectly affects the 2DEG through the strain between the substrate and the deposited material. The difference between 1.4 K and 4.2 K is not enough to significantly reduce the amount of strain that the 2DEG experiences so the oscillations are not significantly dampened. These results show that increasing the temperature to reduce the strain would not be an effective technique to use since this would have a more noticeable effect on being detrimental to the 2DEG properties than on minimising the electrostatic strain.

The persistence of low-field COs to higher temperatures than SdH oscillations is, in fact, a known phenomenon [108]. They explain this effect by asserting that at a temperature T, electrons within an energy $k_B T$ of the Fermi energy contribute to the electron transport. However, the thermal smearing of the Fermi circle results in an equivalent smearing of the cyclotron radius. The COs are quenched when the range of cyclotron orbit diameters is approximately equal to the period of the potential [108]. Therefore, the condition to be satisfied to observe COs is:

$$k_B T \leq \hbar \omega_c k_F a/2, \tag{4.16}$$

whereas the equivalent relation for SdH oscillations is:

$$k_B T \leq \hbar \omega_c. \tag{4.17}$$

Therefore, the value of $k_F a/2$ is the factor that determines the temperature persistence difference between the COs and the SdH oscillations. For our samples, assuming a carrier density of approximately 3×10^{15} m^{-2} and a period of 500 nm, $k_F a/2 = 34$. Thus, for our samples, the temperature required to quench the COs would be 34 times higher than the temperature required to quench the SdH oscillations.

4.5.3   Minimising the Effects of Strain

To observe magnetic commensurability oscillations in our samples, it will be necessary to minimise the effects of piezoelectric strain. Increasing the temperature has been
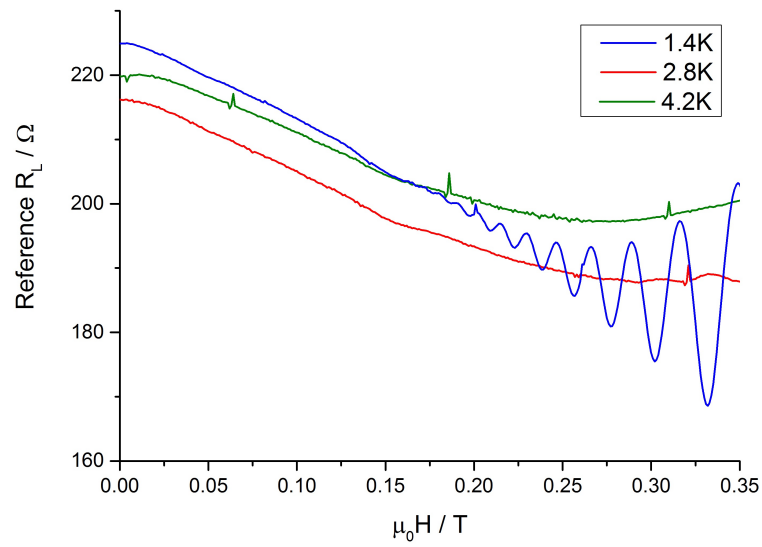
(a) The effects of temperature on SdH oscillations
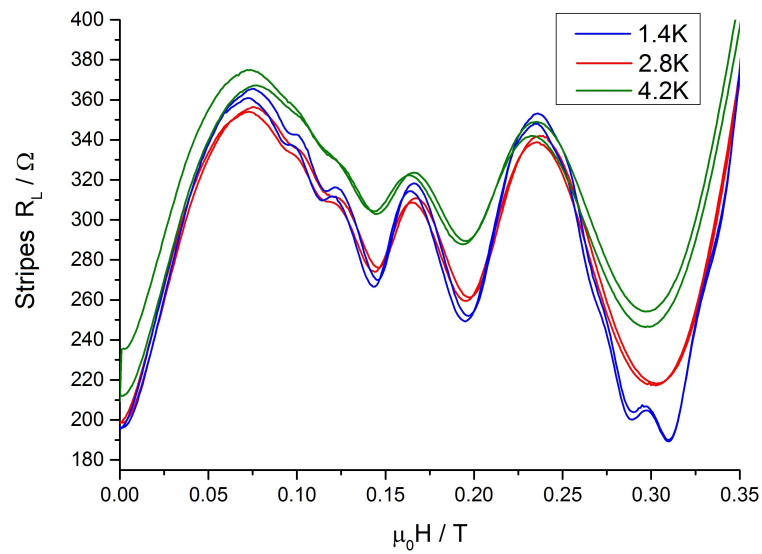
(b) The effects of temperature on piezoelectric strain for a 2DEG with ferromagnetic stripes.

Figure 4.15: SdH oscillations are highly susceptible to changes in temperature, whereas oscillations caused by piezoelectric strain are still very clear at even higher temperatures.

shown to be an ineffective method of reducing the electrostatic strain but it is not the only method available. It has been found that certain axes of a GaAs-AlGaAs wafer are more piezoelectric than others [109, 110], so by aligning our stripes normal to the [100] axis of the wafer, which is non-piezoelectric, oscillations caused by the electrostatic strain can be minimised. We deposited Ti stripes atop a 2DEG in this manner, and compared the longitudinal resistance against the applied magnetic field measurements to those found in figure 4.7, where the stripes are aligned normal to the [110] axis. If this theory is correct, in our striped Ti sample we should see much reduced strain-induced oscillations in the longitudinal resistance and it will look more similar to results obtained in the reference sample.
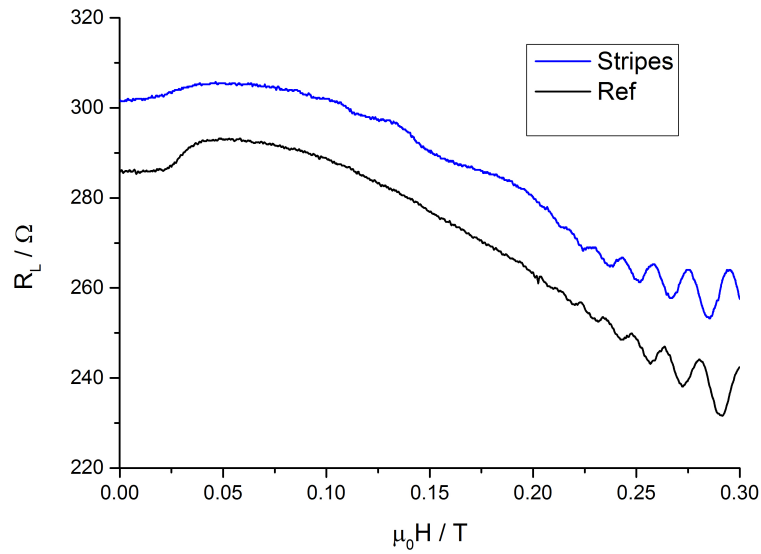
Figure 4.16: The longitudinal resistance of a 2DEG for the reference and Ti striped sections, with the stripes aligned normal to the [100] axis of the wafer. This alignment has strongly reduced the strain-induced oscillations in the magnetoresistance compared with the results found in figure 4.7.

Figure 4.16 shows the results gained when the Ti stripes are aligned normal to the [100] axis. As predicted, the strain here is much reduced compared to previous data using other alignments. Some amount of electrostatic strain will always be present in our samples, but this strain minimisation will allow any magnetic oscillations to be more observable in future NiFe stripe and ASI samples.

4.6   Summary

In this chapter, the experimental procedure used for both this chapter and the following chapter was discussed. The preliminary experiments undertaken on a plain Hall bar indicate that this method can successfully reproduce well-established results regarding the quantum Hall effect and SdH oscillations in the longitudinal resistance. Example calculations demonstrate the methods used to obtain the sheet density,

mobility and mean free path length of a 2DEG wafer. Furthermore, comparisons between these properties when measured in the dark and under illumination have been made, with the illuminated samples showing twice the sheet density and mobility of samples measured in the dark.

There followed an analysis of the effects of piezoelectric strain on the longitudinal resistance of a 2DEG. By comparing the results of transport measurements on two different Hall bars fabricated simultaneously from the same wafer, one with Ti stripes and one with NiFe stripes, we showed that piezoelectric strain was dominating the low field oscillations to the extent that magnetic commensurability oscillations could not be observed. These strain-induced oscillations were shown to act on a period of 200 nm, the width of the stripes, rather than the 500 nm period of the stripes, caused by stress at the edges of the stripes. However, for reasons unknown, the experimental oscillations were not found to be a good fit for the oscillations predicted by equation 4.15.

With the piezoelectric strain oscillations potentially being such a dominating effect, we endeavoured to minimise these effects. We showed that strain oscillations are not temperature dependent, unlike SdH oscillations, so increasing the temperature would not be a successful method of minimising these oscillations. However, we demonstrated that the effects of strain were dependent upon the orientation of the stripes compared to the wafer axes. By aligning the stripes normal to the [100] axis, as opposed to the [110] axis used previously, the piezoelectric strain induced oscillations were minimised. As such, all subsequent results presented in this thesis are based upon a stripe / ASI orientation normal to the [100] axis.

Chapter 5

Transport Properties of Combined 2DEG/ASI Structures

5.1 Introduction

This chapter discusses the effects that ASI and ferromagnetic stripes patterned atop a 2DEG have on the 2DEG's transport properties, focusing on the effects on both the Hall resistance and on the commensurability oscillations in the longitudinal resistance.

Models of the magnitude of the magnetic field at the 2DEG caused by the ferromagnetic stripes were produced to allow comparisons between our work and previous work to be made, and to assist with forming predictions and conclusions.

After minimising the effects of piezo-electric strain in the previous chapter, further experiments were made to ensure that any effects seen in the transport properties were caused solely by the magnetic properties of the stripes and ASI, rather than from our experimental procedures.

We then analyse the effects that ASI has had on both the QHE and commensura-

bility oscillations. Finally, the results from further work undertaken on the temperature and the angular dependence of the ASI induced commensurability oscillations are presented.

5.2 Models of the Magnetic Field at the 2DEG

It is possible to accurately calculate the magnetic modulation profile produced at the 2DEG by the ferromagnetic stripes, showing the magnitude of the x, y or z-components of the magnetic field as a function of distance along the wafer. This is achieved using a Fourier analysis of Maxwell's equations [63, 68], which results in the equations for, respectively, the x, y and z-components of the stray field:

$$B_{1,x}(x, z_0) = \mu_0 M \frac{hd}{a} \sum_{n=1}^{\infty} q_n F(q_n) e^{-q_n(z_0 + h/2)} \sin(q_n x - \theta), \qquad (5.1)$$

$$B_{1,y}(x, z_0) = 0, \qquad (5.2)$$

$$B_{1,z}(x, z_0) = \mu_0 M \frac{hd}{a} \sum_{n=1}^{\infty} q_n F(q_n) e^{-q_n(z_0 + h/2)} \cos(q_n x - \theta) \qquad (5.3)$$

where $q_n = 2\pi n/a$, a is the period of the stripes, n is an integer between 1 and infinity, h and d are the height and width of the stripes respectively, θ is the angle of magnetisation in radians (for an out-of-plane applied magnetic field $\theta = 0$ whereas for an in-plane magnetic field $\theta = \pi/2$), z_0 is the depth of the 2DEG, and $F(q_n)$ is called the form factor, given by:

$$F(q_n) = \frac{\sin(q_n d/2)}{q_n d/2} \frac{\sinh(q_n h/2)}{q_n h/2}$$

This model assumes that the magnetisation of the stripes is both uniform and parallel to the direction of the applied magnetic field.

Our models focus on the z-component of the field since only this component affects the electron dynamics of the 2DEG [10] owing to electron motion being confined to this plane.

It was first necessary to check that our model was correct by reproducing the work done by previous groups, using Ref. [10] as the point of reference. Figure 5.1 shows the graph used in Ref. [10] and our replica of this graph using equation 5.3. Figure 5.1 shows that this model, with the calculations performed using MATLAB, has successfully reproduced the work published by Nogaret *et al.* so is likely to be a suitable model for calculating the stray field profile for our 2DEG wafers.
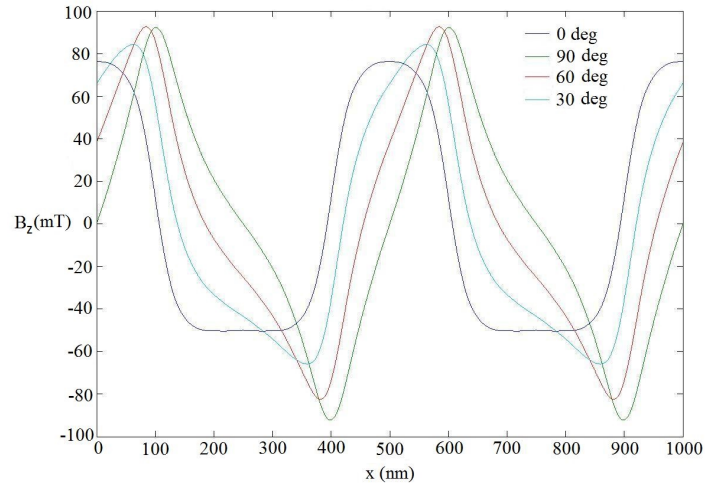
Nogaret *et al.* use a wafer with a 35 nm deep 2DEG, with an array of Ni stripes of period 500 nm, height 100 nm and width 200 nm. This gives a profile asymmetric about 0 T since the width of each stripe is not half the length of the period. There is a large difference between the out-of-plane and in-plane profiles owing to the shallowness of the 2DEG, with the profile being approximately a square wave at 0 degrees but triangular at 90 degrees. The strength of the magnetic field ranges from -50 mT to 75 mT for out-of-plane fields, and -90 mT to 95 mT for in-plane fields. Since these field strengths yielded clear commensurability oscillations for this work, we aim to fabricate stripes that will produce similar field strengths at our 2DEGs.

Figure 5.2 shows the stray field profile that arises for our system, consisting of a wafer with a 90 nm deep 2DEG with NiFe stripes with a 500 nm period, 100 nm height and 200 nm width. The samples used in this project were composed of $Ni_{80}Fe_{20}$ with an assumed value of magnetization of 840kA/m. Despite the depth of the 2DEG being more than twice that used by Nogaret *et al.*, our model shows that our samples should produce the same magnitude of stray field at the 2DEG using the same volume of material in the stripes, since permalloy has a larger magnetisation than nickel. However, our system is predicted to not show a similar large difference between out-of-plane and in-plane measurements, with these profiles showing similar magnitudes and shapes. The depth of the 2DEG also results in the stray field profile having a sinusoidal shape, rather than the square or triangular profiles produced by Nogaret *et al.*.

Figure 5.3 shows the expected strain and magnetic profiles at a 2DEG under certain conditions [73]. In diagram 1 there is a large magnetic field in the z-direction,
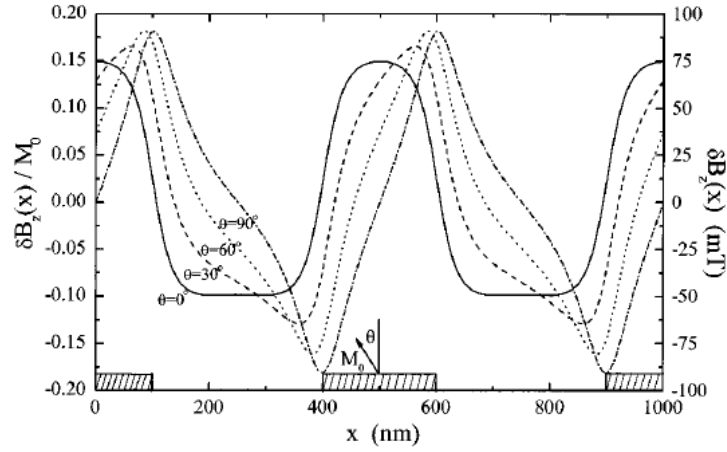
(a)

(b)

Figure 5.1: Confirmation that our model replicates the results found in previous work. Graph (a) shows the results from Nogaret *et al.* of the magnetic field profile for a 35 nm deep 2DEG with arrays of 100 nm high Ni stripes [10]. The results from our model reproducing this system are shown in graph (b). There are two half-stripes located between 0 nm and 100 nm, and 900 nm and 1000 nm, and a whole stripe located between 400 nm and 600 nm, to produce a stray field profile that covers two full periods of stripes. The relationship between θ and the stripes is shown in figure (a).

whilst diagram 2 shows a large magnetic field in the x-direction. For zero applied magnetic field, the magnetization of the stripes lies along the easy axis, or length, of the stripes. There is no magnetic modulation at the 2DEG in this scenario [66].
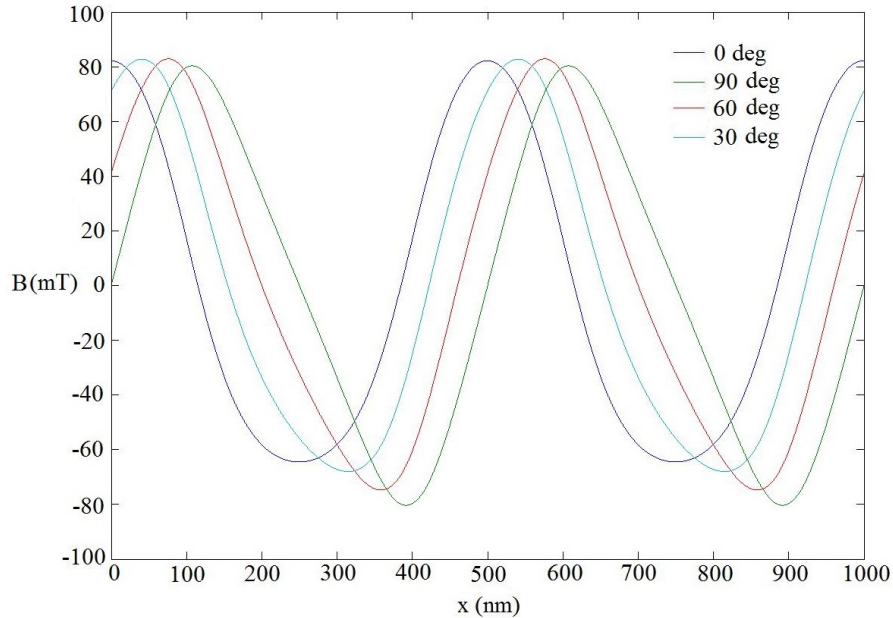

Figure 5.2: A model of the magnetic field profile at the 2DEG for the structures used in this thesis. 100 nm high, 200 nm wide NiFe stripes with a 500 nm period are patterned atop a 90 nm deep 2DEG. The magnitude of the field strength at the 2DEG is similar to that produced by Nogaret *et al.*'s work, but the difference between out-of-plane and in-plane applied fields is not as pronounced.

The saturation field in a particular direction of the NiFe stripes and ASI elements can be calculated by determining the demagnetizing factor and multiplying this by the magnetization strength of the material, which for permalloy is assumed to be 840kA/m, or 1.055T. The demagnetizing factor can be calculated using the equations in reference [111]. Figure 5.4 shows the dimensions of a cuboid with the sides labelled in relation to the direction of the applied magnetic field. For the ASI, when the applied magnetic field is along the easy y-axis, or the side c, the lengths of sides a, b and c are 40 nm, 50 nm and 100 nm respectively. This gives a demagnetizing factor of
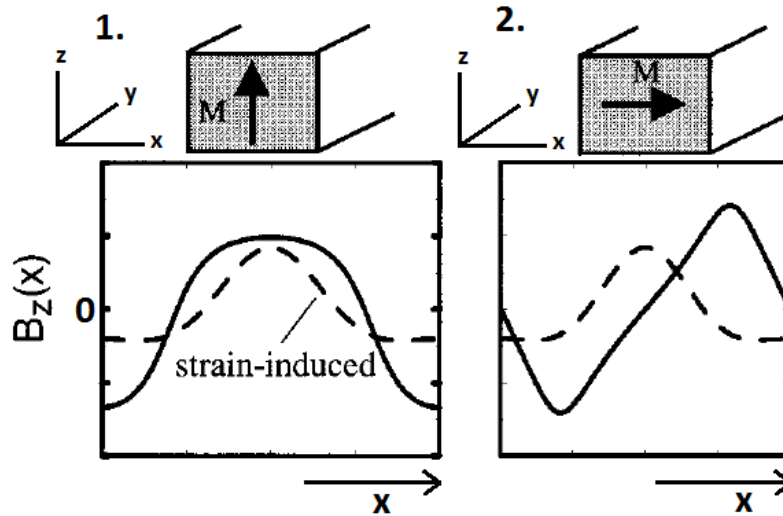
Figure 5.3: The magnetic field profile at the 2DEG induced by a magnetic structure under different applied magnetic field conditions, adapted from Ye *et. al.* [73]. The solid lines show the expected magnetic field profile at the 2DEG whereas the dashed lines show the expected strain profile at the 2DEG. There is no magnetic modulation at the 2DEG when there is zero applied magnetic field, where the magnetization of the magnetic stripes will lie along the length of the stripes.

0.180, which corresponds to a saturation field of 0.191 T. When the applied magnetic field is along the z-axis, the demagnetising factor is 0.367 and the saturation field is 0.388 T. For an applied magnetic field along the x-axis, the demagnetizing factor is 0.453 and the saturation field is 0.478 T. This shows that it is hardest to magnetize the ASI along the width of the magnet, which is the expected result given that the width of the element is the smallest dimension.

For the NiFe stripes, the lengths a, b and c are 100 nm, 50 nm and 37500 nm respectively. The demagnetizing factor along the easy axis is 0.0008 with a corresponding saturation field of 0.00084T. The demagnetizing factor for an applied field along the x-axis is 0.352 with a corresponding saturation field of 0.372 T. Finally, for an applied magnetic field along the z-axis, the demagnetizing factor is 0.647 and the saturation field is 0.683 T. The saturation field is the field at which all the magnetic

spins in a material will be aligned with the applied magnetic field. The long length of the stripes in comparison with the width and height of the stripes results in a strong shape anisotropy in these elements, which is why the saturation field for the length of the stripes is so small. The large saturation fields for the other directions of applied magnetic field along the hard axes explains why some of the prior art ramps the field to a large applied magnetic field straight away before performing magnetoresistance measurements.
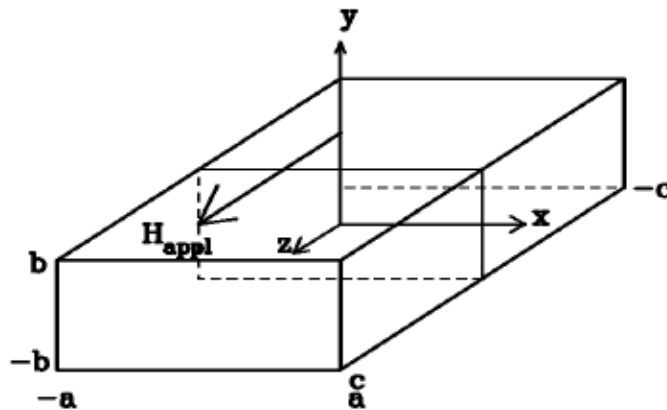
Figure 5.4: Diagram taken from reference [111] showing the dimensions of the cuboid used to determine the lengths a, b and c of the magnetic elements for the purpose of calcuating the demagnetizing factors.

5.3 EBL Effects on the Longitudinal Resistance

The samples used in this chapter were very similar to the samples used in chapter 4. However, the Hall bar was redesigned to have six 'arms' on each side instead of the four 'arms' used before. This allowed the stripes and ASI sections to be patterned across the arms, which enabled more accurate Quantum Hall Effect measurements to be performed. The rest of the design, including the dimensions of the stripes and spin ice elements, and the experimental set up was identical to that used in chapter

4. A sketch of the Hall bar is shown in Figure 5.3, along with the new length and width measurements of the Hall bar.
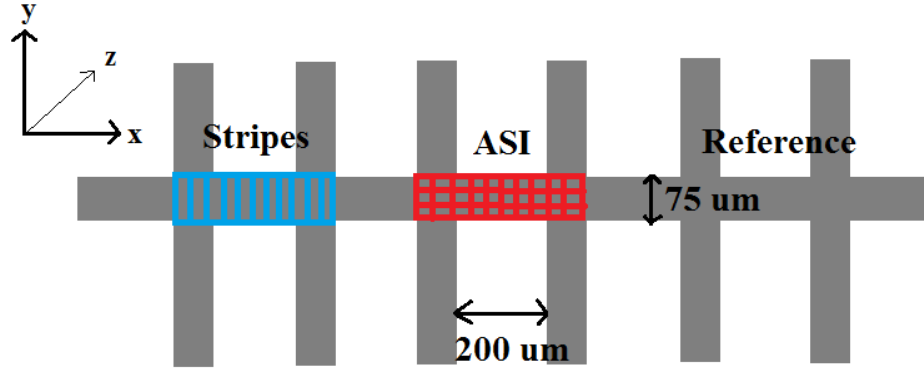

Figure 5.5: A sketch of the Hall bars used in this chapter showing the locations of the different sections, along with the dimensions of the Hall bar. The rest of the design was identical to that used in chapter 4. The axes define the x, y, and z directions. For clarity, the z-direction is the dimension that goes down perpendicular to the plane of the Hall bar surface, towards the 2DEG layer.

In order to ascertain whether any oscillations observed in the longitudinal resistance are due to the magnetic properties of the NiFe, it is necessary to rule out any other factors that might also result in oscillations in the resistance. One concern was that the process of EBL could leave the 2DEG with periodic regions of either depletion or enhanced electron density, which could then alter our results. To test whether or not this was the case, on one Hall bar we deposited the resist, patterned the sample using e-beam lithography, and developed the sample as usual, but we then removed all the resist rather than depositing any material on top to form stripes / ASI. This left a blank sample that had undergone the EBL process, so if there were any commensurability-like oscillations in the stripe or ASI sections then these could not be due to magnetic effects and must have been caused by the lithography process. Unless stated otherwise, owing to equipment constraints, the samples measured in this chapter did not undergo illumination prior to the measurements.
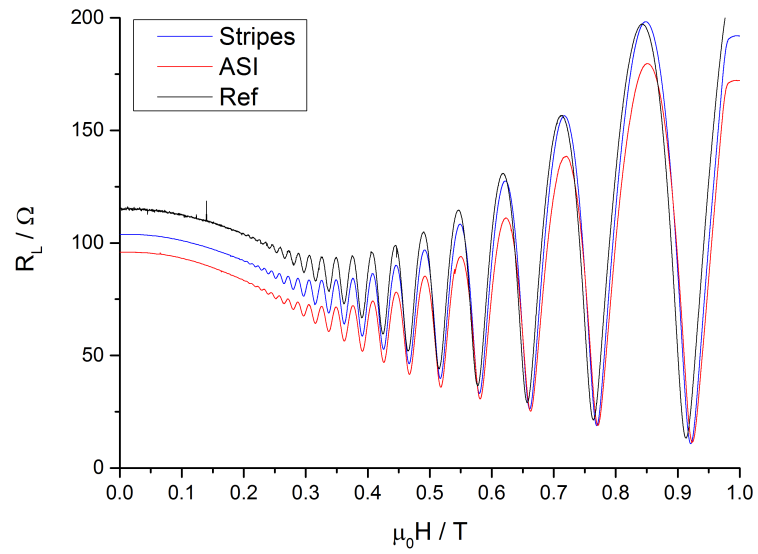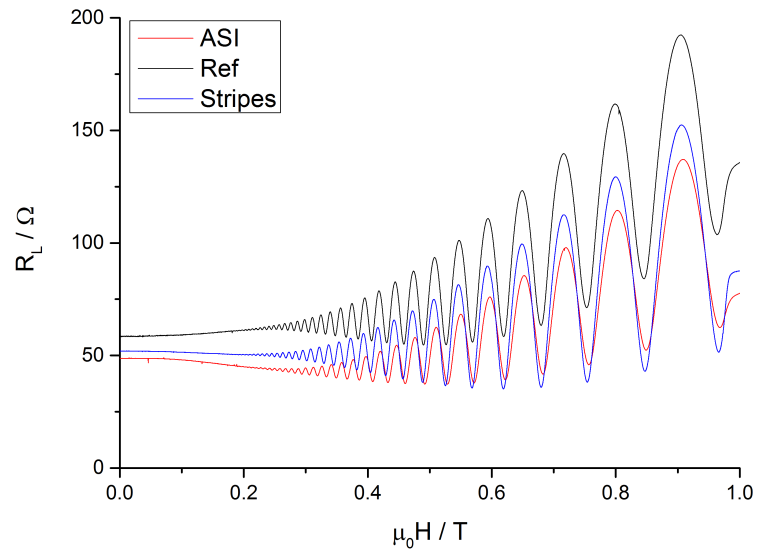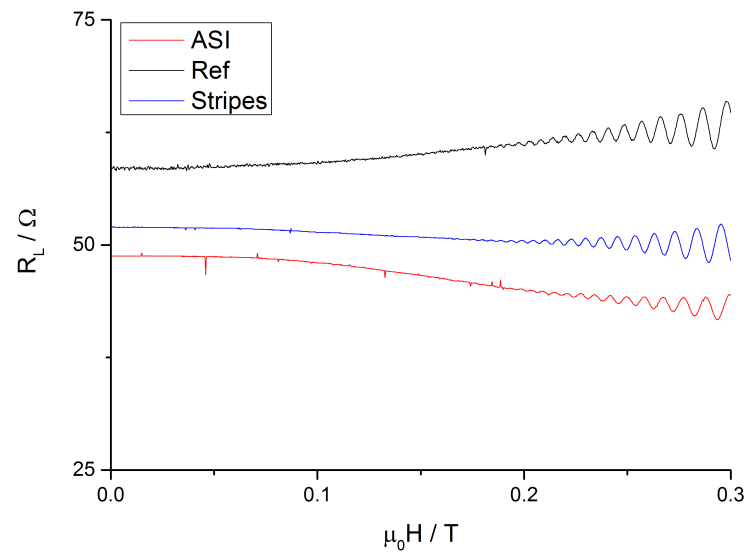
(a) Full measurement
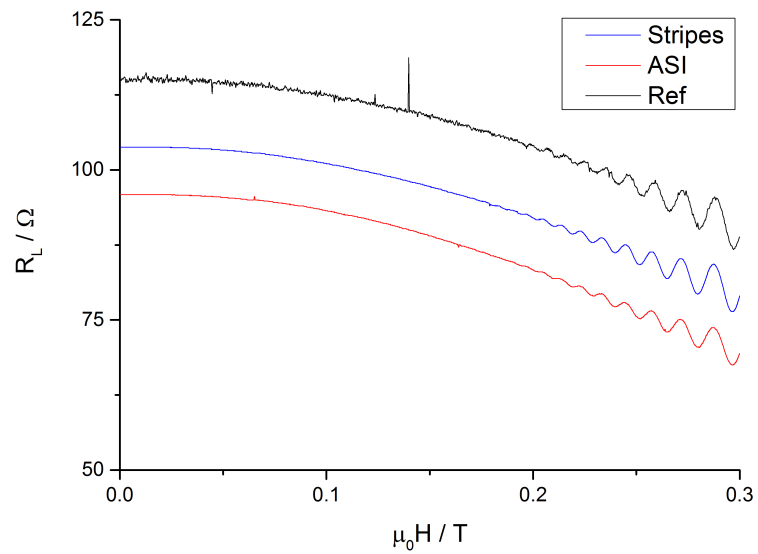
(b) Zoomed in to show 0 T to 0.4 T more clearly

Figure 5.6: Longitudinal resistance measurements of a sample that was patterned using e-beam lithography but had no material deposited on it, measured in the dark.

(a) Full measurement

(b) Zoomed in to show 0 T to 0.4 T more clearly

Figure 5.7: Longitudinal resistance measurements of a sample that was patterned using e-beam lithography but had no material deposited on it, measured in the light.

Figures 5.6 and 5.7 show the results of longitudinal resistance measurements taken at 1.4 K for applied magnetic fields between 0 T and 1 T, for both light and dark measurements. All three sections of the Hall bar show similar results; the only difference is that the magnitudes of the resistances for the different sections are not always equal, which could be attributed to having Ohmic contacts of varying quality. The key finding from this data is that there are no low-field oscillations present in the striped or ASI sections for either the dark or light results. This shows that performing EBL on a 2DEG does not cause commensurability-like oscillations in its longitudinal resistance, so EBL is a suitable method to use for the patterning of the striped and ASI sections for future samples.

5.4 SEM Effects on the Longitudinal Resistance

Scanning electron microscopy (SEM) is a useful technique for checking the quality of our ferromagnetic features. However, it is necessary to ensure that the high-energy, focused electron beams involved in the SEM process do not damage or otherwise affect the 2DEG. Several samples were fabricated on the same wafer simultaneously and SEM was performed on one of these samples. Resistance against applied field measurements were then taken of these samples, and the results for different samples were compared to check for changes such as increased resistances or extra oscillations.

Figure 5.8 shows the results obtained during this experiment. At 1.4 K, the sheet density for the samples that had not been in the SEM was 1.74×10^{11} cm^{-2} and had a mobility up to 553,000 cm^{2}V^{-1}s^{-1}. However, for the sample which had undergone SEM these figures were rather lower at 1.65×10^{11} cm^{-2} and 408,000 cm^{2}V^{-1}s^{-1} so we can see that the process of SEM can alter the properties of a 2DEG. Therefore, in order to maximise the mobilities and sheet densities for our samples, we only performed SEM on a representative range of samples from each batch and performed resistance measurements on the remaining samples.
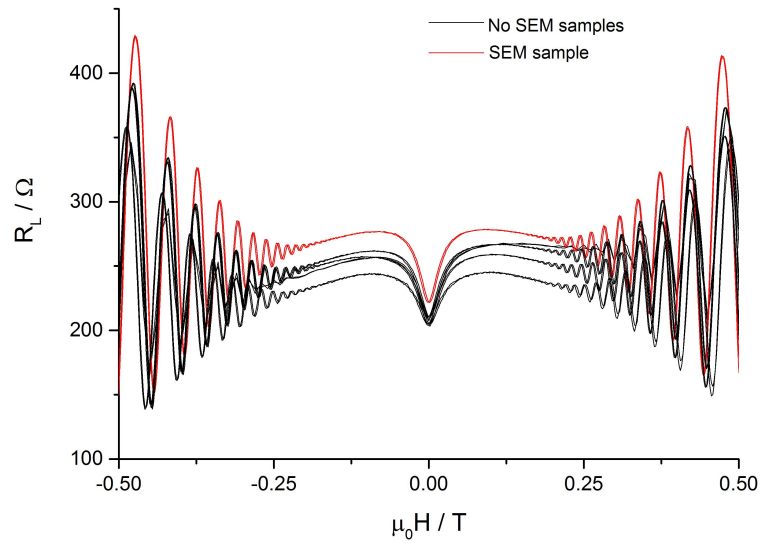
Figure 5.8: The effects of undertaking SEM measurements on a sample on its magnetoresistance. The sample that has undergone SEM is shown in red whereas other samples, fabricated at the same time, are shown in black.

5.5 ASI and the Quantum Hall Effect

Although the effects of ferromagnetic stripes and other periodic modulations on the Hall resistance have been documented [68], no literature was found on the effects of ASI on the Hall resistance of a 2DEG. Periodic stripes do not have an effect on the Hall resistance of a 2DEG owing to cyclotron orbit drift occuring equally in the $y > 0$ and $y < 0$ directions, thereby cancelling out to leave no overall effect [112].

Figure 5.9 shows the results from Hall resistance against applied magnetic field measurements taken for reference, striped and ASI sections of a Hall bar. With the results for ferromagnetic stripes already established by previous groups, we also measured Py stripes as a control. Our data shows that the deposition of ASI atop a 2DEG does not appreciably alter the Hall resistance. This is demonstrated in figure 5.9 by the reference (plain), striped and ASI sections all overlaying one another. We can explain these results using the same justification as for the ferromagnetic stripes. The

ρ_{xy} component of the resistance is not subjected to any periodic modulation since cyclotron orbits drift equally along the y > 0 and y < 0 directions which average out to leave no additional charge on the Hall probes, so no commensurability oscillations or other effects in the Hall resistance are observed for this system [68].
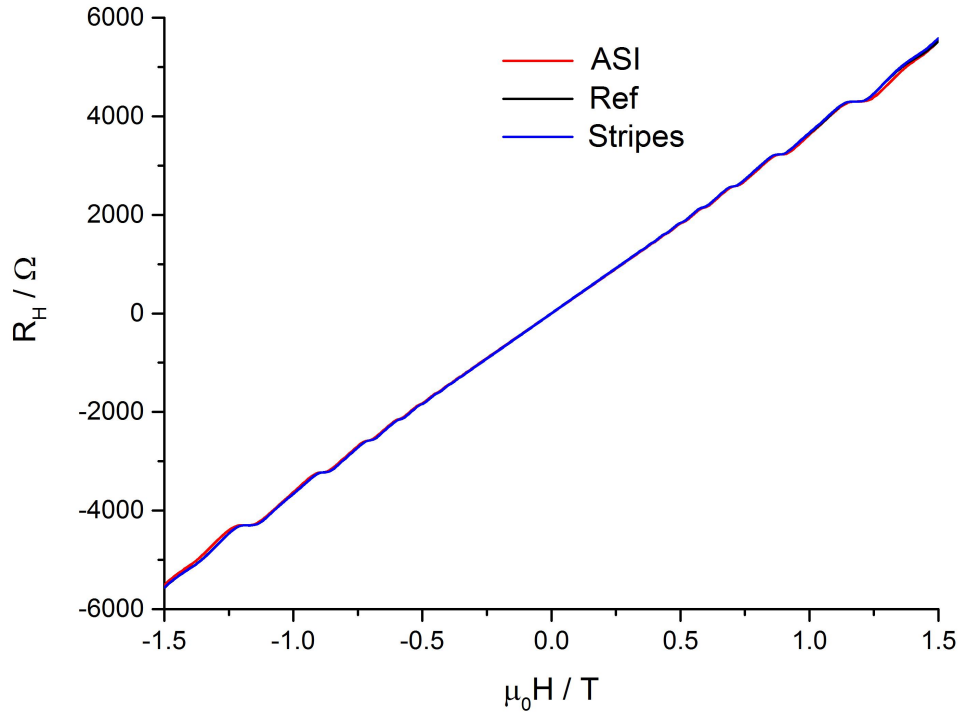

Figure 5.9: The Hall resistance for the reference, ASI and striped sections. The lines lie on top of one another, showing that there is no difference in the Hall resistance of the three sections.

5.6   Commensurability Oscillations in ASI

With the effects of ASI on the quantum Hall effect established in section 5.5, attention turns to the effects of ASI on the longitudinal resistance of a Hall bar. Permalloy ASI of length 200 nm, width 80 nm, height 100 nm and period 500 nm was fabricated

atop a GaAs-AlGaAs wafer containing a 90 nm deep 2DEG. An image representative of the ASI samples is shown in figure 5.11. Each Hall bar also contained a plain reference section, and a NiFe striped section with stripes spanning the width of the Hall bar with height 100 nm, width 200 nm and period 500 nm.
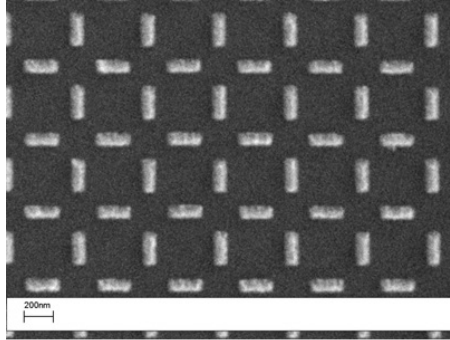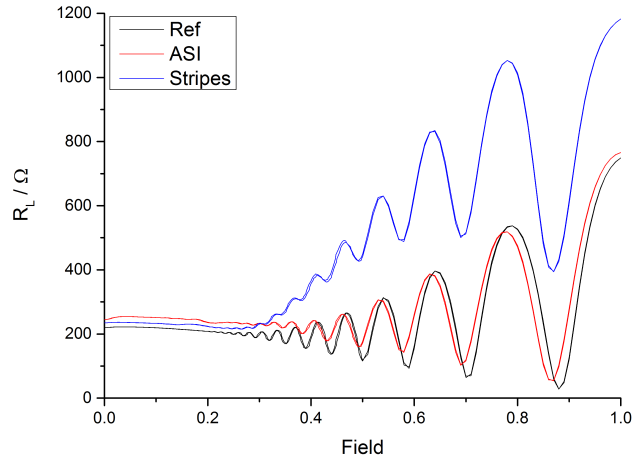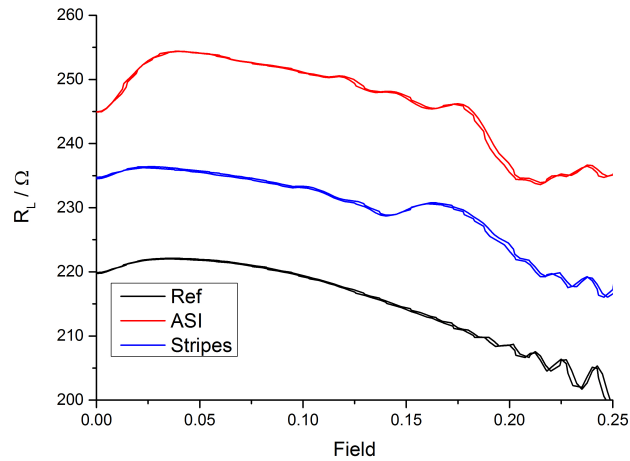

Figure 5.10

Figure 5.11: SEM image of the ASI patterned atop the Hall bars. Each individual element has dimensions $200 \times 80 \times 100$ nm with a period of 500 nm.

Transport measurements were performed at 1.5 K, recording the longitudinal resistance of each section of the Hall bar for applied magnetic fields between 0 T and 1 T. The results of these measurements are shown in figure 5.13, along with the magnetoresistance results obtained in Figure 4.11 for the strain reduced Ti stripes for comparison. The different carrier concentrations results in the SdH oscillations having minima at different applied magnetic fields for the different materials. The COs in the permalloy sections do appear to be more distinct than the COs in the Ti sample, suggesting that there is some effect occuring due to the magnetic properties of the material.

Forwards and backwards field sweeps can be seen in Figure 5.12. The samples show little evidence of hysteresis, which is unexpected for ferromagnetic structures, and for which we currently cannot provide an explanation.

(a) Full field sweep. There are forwards and backwards traces here, but they lie almost exactly on top of one another.


(b) Zoomed in to show the 0 T to 0.25 T range more clearly.

Figure 5.12: Forwards and backwards magnetic field sweeps for the magnetoresistance data. There is a lack of hysteresis in these samples.

The sheet density and mobility were found, using the $1/B$ periodicity of the SdH oscillations, to be 1.69×10^{11} cm^{-2} and 450,000 cm^{2}V^{-1}s^{-1} for the reference section and 1.65×10^{11} cm^{-2} and 403,000 cm^{2}V^{-1}s^{-1} for the ASI section. With the strain

minimised by fabricating the ASI normal to the [100] axis, any oscillations in the longitudinal resistance at low fields are likely to be due to the magnetic properties of the ASI. With the magnetic and strain oscillations out of phase, from the ($\lambda \pm 0.25$) component of their equations (equations 2.24 and 2.23), this means that the maxima of the magnetic oscillations are located at the same B field as the minima of the strain oscillations. Using the sheet density of the ASI section and a 500 nm period, the predicted locations of the minima and maxima of the magnetic commensurability oscillations are shown in table 5.1.
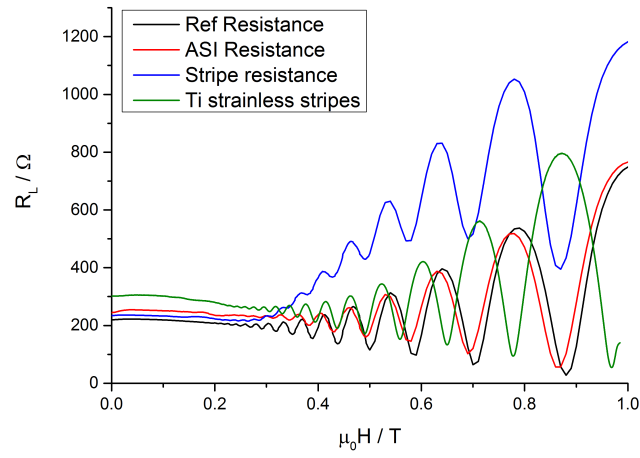
(a) The longitudinal resistance for the reference, striped and ASI sections of a Hall bar at a temperature of 1.5 K along with the Ti stripes results from Figure 4.11 for comparison.
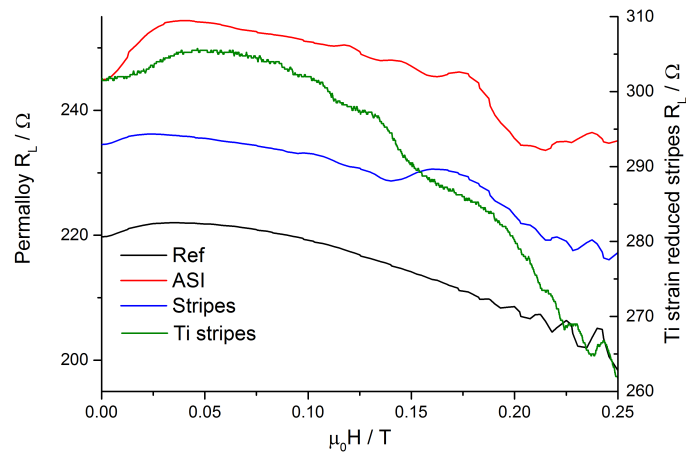
(b) The same data as above zoomed in to show the longitudinal resistance of the Hall bar sections at low applied magnetic fields. The Ti stripes are shown on a separate y-axis for clarity.

Figure 5.13: Magnetic commensurability oscillations in the ASI section of a Hall bar. There are oscillations present in the striped and ASI sections that do not occur in the reference section; these are the magnetic commensurability oscillations.

λ	Predicted values		Actual values	
	B_0 min / T	B_0 max / T	B_0 min / T	B_0 max /T
0	1.07	-	-	-
1	0.215	0.358	0.163	0.173
2	0.119	0.153	0.136	0.141
3	0.0826	0.0976	0.112	0.118
4	0.0631	0.0716	-	-

Table 5.1: Predicted minima and maxima of the magnetic commensurability oscillations of the ASI, using a sheet density of 1.65×10^{11} cm^{-2} and period of 500 nm. The predicted locations of the oscillations show little resemblance to the actual locations.

Similar to the piezoelectric strain discussed in chapter 4, the data in table 5.1 shows that the predicted and actual locations of oscillation minima and maxima are a poor fit when a period of 500 nm is used for the predictions. Since the ASI has length 200 nm and width 80 nm, table 5.2 shows the predicted locations of oscillation minima and maxima using these values for the period.

λ	Predicted values 200 nm		Predicted values 80 nm		Actual values	
	B_0 min / T	B_0 max / T	B_0 min / T	B_0 max / T	B_0 min / T	B_0 max /T
0	2.69		6.71			
1	0.537	0.895	1.34	2.24		
2	0.299	0.384	0.746	0.959		
3	0.207	0.244	0.516	0.610		
4	0.158	0.179	0.395	0.447	0.163	0.173
5	0.128	0.141	0.320	0.353	0.136	0.141
6	0.107	0.117	0.268	0.292	0.112	0.118
7	0.0926	0.0995	0.231	0.249		
8	0.0814	0.0867	0.203	0.216		
9			0.181	0.192		
10			0.164	0.172		
11			0.149	0.156		
12			0.137	0.143		
13			0.127	0.132		
14			0.118	0.122		
15			0.110	0.114		

Table 5.2: Predicted minima and maxima of the magnetic commensurability oscillations of the ASI, using a sheet density of 1.65×10^{11} cm^{-2} and periods of 200 nm and 80 nm.

From table 5.2, it could be argued that either the 200 nm or 80 nm are a fit for the actual locations of the minima and maxima of the commensurability oscillations. If the actual oscillations correspond to λ = 4, 5, 6 then the predicted oscillations of the 200 nm period match the actual values with errors between 0 % and 5.9%. The predictions are more accurate for the maximum locations, with a maximum error of 3.4 %, than for the locations of the minima, whose errors lie between 3.1 % and 5.9 %. For the 80 nm period, when λ = 10 and 12, the predicted oscillations

match the actual oscillations with a maximum error of 1.4 %. However, the 80 nm period predicts there to be many oscillations so statistically there would be more chance of the actual oscillations falling close to the predicted values. Moreover, these extra oscillations, most noticeably when $\lambda = 11$, show no signs of being apparent in the data. From this, we take the 200 nm period to be the most likely period that the oscillations have taken, and figure 5.14 shows graphically the proximity of the predicted and actual oscillations.

With a 200 nm period and sheet density of 1.65×10^{11} cm^{-2}, the predicted and actual positions of the oscillation maxima and minima are not a perfect match, particularly for the magnetic minima locations. This suggests that either the period or sheet density are inaccurate, the equation used to calculate the locations of the oscillations for ferromagnetic stripes does not hold for ASI, or there are other unknown factors that are affecting the data. However, there is a method whereby the actual locations of the minima (or maxima) can be used to obtain the period or the sheet density of the sample. Using equation 2.23, used for predicting the locations of the magnetic oscillation minima:

$$B_0 = \frac{2\hbar\sqrt{2\pi n_s}}{ea(\lambda + \frac{1}{4})},$$
(5.4)

this can be rearranged to form:

$$\frac{1}{B_0} = \frac{ea(\lambda + \frac{1}{4})}{2\hbar\sqrt{2\pi n_s}},$$
(5.5)

which rearranges further to become:

$$\frac{1}{B_0} = \frac{ea}{2\hbar\sqrt{2\pi n_s}}\lambda + \frac{ea}{8\hbar\sqrt{2\pi n_s}}.$$
(5.6)

Therefore, when a graph of $1/B_0$ against λ is plotted, the gradient, m, is equal to:

$$m = \frac{ea}{2\hbar\sqrt{2\pi n_s}},$$
(5.7)

This function consists solely of fundamental constants, the sheet density, and the period of oscillations. Using m and equation 5.7 the sheet density or period can be

calculated. For the sheet density:

$$n_s = (\frac{ea}{2\hbar m})^2/2\pi, \tag{5.8}$$

whereas for the period:

$$a = \frac{2\hbar m\sqrt{2\pi n_s}}{e}. \tag{5.9}$$

Likewise, when using the magnetic maxima of the oscillations (which is the same as the strain minima) and equation 2.24:

$$B_0 = \frac{2\hbar\sqrt{2\pi n_s}}{ea(\lambda - \frac{1}{4})}, \tag{5.10}$$

rearranges to form:

$$\frac{1}{B_0} = \frac{ea}{2\hbar\sqrt{2\pi n_s}}\lambda - \frac{ea}{8\hbar\sqrt{2\pi n_s}}. \tag{5.11}$$

Hence the graph of $1/B_0$ against λ for magnetic maxima has a gradient identical to that of the magnetic minima, so the sheet density and period can also be calculated using equations 5.8 and 5.9.

Figure 5.15 shows $1/B$ against λ for the minima found in figure 5.13. Unfortunately, there are few low field oscillations so the graph contains just three points. They lie in a straight line, although not perfectly, with a gradient of 1.397 ± 0.103 T^{-1}. With this gradient, a period of 200 nm and equation 5.8, the sheet density is calculated to be $1.92 \pm 0.17 \times 10^{11}$ cm^{-2}. This value for the sheet density is greater than that of the reference section. The sheet density would not be expected to be larger for a sample subjected to electron depletion than for a reference sample, so attention turns to checking that the periodicity is correct at 200 nm.

Using equation 5.9, the gradient above, and a sheet density of 1.65×10^{11} cm^{-2}, the period is calculated to be 188 ± 13.8 nm – a value 6% smaller than our expected period of 200 nm, but with a 7.3 % error. This can be explained using figure 5.16, an SEM image taken at an angle of $60°$. In this figure, the ASI is shown to be shaped as trapezoids rather than cuboids. This means that the edges of each element do not

have the full 100 nm height so are less able to influence the motion of the electrons in the 2DEG with their smaller magnetic field.
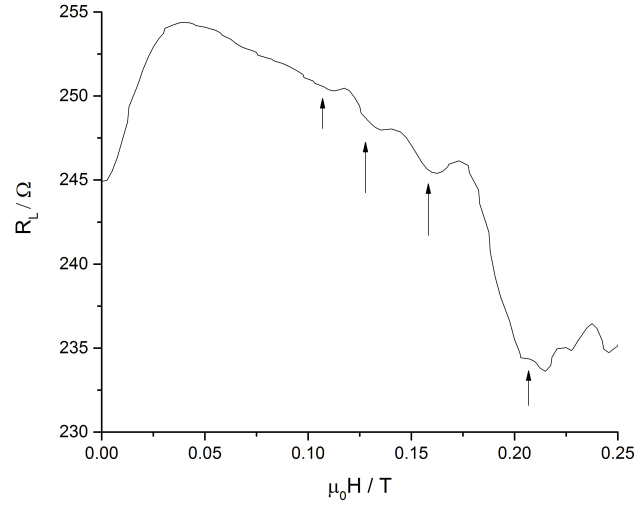
(a) Arrows show the predicted locations of the oscillation minima
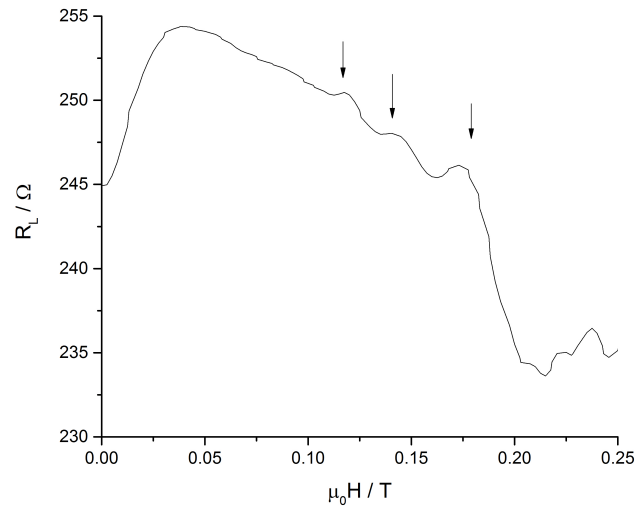
(b) Arrows show the predicted locations of the oscillation maxima.

Figure 5.14: The predicted and actual magnetic commensurability oscillations for a 2DEG with sheet density 1.65×10^{11} cm^{-2} with ASI of period 200 nm.
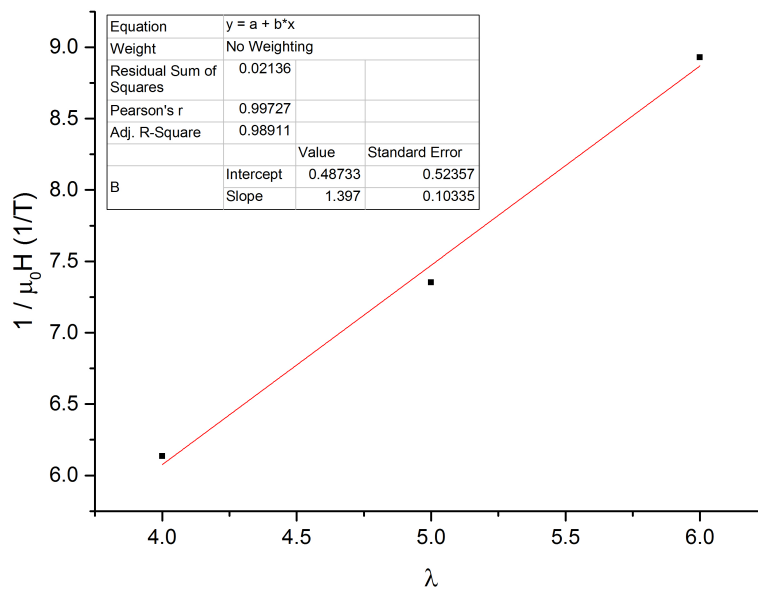
Equation	y = a + b*x	
Weight	No Weighting	
Residual Sum of Squares	0.02136	
Pearson's r	0.99727	
Adj. R-Square	0.98911	
	Value	Standard Error
B Intercept	0.48733	0.52357
Slope	1.397	0.10335

Figure 5.15: A graph of $1/B$ against λ. The gradient of this graph can be used to obtain the sheet density or the period of the ASI.
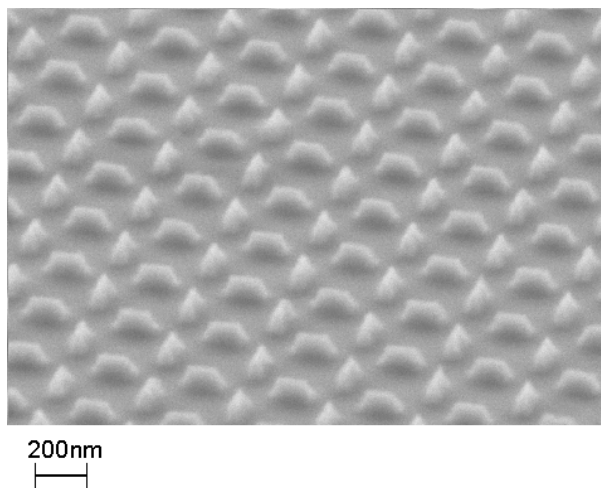

Figure 5.16: An SEM image taken at $60°$ shows that the ASI elements are shaped like trapezoids rather than cuboids, so the full 100 nm height is not present throughout the structure.

To determine how the magnetic field at the 2DEG is altered when the ferromagnetic structures are trapezoid shaped, rather than the cuboids we previously assumed, we can modify the equation used in our models in section 5.2:

$$B_{1,z}(x, z_0) = \mu_0 M \frac{hd}{a} \sum_{n=1}^{\infty} q_n F(q_n) e^{-q_n(z_0+h/2)} cos(q_n x - \theta).$$ (5.12)

In this equation, hd gives the cross-sectional area of the cuboid magnetic elements. This can easily be altered to give the cross-sectional area of a trapezoid, so the new equation to be used in our models is:

$$B_{1,z}(x, z_0) = \mu_0 M \frac{0.5h(d_1 + d_2)}{a} \sum_{n=1}^{\infty} q_n F(q_n) e^{-q_n(z_0+h/2)} cos(q_n x - \theta)$$ (5.13)

where d_1 and d_2 are the lengths of the parallel sides of the trapezoid. Using a height of 100nm, and lengths of d_1 and d_2 of 200 nm and 188 nm, the result of this model of the magnetic field strength at the 2DEG for trapezoid shaped magnetic structures is shown in figure 5.17. This figure also contains a graph showing the difference between the magnetic field strengths at the 2DEG of the cuboid structures and the trapezoid structures. We can see that having trapezoid magnets, rather than cuboid magnets, has little effect on the strength of the magnetic field at the 2DEG with a maximum difference between the two structures of just 2.5 mT.
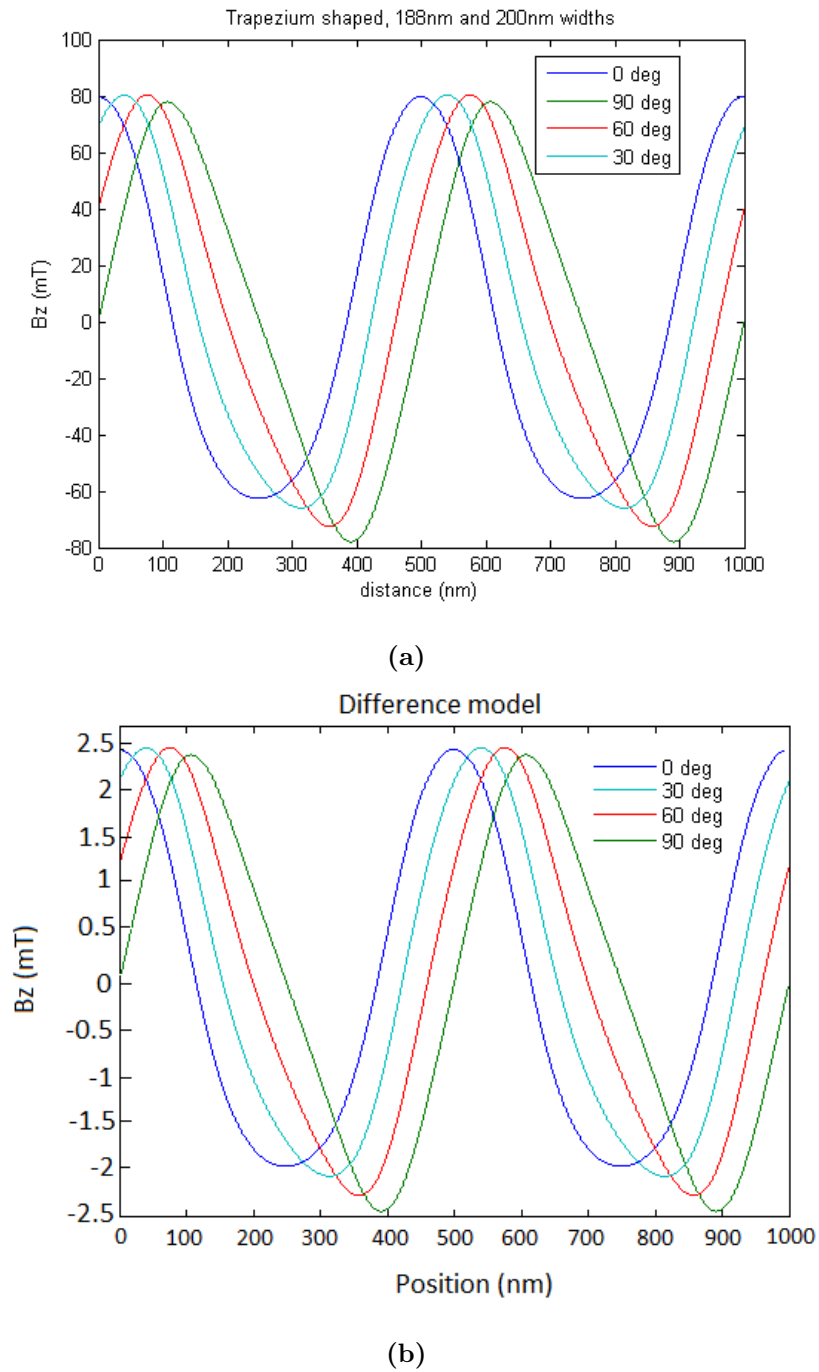
(a)

(b)

Figure 5.17: Graph (a) shows the magnetic field strength at the 2DEG for trapezoid shaped permalloy ferromagnetic magnets of height 100 nm, and with parallel sides with lengths of 188 nm and 200 nm. Graph (b) shows the difference between the magnetic field strengths for the cuboid structures modelled in section 5.2 and the trapezoid structures modelled above. These graphs have the same shape, only the scale is different.

The predicted maxima and minima for the oscillations, using a sheet density of 1.65×10^{11} cm^{-2} and period of 188 nm are shown in table 5.3. The predicted minima match the actual locations with errors between 0 % and 3.1 %, an improvement on the 3.1 to 5.9 % errors of the 200 nm period. However, the predicted maxima for the 188 nm period does not fit as well with the actual maxima locations with errors between 5.1 % and 10.4 %, greater than the 7.3 % error on the 188 nm period measurement. The 200 nm period, with its errors between 0 % and 3.4 % (or, alternatively, between 0 T and 0.006 T) is a much better fit for the maxima data than the 188 nm period.

	Predicted values		Actual values	
λ	B_0 min / T	B_0 max / T	B_0 min / T	B_0 max /T
0	2.86	-		
1	0.572	0.953		
2	0.318	0.408		
3	0.220	0.260		
4	0.168	0.191	0.163	0.173
5	0.136	0.150	0.136	0.141
6	0.114	0.124	0.112	0.118
7	0.0986	0.106		

Table 5.3: Predicted minima and maxima of the magnetic commensurability oscillations of the ASI, using a sheet density of 1.65×10^{11} cm^{-2} and period of 188 nm.

Although the predicted locations do not perfectly fit the data, the oscillations can still be attributed to magnetic commensurability effects. However, previously published papers on the subject of magnetic commensurability oscillations have also incurred this issue, without providing any explanations as to the causes of the discrepancies; these same papers confidently assert that their observations are due to magnetic commensurability oscillations. The best demonstration of this is by Ye *et al.* who observe magnetic commensurability oscillations when Dy stripes are patterned

atop a GaAs-AlGaAs heterojunction containing a 100 nm deep 2DEG, as shown in figure 5.18.
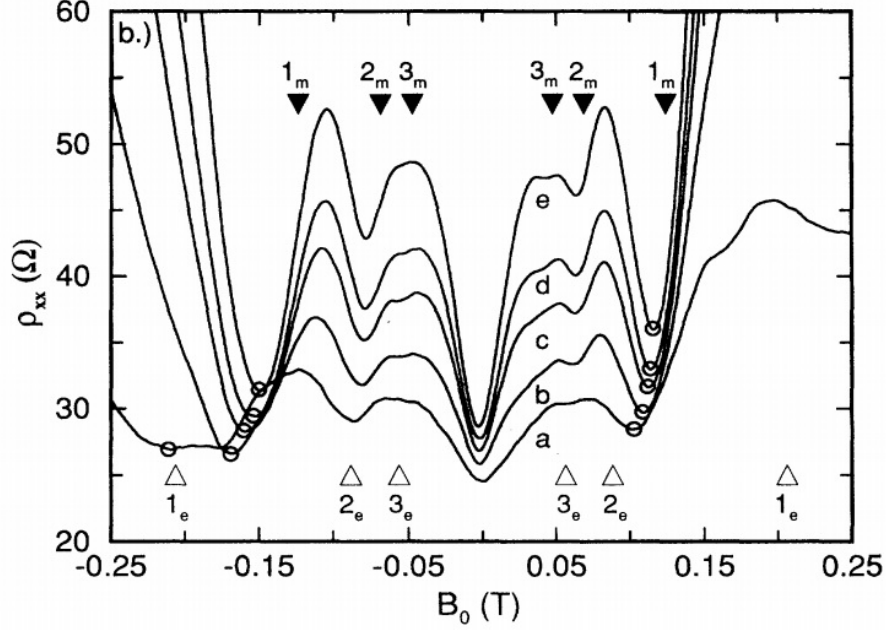

Figure 5.18: Figure taken from [69] demonstrating that the predicted locations of magnetic minima and maxima (indicated by triangles) do not perfectly coincide with the actual locations. The black triangles show the positions of the expected magnetic CO minima whereas the white triangles show the positions of the predicted electrostatic minima. The circles show the positions of the resistance minima which this group used to evaluate the amplitude of the stray magnetic field.

Equation 4.14 can be used to calculate the magnetoresistance relative to the zero field resistance [103]:

$$\frac{\Delta R_{xx}}{R_0} = [\frac{ak_F}{4\pi^2}(\frac{\hbar\omega_0}{E_F})^2(\frac{l_e}{l_m})^2 + (\frac{V_0}{E_F})^2(\frac{l_e^2}{aR_c})] \times$$
$$[1 - A(T/T_A) + A(T/T_A)\sin^2(\frac{2\pi R_C}{a} - \frac{\pi}{4} + \phi)]. \quad (5.14)$$

The first term in the first pair of brackets relates to the magnetic field modulation B_0 and the second term relates to the electric field modulation V_0. It is possible to determine V_0 and B_0 directly from the experimental data [103]. For relatively weak

magnetic modulation, $\sin(2\phi) \propto B_0/V_0$ so the phase difference 2ϕ can be obtained from the difference between the forwards and the backwards magnetic field sweeps. However, from Figure 5.12 we do not observe any hysteresis in these samples. Furthermore, the models shown in Figures 4.13 and 4.14 showed little correlation with the experimental oscillations obtained for reasons that were unknown, but not due to the estimate of V_0 as 1 meV since this factor merely changed the amplitude of the oscillations and not their locations. However, the amplitude of the modelled oscillations of up to 4.5 Ω is the same order of magnitude as the measured oscillations for the minimised strain Ti sample in section 4.5.3, so whilst the modelled oscillations will not be in the same locations as the experimental oscillations, we can use equation 5.6 to model the effects that different values of B_0 will have on the oscillations for this sample when $V_0 = 1$ meV. The same parameters used before in Figures 4.13 and 4.14 are used here for consistency, with B_0 values of 0.01 T, 0.02 T and 0.03 T in keeping with the results found in prior work [103] and [62], as well as a slightly larger value of B_0 of 0.05 T for comparison. The results using equation are shown in Figure 5.19 for the 500 nm period and Figure 5.20 for the 200 nm period sample.

The figures both show the effect of the phase angle ϕ on the oscillations, with all oscillations with the magnetic modulation B_0 shifted in comparison with the purely electrostatic modulation. For the 500 nm sample, the shift decreases slightly as the size of B_0 increases. Furthermore, for the 500 nm sample the magnitude of the oscillations increases as B_0 increases; this effect is also seen for the 200 nm oscillations but is not as pronounced. The oscillations in these figures are a poor fit for the experimental oscillations observed in terms of the locations of the oscillation minima and maxima, which is not surprising given that the purely electrostatic oscillations from which these are based were also a poor fit for the data.
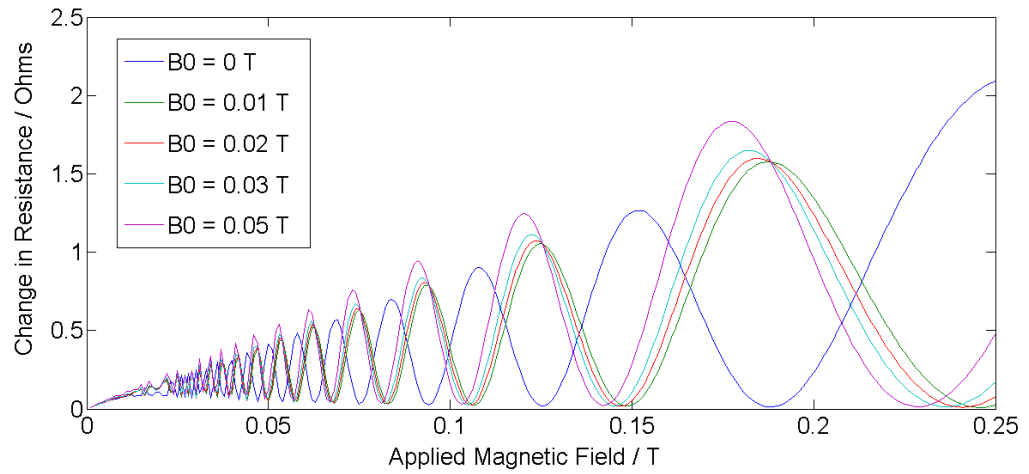
Figure 5.19: The predicted combined strain and magnetic oscillations in the NiFe sample using $n_s = 3.24 \times 10^{15}$ m^{-2} and period of 500 nm, and equation 5.6 for a range of B_0 values, with $V_0 = 1$ meV. The results from Figure 4.13 are also shown in this graph. These oscillations do not match the experimental oscillations observed.
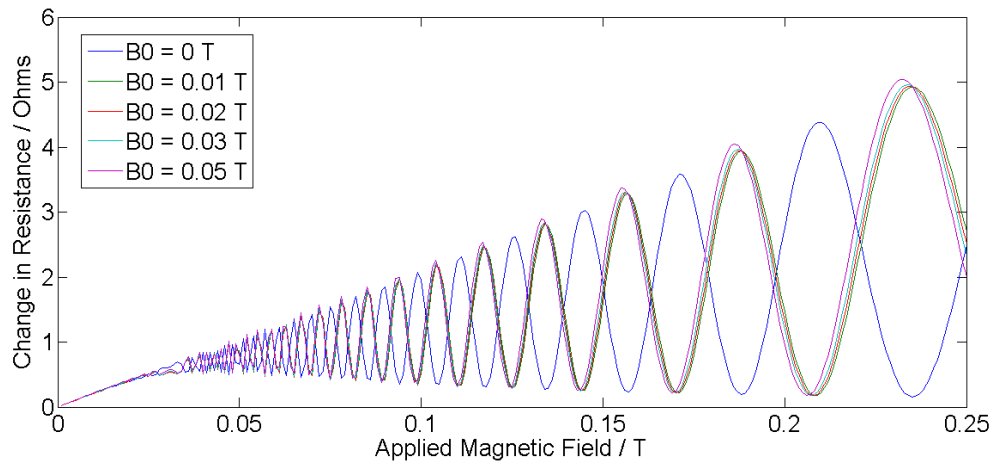

Figure 5.20: The predicted combined strain and magnetic oscillations in the NiFe sample using $n_s = 3.13 \times 10^{15}$ m^{-2} and period of 200 nm, and equation 5.6 for a range of B_0 values, with $V_0 = 1$ meV. The results from Figure 4.14 are also shown in this graph. These oscillations do not match the experimental observations observed.

The study of two-dimensional modulations in section 2.3.2 showed that the magnetoresistance oscillations in a two-dimensional modulation will still occur in the same locations as the minima and maxima of one-dimensional modulations calculated using equation 2.23 [11, 73], so having two-dimensional modulations does not explain why our predicted and experimental minima do not match, nor does it provide a different means of predicting where the minima are likely to occur. However, the simulations do show that the commensurability oscillations can be suppressed as the electric modulation in the y direction increases [71], so this may be a reason why our oscillations have a small magnitude.

To summarise, we have observed some oscillations in a 2DEG with an ASI array patterned atop. When using a period of 188 nm, the predictions for the locations of the magnetic minima are a good match for the data. However, the predictions of the magnetic maxima are a better match for the data when a period of 200 nm is used. The method used to obtain a period of 188 nm has its limitations with only three data points available to use in the $1/\mu_0 H$ against λ graph. More data is required to determine which period matches the commensurability oscillations best, or if there are indeed two periods that contribute to the commensurability oscillations. The data is therefore inconclusive as to the origins of these oscillations. We cannot be certain that the oscillations are due to the magnetic modulation of the 2DEG caused by the ASI, rather than the electric modulation caused by the piezoelectric strain between the wafer surface and the magnetic elements. The oscillations may also be being suppressed by electric or magnetic modulations along the y axis, as has been seen in previous work [71]. However, we know that the oscillations in a two-dimensional array should have the same minima and maxima as the oscillations in a one-dimensional array [11] so further work using either stronger magnets or a shallower 2DEG may help enhance the oscillations sufficiently for more progress to be made.

5.7 Temperature Dependence of COs

In this section we discuss how altering the temperature affects the commensurability oscillations that we observed in section 5.6. First, we verify that the SdH oscillations behave as expected at the base temperature of 1.5 K and when the samples are heated to temperatures of up to 10 K. We then study the behaviour of the COs in both the striped and ASI samples as the temperature increases.

Figure 5.21 shows the longitudinal resistance data of the reference, striped and ASI samples at a temperature of 1.5 K for applied magnetic fields between 0 T and 1 T. The SdH oscillations are clear and start to occur at about 0.3 T. At this scale, the commensurability oscillations are not visible in the low applied magnetic field regions of the striped and ASI sections. The longitudinal resistance of the striped sample begins to increase at about 0.3 T, which is not observed in either the ASI or reference sections.
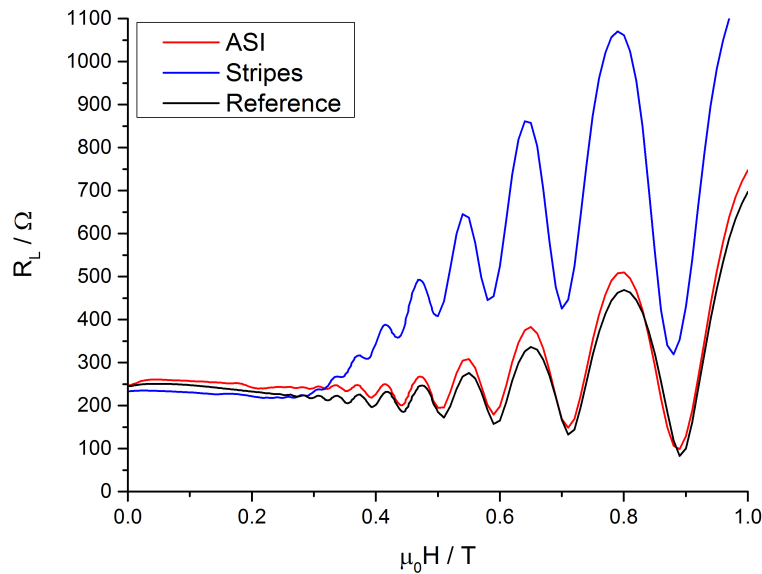

Figure 5.21: The longitudinal resistance for the reference, striped and ASI sections at a temperature of 1.5 K. There are clear SdH oscillations in all sections that commence at magnetic fields of approximately 0.3 T.
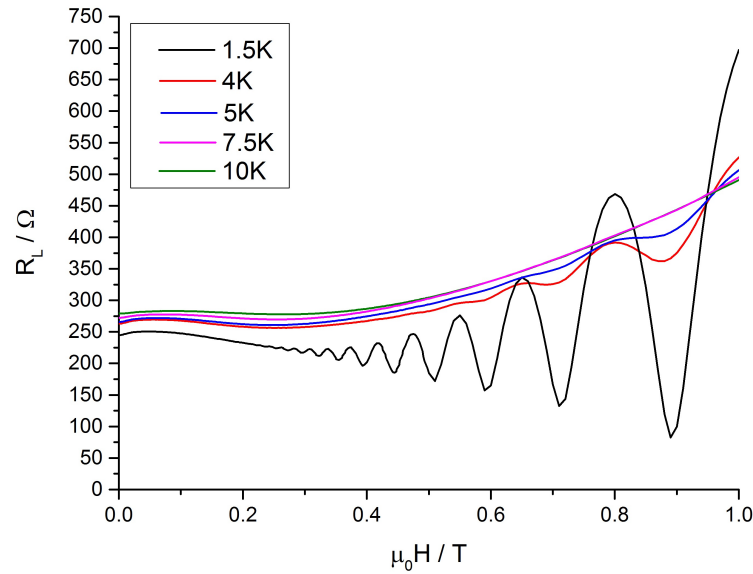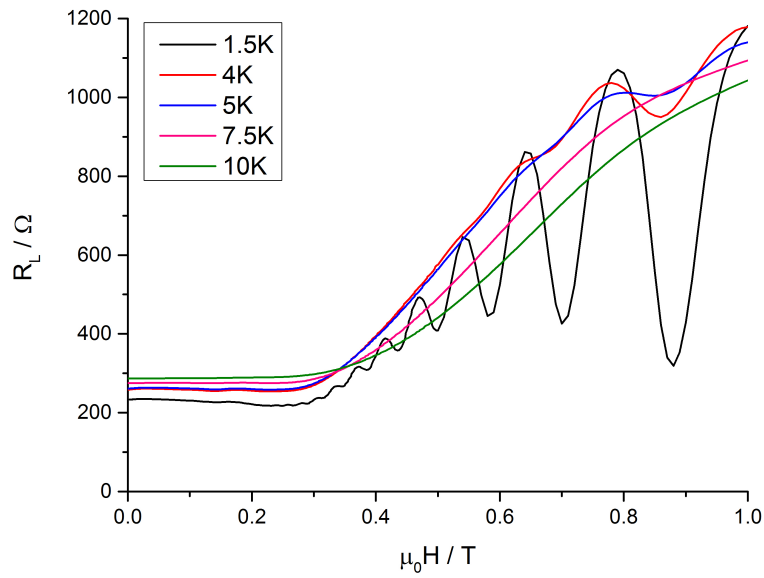
Figure 5.22: The longitudinal resistance of the reference section of a Hall bar for a range of temperatures. As the temperature increases the SdH oscillations quickly disappear.

The temperature dependence of the longitudinal resistance of the reference section is shown in figure 5.22. The reference section shows clear SdH oscillations that quickly diminish in amplitude as the temperature increases until at 7.5 K there are no more SdH oscillations.

Figures 5.23 and 5.24 show, respectively, the longitudinal resistances of the striped and ASI sections of a Hall bar for a range of temperatures. Each figure consists of two parts: one figure showing the full 0 T to 1 T measurements, and the other figure containing just the low field measurements from 0 T to 0.25 T to show the commensurability oscillations more clearly. For both the striped and ASI sections, the SdH oscillations decrease with temperature, as expected. The commensurability oscillations are also shown to be temperature dependent, with the COs for both sections decreasing as the temperature increases.

The ASI section shows some unexpected but interesting results at higher magnetic fields as the temperature increases. For the striped section, the magnetoresistance

undergoes a sharp increase in magnitude at a field of approximately 0.3 T at all temperatures. However, the ASI does not show this behaviour at 1.5 K, but does have this sudden increase at higher temperatures. The explanation for this behaviour is currently unknown, but this could be an avenue for further research.
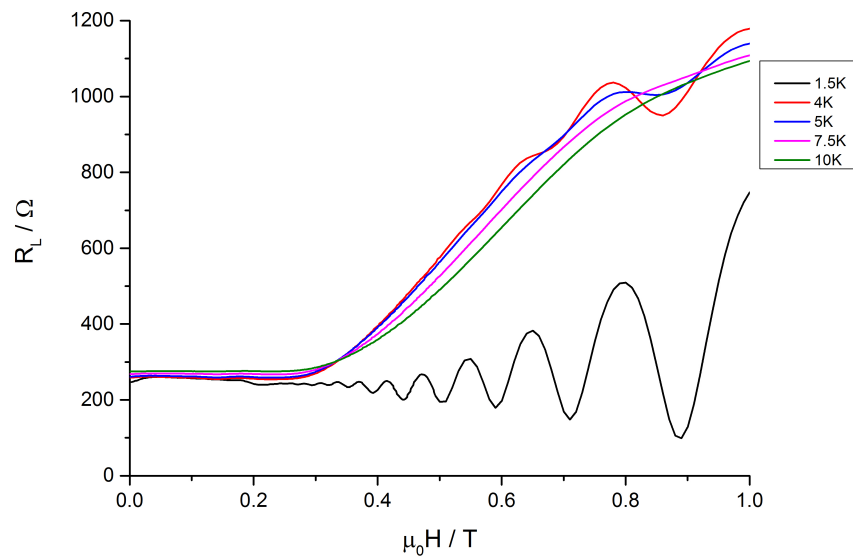
(a) The longitudinal resistance for the striped section of a Hall bar for a range of temperatures.
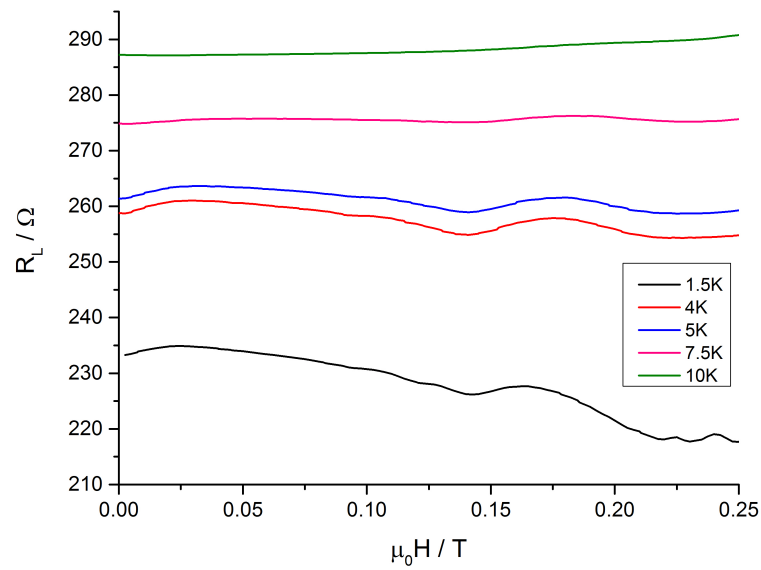
(b) The data from figure (a) zoomed in to show the data at low applied magnetic fields. This figure shows that the commensurability oscillations are temperature dependent, with the oscillations disappearing at higher temperatures.

Figure 5.23

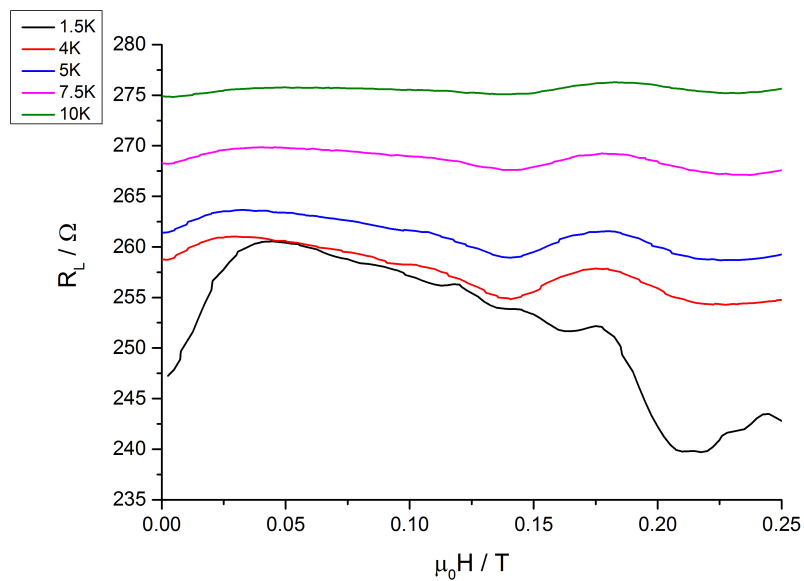**(a)** The longitudinal resistance of the ASI section of a Hall bar for a range of temperatures.

(b) The data from figure (a) zoomed in to show the data at low applied magnetic fields. This figure shows that the commensurability oscillations are temperature dependent, with the oscillations disappearing at higher temperatures.

Figure 5.24

5.8 Angular Dependence Measurements

Previous work has shown [10] that altering the angle of magnetisation θ of the stripes, by applying the external magnetic field at an angle that is not completely out-of-plane, can enhance the commensurability oscillations produced in the longitudinal resistance since the magnets reach magnetic saturation more rapidly. This enhancement includes both an increase in the magnitude of the oscillations, and an increase in the number of oscillations present. The model in figure 5.1 confirms that a larger applied field angle produces a stronger stray magnetic field at the 2DEG for this device, hence the enhancement in the commensurability oscillations.

For our devices, on a 90 nm deep 2DEG, our model (figure 5.2) does not show a change in the magnitude or profile of the stray magnetic field for different applied field angles. Therefore, we expect no enhancement in the commensurability oscillations for different angles for these devices.

Figures 5.29, 5.30 and 5.31 show these results plotted against the perpendicular component of the applied magnetic field – obtained by multiplying the applied magnetic field by sin10. These results again show that the magnetic modulation is not larger at the larger angle, since the oscillations seen are simply SdH oscillations moved to a lower magnetic field. Ideally, these experiments need to be repeated using a semiconductor substrate with a shallower 2DEG, since our models showed that the current wafers have the 2DEG too deep for the different angle of magnetic field to cause larger magnetic modulations.
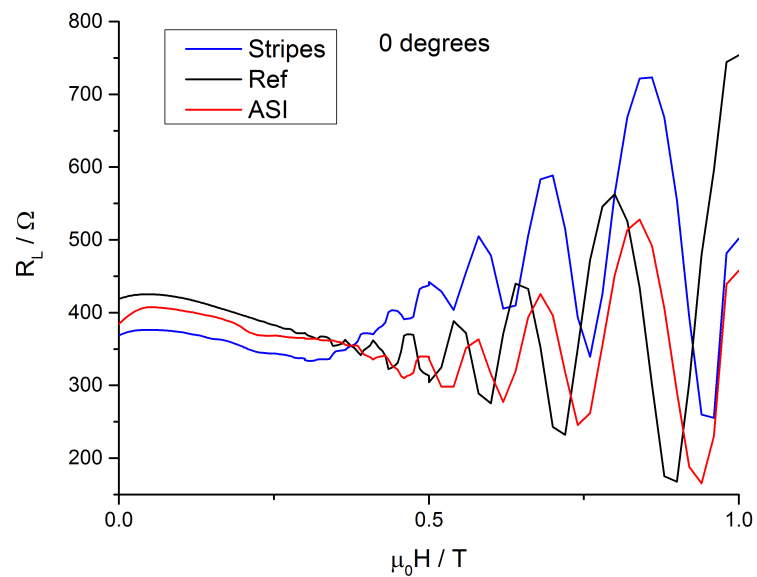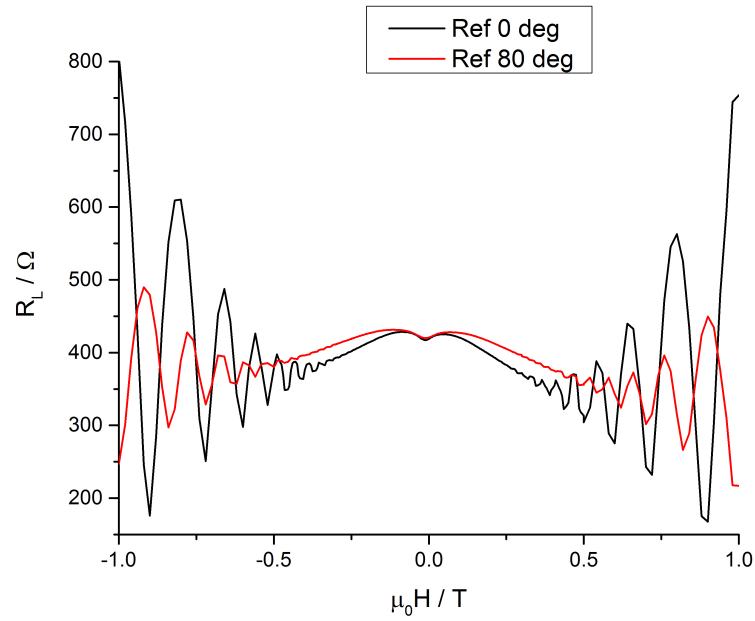
Figure 5.25: Longitudinal resistance data for the reference, striped and ASI sections at 1.4K for an out of plane applied magnetic field.

(a) Full data
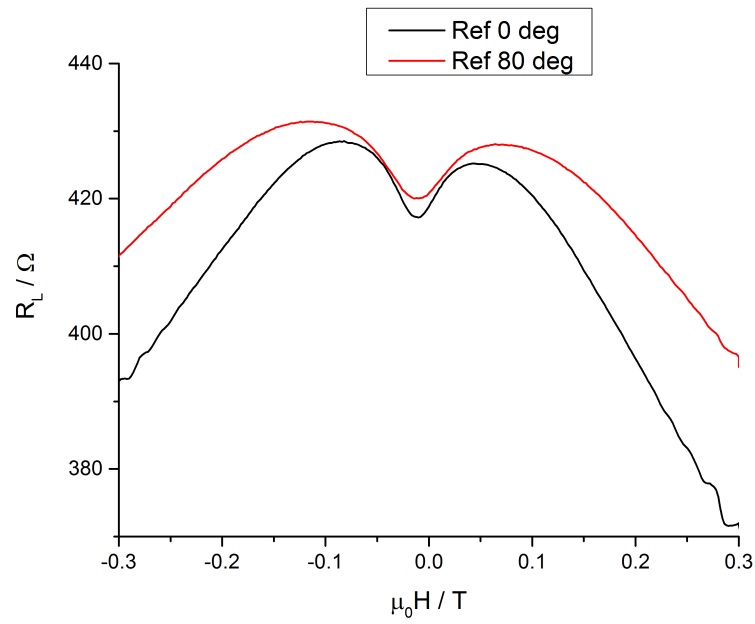
(b) Low magnetic field data

Figure 5.26: The resistance of the reference section for a completely out of plane magnetic field, and a field applied at 80°. Figure (b) zooms in to the low field section of figure (a). As expected, no COs are observed in the reference section.
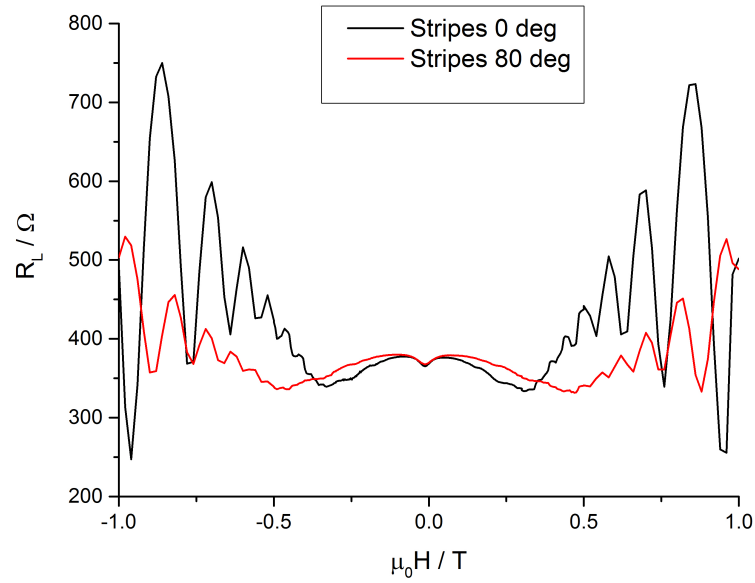
(a)
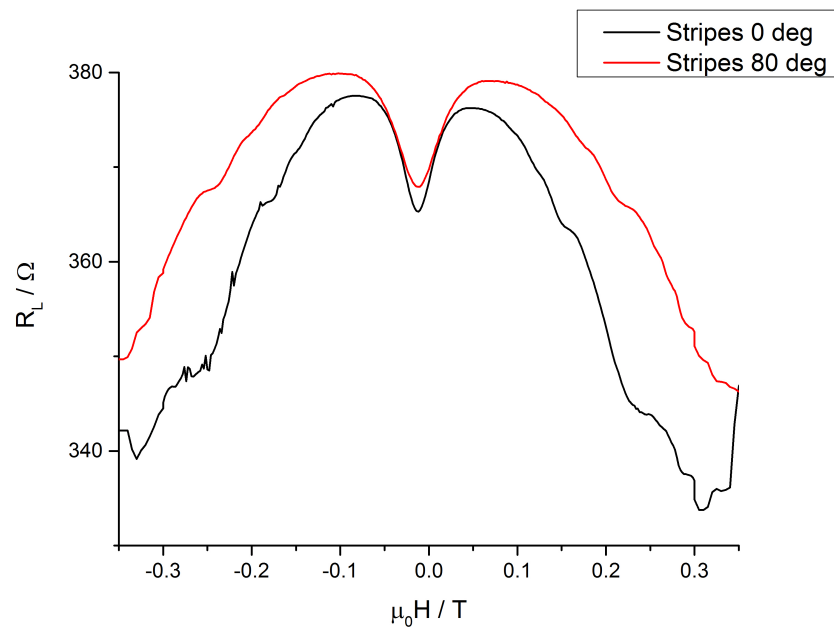
(b)

Figure 5.27: The resistance of the striped section for both an out of plane magnetic field, and a field applied at 80°. There is no enhancement of the COs with an increased angle, as predicted by our model. Figure (b) zooms in to the low field section of figure (a).
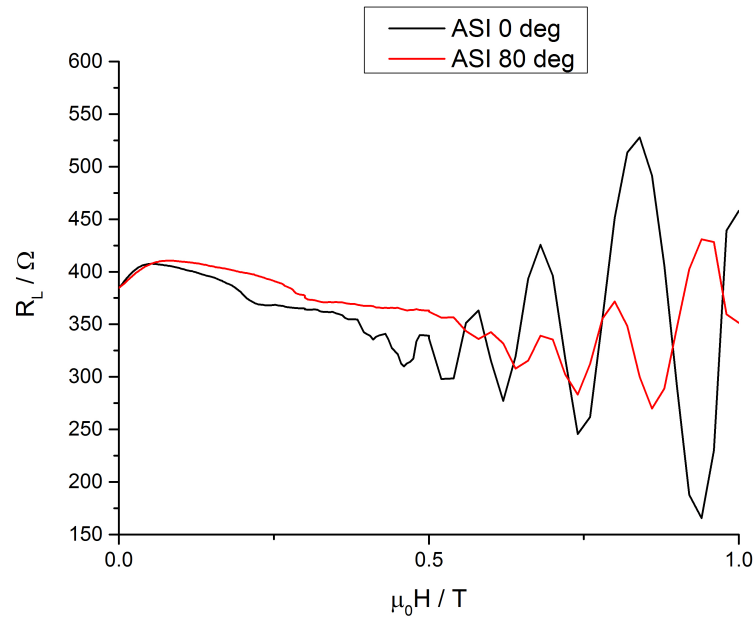
(a)
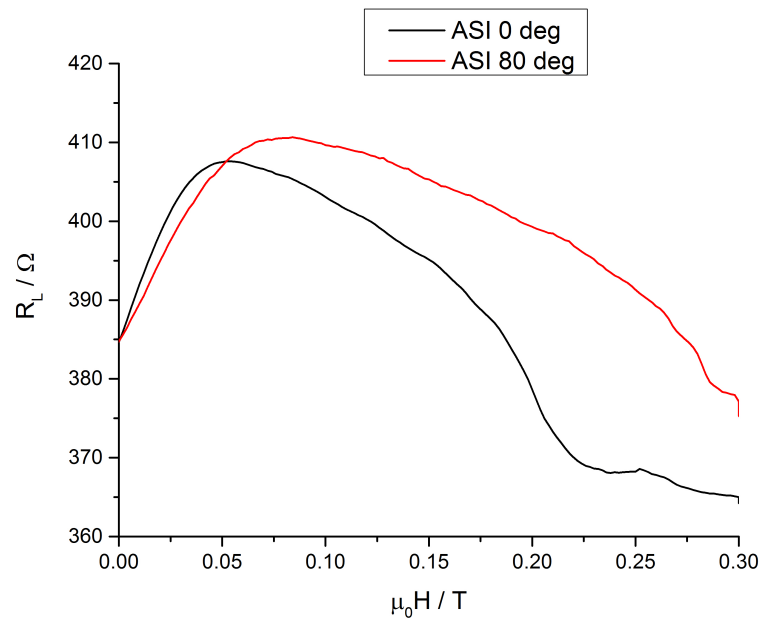
(b)

Figure 5.28: The resistance of the ASI section for both an out of plane magnetic field, and a field applied at 80°. Similar to the striped section, and as our model predicts, there is no enhancement of the COs as the angle of the applied magnetic field increases. Figure (b) zooms in to the low field section of figure (a).

Figure 5.29: Reference magnetoresistance data plotted against the perpendicular component of the magnetic field. The large oscillations in the 80° are due to the SdH oscillations

Figure 5.30: Striped magnetoresistance data plotted against the perpendicular component of the magnetic field. The large oscillations in the 80° are due to the SdH oscillations, and there is again no enhancement of the COs with angle.
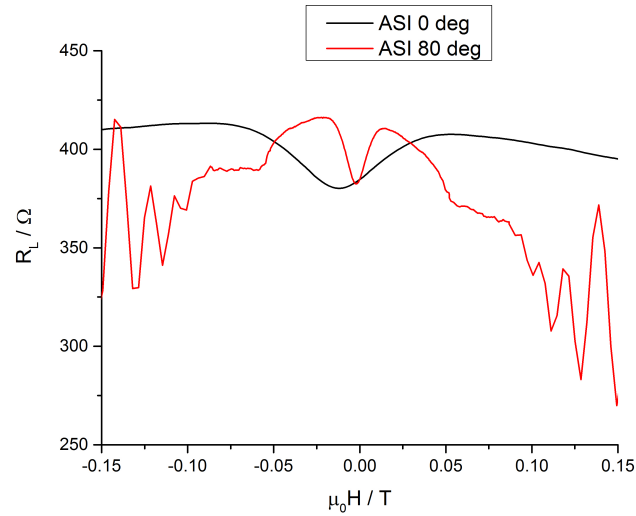
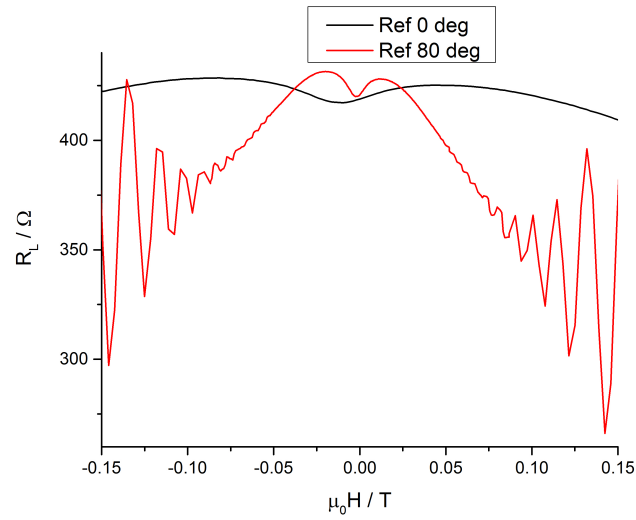**Figure 5.31:** ASI magnetoresistance data plotted against the perpendicular component of the magnetic field. The large oscillations in the 80° are due to the SdH oscillations, and there is again no enhancement of the COs with angle.
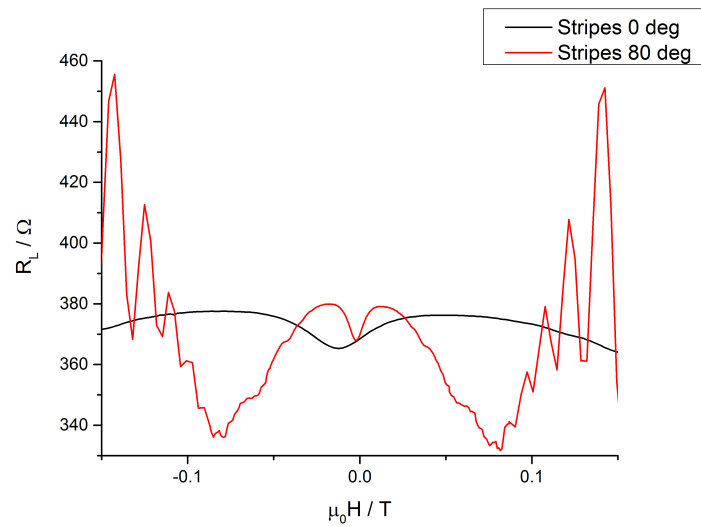
5.9 Summary

In this chapter we discussed the first commensurability oscillations observed in combined 2DEG / ASI structures. These occur at low applied magnetic fields and cryogenic temperatures.

First we discussed the models, based upon a Fourier analysis of Maxwell's equations, which showed the strength of the magnetic field at the 2DEG caused by the ferromagnetic structures patterned onto the substrate. By comparing our models with those of other groups, who had previously observed commensurability effects in combined 2DEG / striped structures, we showed that our magnetic features would produce a sufficiently strong magnetic field at the 2DEG to result in commensurability oscillations.

We then performed experiments to prove that any observed effects would not be due to artifacts from the fabrication process, and showed that performing EBL and SEM on our samples would not affect our results. After establishing that any com-

mensurability effects could only be caused by the magnetic field of the ferromagnetic structures, we measured the Hall resistance as a function of applied magnetic field for the reference, striped and ASI sections of our Hall bar. The ASI caused no new effects in the Hall resistance of the sample, in line with previous work showing that the presence of ferromagnetic stripes has no effect on the QHE. We explained this by considering the motion of the cyclotron orbits – they drift equally along the y > 0 and y < 0 directions so cancel out to leave no net additional charge on the Hall probes.

Next, by measuring the longitudinal resistance at low applied magnetic fields, we made the first observation of commensurability oscillations in a combined 2DEG / ASI structure. The locations of the oscillation minima and maxima were shown to not be dependent upon the period of the ASI, as initially expected, but on the width of the ASI instead. However, this is an indication that the commensurability oscillations may be caused by the strain between the wafer surface and the ASI rather than the magnetic effects of the ASI on the 2DEG. The cause of the observed oscillations is currently inconclusive since the locations of the oscillations do not match the predicted locations or the models. The oscillations are also rather small in magnitude, which could be a sign of the suppression seen in previous simulations undertaken on commensurability oscillations of two-dimensional modulations. Further work will need to be performed to ascertain the origin of these oscillations.

Finally, we discussed both the temperature dependence and the angular dependence of the commensurability oscillations. We found that as the temperature increased, the commensurability oscillations became weaker. Altering the angle of the applied magnetic field had no impact on the commensurability oscillations, confirming the predictions made using our models.

Chapter 6

Thermally-Activated Magnetization Dynamics of Artificial Spin Ice

6.1 Introduction

This chapter discusses the thermally-activated magnetization dynamics of square ASI. In particular, we present the first data showing how the proportion of different vertex types changes with temperature when commencing with an ordered array of type 2 vertices and progressing towards a ground state configuration.

A series of MFM images of two different FePd alloys allows us to determine how the presence of Pd affects the dynamics of the ASI. Moreover, we also use three different lattice spacings of ASI to ascertain the effects of the period on the thermal dynamics.

Vibrating sample magnetometry (VSM) measurements are used to determine the relative magnetization strengths of the two materials at temperatures up to 295 K. From our data, we calculate and compare the blocking temperatures of the different materials, and the magnetizations at these temperatures.

6.2 Experimental Methods

6.2.1 Sample Fabrication

The samples used in this chapter were fabricated by Dr. Sophie Morley. For the first sample, a 2 nm Pd layer was sputtered onto a SiO_2 wafer. Pd and Fe were then sputtered at powers of 5 W and 10 W, respectively, for a period of 600 s to give an overall PdFe thickness of 30 nm. The Fe : Pd ratio in this sample was 1 : 1.9.

For the second sample, a 2 nm Pd layer was again sputtered onto a SiO_2 wafer. Pd and Fe were then sputtered at powers of 10 W and 13 W, respectively, for a time of 300 s to give an overall PdFe thickness of 33 nm. The Fe : Pd ratio in this sample was 1 : 3.5. The Fe/Pd ratio was calibrated using low angle x-rays to measure the thickness of thin films of each material when sputtered at different powers [113]. A Bruker Diffractometer was used to obtain interference patterns of the scattered x-rays from the interface between different density layers, which could then be fit using the Kiessig method [114]. The Fe/Pd ratio of the low Pd sample was 1 : 1.87 ± 0.05 and the high Pd sample was 1 : 3.5 ± 0.1.

The remainder of the fabrication process for these two samples was identical, and occurred simultaneously. A primer, used to promote resist adhesion, was spin-coated onto the samples at a speed of 4 krpm for 40 s and baked at 180°C for 1 minute. Next, a resist comprised of ZEP520A and anisole with a 1 : 1 ratio was spin-coated onto the samples at 4 krpm for 40 s and baked at 180°C for 3 minutes.

The ASI pattern was written using e-beam lithography in the JEOL-6300 using a 100 kV electron beam and a dose of 190 $\mu C/cm^2$. The samples were then developed for 60 s in N50 solution and rinsed with IPA. Next, a 15 nm Ti layer was deposited onto the samples using the e-beam evaporator at a rate of 1 Å/s. Lift-off was performed using remover 1165, and afterwards the samples were washed in H_2O, acetone, and IPA and dried with N_2 gas.

Finally, the Ti layer was removed by ion-milling in argon gas for 70 s, using a 29 mA beam current and a 100 V accelerating voltage at a working pressure of

$\approx 1 \times 10^{-5}$ Torr. This process resulted in 30 nm thick PdFe ASI structures, with length 250 nm and width 80 nm, on a SiO$_2$ substrate.

6.2.2 Experimental Procedure

After the samples were fabricated, a large saturating magnetic field was applied by a permanent magnet to align the ASI into ordered type 2 arrays and AFM and MFM images were taken of each sample. They were then heated in an annealer, in a nitrogen rich atmosphere to prevent oxidation, for 2 minutes and then allowed to cool back down to room temperature over a period of 15 minutes. Further MFM and AFM images were then recorded at room temperature. This allowed any changes to the magnetic configuration of the ASI to be tracked. This heating, cooling and reimaging process of the same sample was repeated at higher temperatures using approximately 20°C intervals.

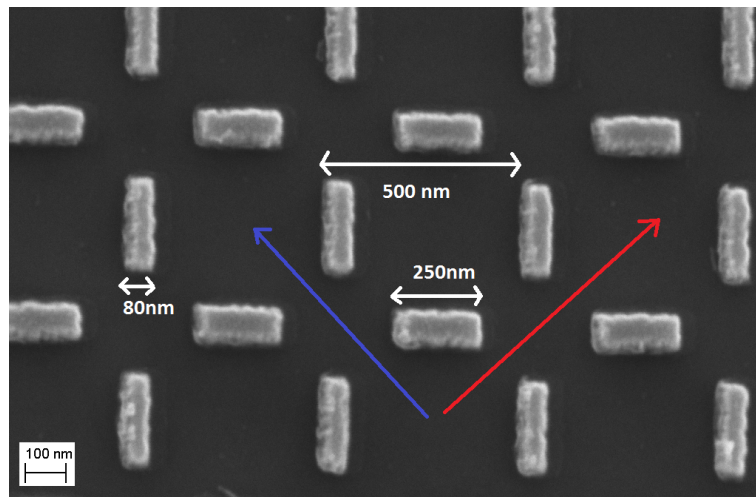**Figure 6.1:** SEM image of an example of the ASI elements with period 500 nm and dimensions 250 nm × 80 nm. The dimensions for all the ASI arrays used in this experiment was kept the same, only the period changed. The samples were initially magnetized along the red arrow for the high Fe / low Pd sample, and along the blue arrow for the low Fe / high Pd sample.
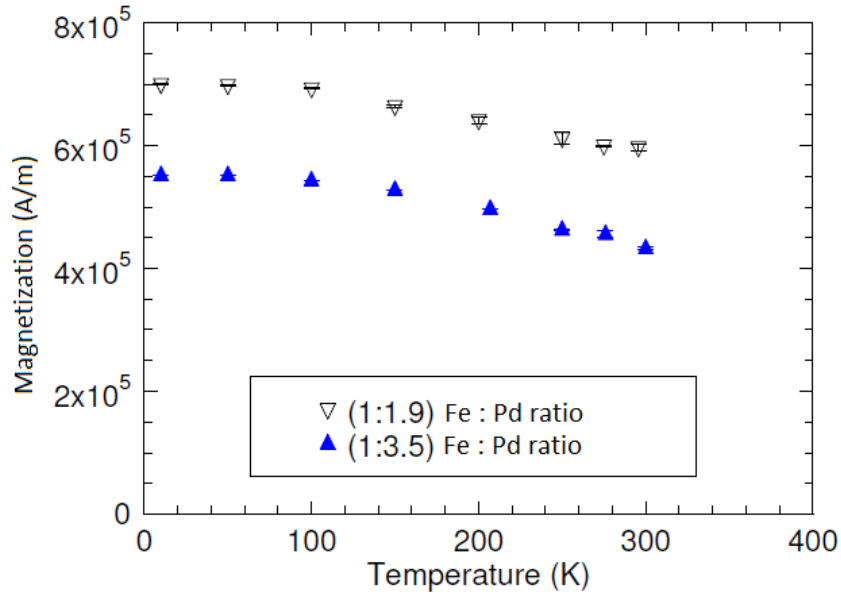
Figure 6.2: VSM measurements showing the magnetization strengths of two thin films of different FePd alloys as a function of temperature.

6.3 Magnetization Strengths of the Materials

When two different magnetic materials are being compared, it is useful to know their relative magnetization strengths. Using a vibrating sample magnetometer (VSM), we measured the magnetization as a function of temperature between 10 K and 295 K for a thin film (30 nm) sheet of each material. This was the maximum temperature that could be measured in the VSM, although ideally data would have been taken up to the Curie temperature of the material. The results are shown in figure 6.2 where the 1 : 1.9 FePd sample is shown to have a magnetization approximately 1.3 times greater than the 1 : 3.5 FePd sample.

With this information, it is possible to calculate the temperature required to flip the magnetic moment of a nanoisland. The shape anisotropy, $E_A = \frac{1}{2}\mu_0 M_S^2 \Delta N V = KV$, is the energy barrier that has to be overcome for the magnetic moment to flip. In this expression, K is the shape anisotropy constant, V is the volume, M_S is the

magnetization and ΔN is the difference between the demagnetizing factors. ΔN is calculated using the formulae in reference [115], and found to be approximately 0.22 for our samples. The blocking temperature, T_B, that would be required for the moment to flip can be estimated using $E = k_B T$. However, according to the Néel-Brown relaxation model, the magnetization of a material relaxes according to the length of time for which a material is held at a temperature. The magnetization relaxes according to:

$$M = M_0 e^{-t_m/\tau}, \tag{6.1}$$

where M is the final magnetization, M_0 is the initial magnetization, t_m is the holding time and τ is the relaxation time, which decreases with increasing temperature:

$$\tau = \tau_0 e^{\Delta E/k_B T}, \tag{6.2}$$

where τ_0 is typically around 10^{-9} s. This results in the following equation for determining the blocking temperature, T_B, of a magnetic structure:

$$T_B = \frac{KV}{k_B ln(t_m/\tau_0)} \tag{6.3}$$

For the high Pd sample, M_S at room temperature is 4.33×10^6 A/m. Therefore, for our samples of $250 \times 80 \times 30$ nm, a temperature T_B of approximately 6350 K is required to make the magnetic moments flip. For the low Pd sample, with a magnetization of 5.97×10^6 A/m the necessary temperature is approximately 12100 K. In reality, the FePd magnetic moments are going to flip at temperatures close to the Curie temperature, which is 260°C for bulk PdFe [58]. The large discrepancy between the calculated values and the experimental values is caused by the magnetization rapidly decreasing as the temperature increases, which is not accounted for in the formulae. However, from our experimental data, we will be able to determine the blocking temperature of our samples, which we shall define as the temperature at which half of the magnetic vertices have changed from their original state. From this, we will be able to calculate the value of the magnetization for the two materials at this temperature.

Iron content, atomic percentage	1.25	3.16	5.11	9.78	15.75
Magnetization, Am^2/kg	4.9	13.1	18.8	31.9	45.3
Curie Temperature, K	66	122	162	236	377

Table 6.1: Magnetization and Curie temperature for different FePd alloys [118].

Previous research has found the Curie temperature of FePd to be 470°C for $Fe_{50}Pd_{50}$, 370°C for $Fe_{45}Pd_{55}$ and 320°C for $Fe_{40}Pd_{50}$ [116], which is verified in other work [117]. Another work [118] found the Curie temperature and magnetization for FePd alloys with different atomic percentages of Fe, with the results shown in Table 6.1. The magnetizations given here have different units since these magnetizations are in terms of the volume, rather than the mass, of the sample. These results show that as the iron content increases, so does both the Curie temperature and the magnetization.

6.4 Thermal Dynamics of Square Artificial Spin Ice

6.4.1 Higher Magnetization Materials

This sample had a Fe : Pd ratio of 1 : 1.9. AFM and MFM measurements were performed at room temperature after heating to higher temperatures and cooling down to room temperature, with temperatures of 50°C, between 80°C and 220°C in 20°C intervals, 230°C and 240°C for ASI of periods 450 nm, 500 nm, and 600 nm. Figures 6.4, 6.5 and 6.6 show a selection of the MFM images obtained for each lattice spacing as the vertices change type, with a brief guide to identifying the different vertex types given in figure 6.3.

Up to 220°C, this high Fe content sample exhibited no changes to the magnetic configurations for any of the periods – all vertices remained in their initial type 2 state. However, by 240°C the magnetic configurations abruptly changed such that 96 % of all vertices were in the ground state. At 230°C we can observe the way

in which the vertices start to change from a type 2 ordered state to the ground state. The vertices begin to split into rough bands of alternating type 1 and type 2 vertices. As the period decreases, the width of the type 2 bands increases, resulting in smaller ground state regions. This could be a result of stronger interactions between individual magnets for the smaller period, so that more energy is required to flip them from one type to another. However, by 240°C, the proportions of the different types of vertices are approximately equal for all the periods.

These results are presented graphically in figure 6.7. For added detail, we have split the type 2 states further into four different types, labelled 2(a) to 2(d); examples of each of these vertices are shown in figure 6.8. The vertices in this sample all started as type 2(d) vertices at room temperature. This splitting allows us to differentiate between vertices which have not changed, and those which have altered but have changed to a different type of type 2 vertex. This is the first time that the proportions of different types of type 2 vertices have been recorded as a function of temperature. For the high iron sample, this splitting offers little value since the vertices have predominantly changed straight from type 2(d) to type 1 (ground state).

We can now calculate the magnetization, M_S, of this sample at the blocking temperature. We use a blocking temperature of 230°C, since this is the temperature at which approximately half the vertices are no longer in their initial type 2 state and the equations used in section 6.4.1 to obtain a magnetization of 121000 A/m. This is far smaller than the 5.97×10^6 A/m measured at room temperature in the VSM.
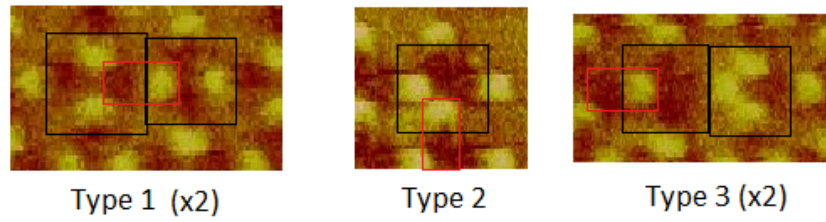
Figure 6.3: A guide to identifying the different types of vertices. Each magnet in an MFM image has a yellow end and a red end, to represent the north and south poles. Here we have examples of type 1, type 2 and type 3 vertices, with the vertices highlighted in a black box and one individual magnet in each image outlined in red. The two type 1 vertices shown here have alternating red and yellow ends at each vertex. A system containing arrays of type 1 vertices is in the ground state. The type 2 vertex also has two yellow ends and two red ends meeting at a point, but the colours do not alternate. Any rotationally symmetric version of this system would also be a type 2 vertex. There are two type 3 vertices shown here; type 3 vertices can also be called magnetic monopoles. In this example, one type 3 vertex has three yellow ends and one red end meeting at the vertex. The other vertex has three red ends and one yellow end. Once again, any rotationally symmetric version of this configuration would also be a type 3 vertex.

Figure 6.4: MFM images of the high Fe / low Pd sample for the 600 nm period for temperatures of (a) 220°C, (b) 230°C and (c) 240°C. There is a rapid change between the completely ordered type 2 state at 220°C and the predominantly ground state at 240°C. Each image is 15 μm square.

Figure 6.5: MFM images of the high Fe / low Pd sample for the 500 nm period for temperatures of (a) 220°C, (b) 230°C and (c) 240°C. Each image is 15 μm square. At 230°C the vertices appear to have formed approximate bands of type 2 and type 1 vertices.
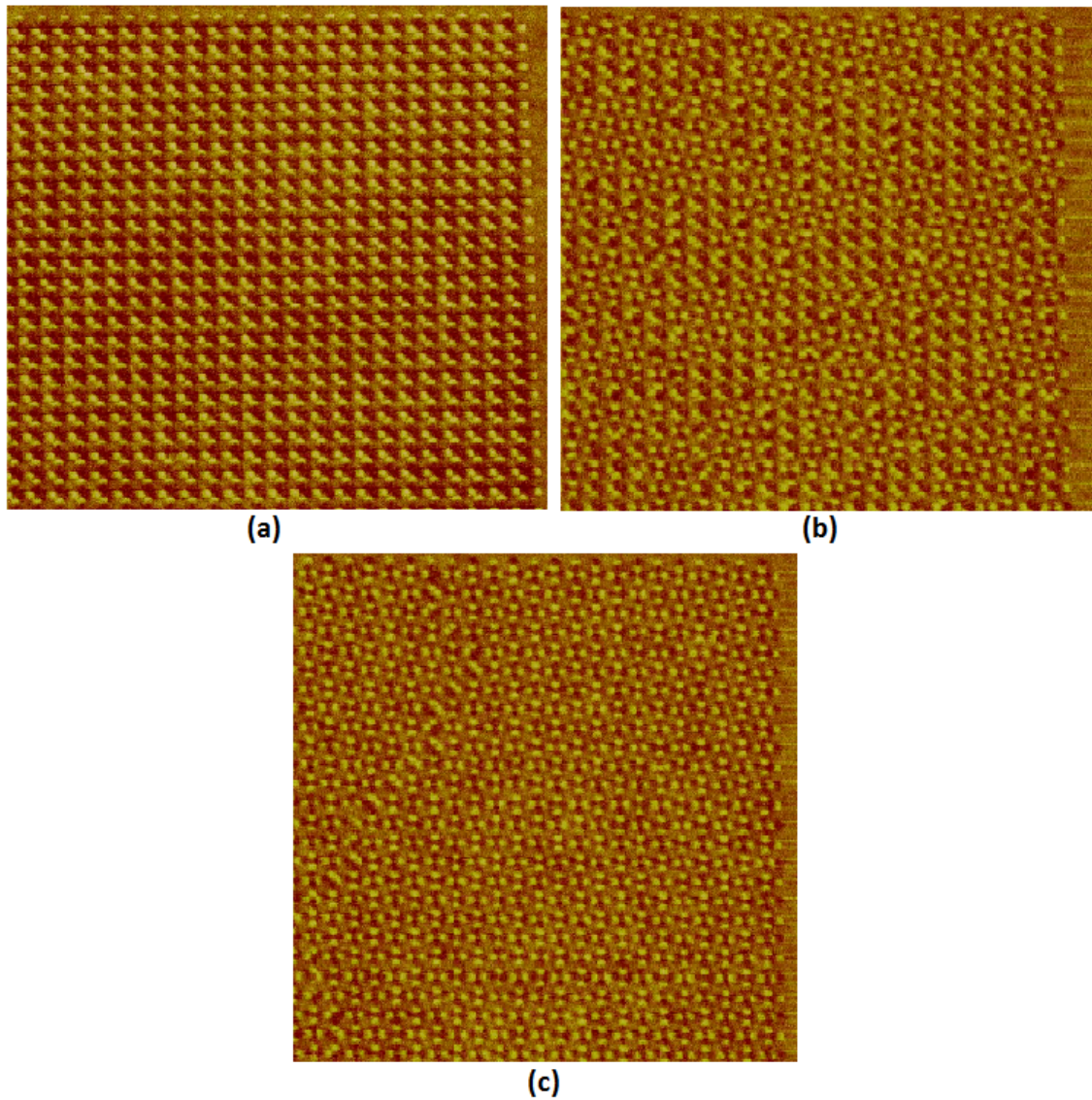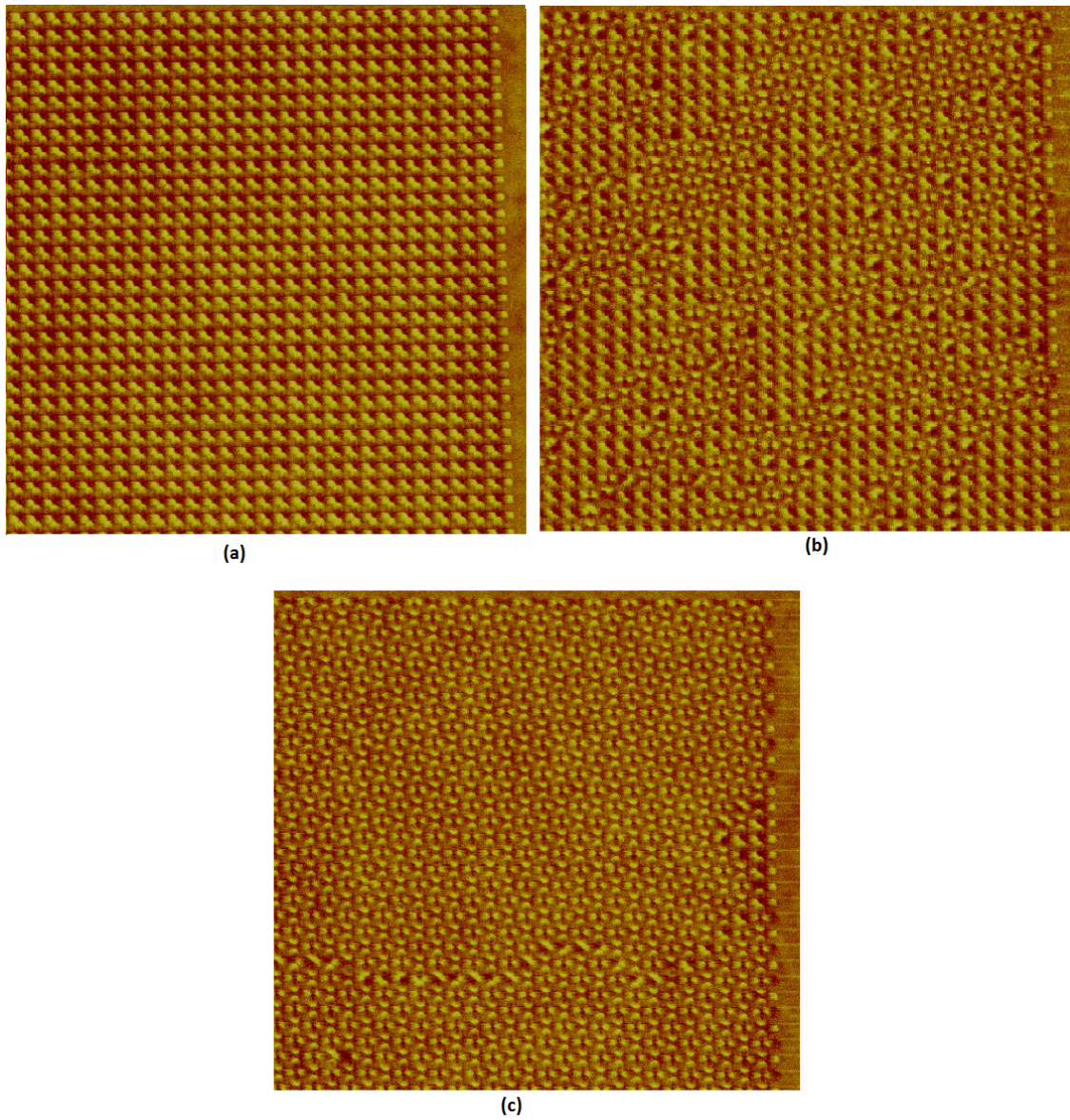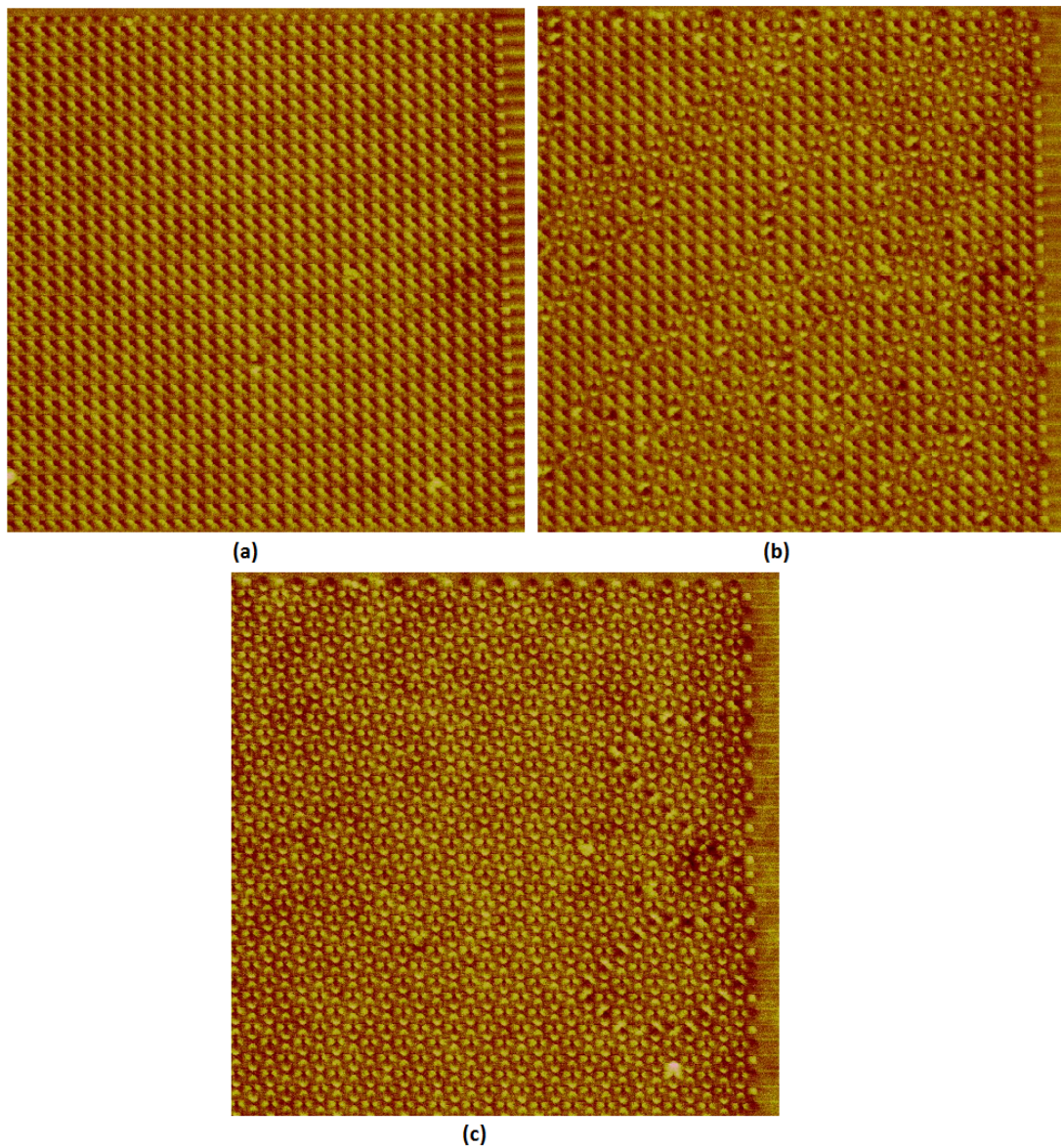
Figure 6.6: MFM images of the high Fe / low Pd sample for the 450 nm period for temperatures of (a) 220°C, (b) 230°C and (c) 240°C. Each image is 15 μm square. At 230°C the vertices have again formed alternating bands of type 1 and 2 vertices, with the type 2 bands broader than those observed in figure 6.5.
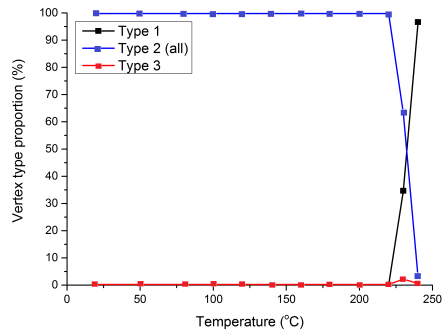
(a) 450 nm
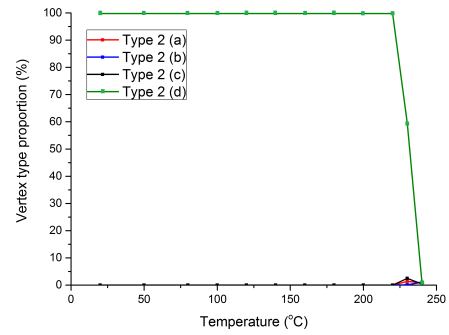
(b) Type 2 only
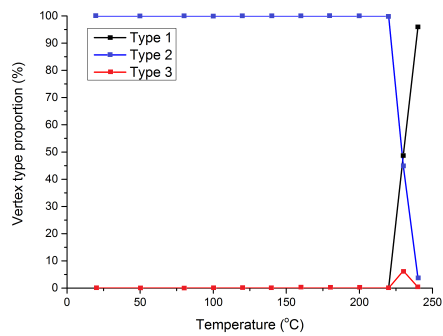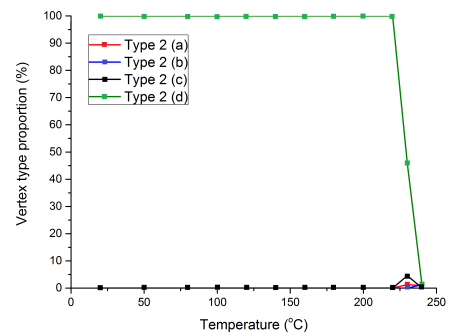
(c) 500 nm

(d)
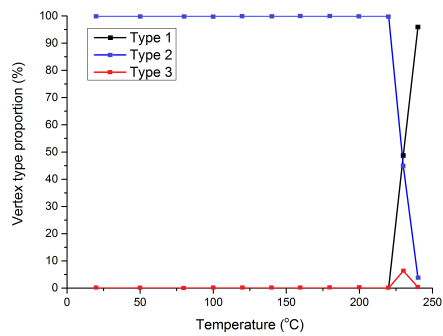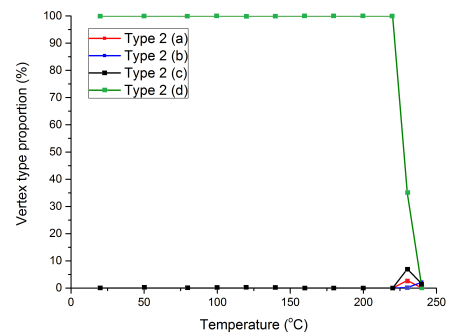
(e) 600 nm

(f)

Figure 6.7: Vertex proportions as a function of temperature for the higher magnetization. Figures (b), (d), and (f) focus on the variation of type 2 vertices for the 450 nm, 500 nm, and 600 nm periods respectively.
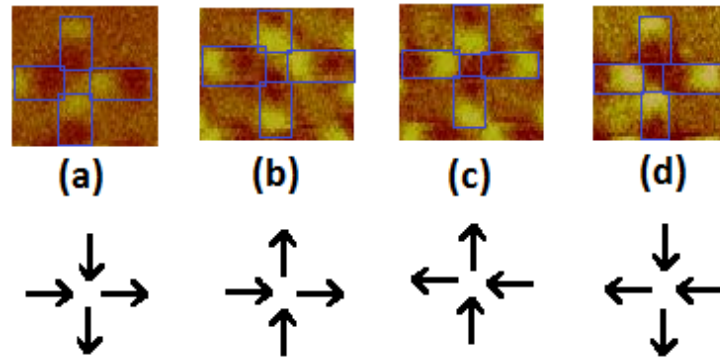
Figure 6.8: The four possible type 2 configurations, labelled 2(a) to 2(d). The individual nanomagnets are outlined in blue. The diagram also shows the configurations represented as Ising spins using arrows, where the arrowheads point towards the red end of each magnet.

6.4.2 Lower Magnetization Materials

This sample had a Fe : Pd ratio of 1 : 3.5. AFM and MFM measurements were performed at room temperature, 50°C, and between 80°C and 240°C in 20°C intervals for square ASI of periods 450 nm, 500 nm, and 600 nm. Figure 6.9 shows a selection of the MFM images obtained for the 600 nm period as the vertices change type. The low magnetization material did not form the bands of type 1 and 2 vertices that were observed in the high magnetization material. Instead, the vertices change in a more random manner as a result of the weaker interaction strength between the nanomagnets.

The results for the lower magnetization samples are presented graphically in figure 6.10. Here, the vertices begin to change at a lower temperature than for the high magnetization sample – at 140°C, rather than 230°C. However, even at 240°C these samples do not reach the ground state, instead becoming a mixture of type 1, 2 and 3 vertices. The lack of type 4 vertices shows that the magnets are still interacting and not a completely random arrangement, since we would expect 12.5 % of the vertices to be type 4 if they were non-interacting. We also observe little difference in the

results obtained for the various lattice spacings of the ASI.

We have once again split the type 2 vertices into each possible variation of a type 2 vertex. The vertices are all initially in the type 2(a) configuration. Between 140°C and 180°C there is a rapid decrease in the proportion of type 2(a) vertices, as their numbers fall to make up fewer than 10 % of the vertices. However, unlike the high magnetization sample, these vertices change to form a mixture of type 1, 2 and 3 vertices with no dominant preference. The proportion of type 2(a) vertices does start to increase and decrease again as the vertices fluctuate between their new and original states.

For this material, half of all vertices have changed from their initial state at a temperature of approximately 170°C – we use this value for our blocking temperature. Using the equations in section 6.4.1, we estimate the magnetization of this sample to be 114000 A/m, far lower than the 433,000 A/m that was experimentally determined at room temperature. As expected, this is also a smaller but similar value than the 121000 A/m obtained in the higher Fe content sample.

The difference in the behaviour of the two materials could be attributed to the different magnetizations at their blocking temperatures. It could be that the magnetization strength of the low Fe content material is too low to thermalize the sample and result in long-range ground state ordering. Instead, the vertices appear to form a random distribution of vertex types more akin to a system with the vertices acting individually rather than with collective long-range interactions. This is shown by the end result in which the vertex proportions tend towards a random distribution and Figure 6.8 does not show any significant areas where the vertices are ordered.
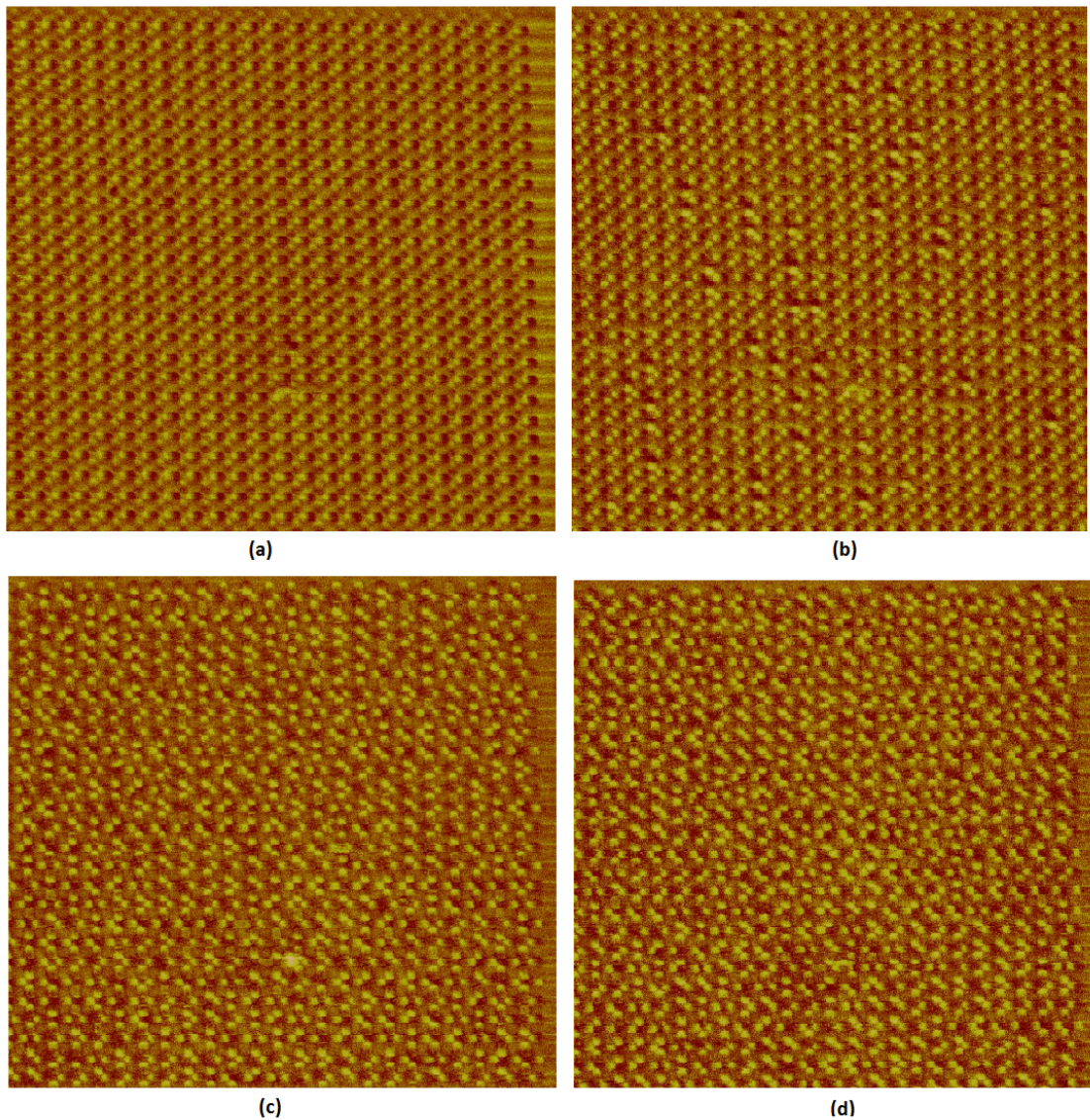
Figure 6.9: MFM images of the lower magnetization sample for the 600 nm period for temperatures of (a) room temperature, (b) 160°C, (c) 200°C and (d) 240°C. This sample starts to undergo thermal dynamical changes at lower temperatures than the high Fe sample, but does not reach the ground state at high temperatures. Each image is 15 μm square.

(a) 450nm

(b) Type 2 only

(c) 500nm

(d)

(e) 600nm

(f)

Figure 6.10: Vertex proportions as a function of temperature for the low Fe / high Pd sample. Figures (b), (d), and (f) focus on the variation of type 2 vertices for the 450 nm, 500 nm, and 600 nm periods respectively.

The remanent magnetization can be obtained by choosing a direction and assigning a value of +1 to all nanomagnets pointing in that direction, and similarly for an orthogonal direction. All nanomagnets pointing in opposite directions to the assigned directions are valued at -1. Any vertices in the ground state will have a remanent magnetization of 0, so for a system consisting of mostly ground state vertices, the remanent magnetization can be obtained by just considering the magnetization of defects and domain walls. For the high Fe content sample, arrows pointing up and to the right were assigned the value of +1 such that the vertex 2d, as shown in Figure 6.8, would have a remanent magnetization value of +4. For the low Fe content sample, arrows pointing upwards and to the left were assigned values of +1, such that the vertex 2a would have a remanent magnetization value of +4. By assigning the directions in this manner, both the high and low Fe content samples commence the experiment with their maximum remanent magnetization values.

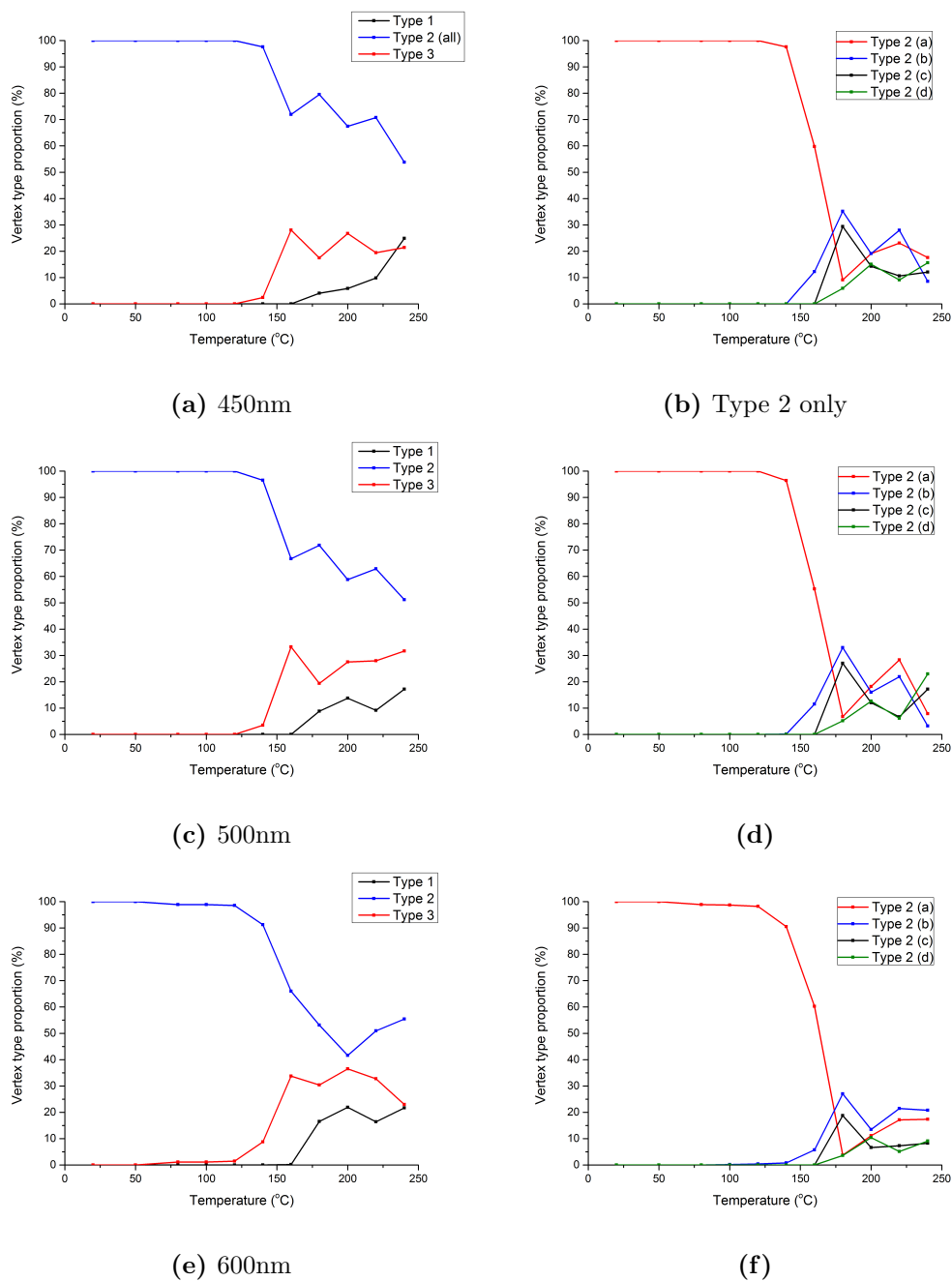The remanent magnetization values as a function of temperature are shown in Figure 6.11 for the 600 nm period. This period has been chosen to be representative of all the periods, given that there was little variation with temperature of the changes between different vertex types for each different period. The high Fe sample shows a steep decline in the remanent magnetization from its value at +1160 at 220°C when the system is ordered as type 2d vertices to a value of -26 at 240°C when the vertices are mostly in the ground state. For a perfect ground state system, the remanent magnetization would be zero. The low Fe sample shows a sharp decrease in the remanent magnetization at 180° when the remanent magnetization falls to -160 from +736. This coincides with the sharp fall of type 2a vertices at this temperature in Figure 6.10 and the increase in the proportion of type 2c vertices, which have a remanent magnetization of -4 since all the spins point in the opposite direction to the spins of type 2a vertices. The remanent magnetization increases again between 180°C and 200°C when the proportion of type 2a vertices rises.

Figure 6.12 shows how the vertex types can transition from one to another, and explains how the proportion of type 2a vertices in Figure 6.10 can increase and

decrease in a zigzag fashion as the temperature increases. Starting from a type 2a vertex, flipping any one magnet produces a type 3 vertex. When any one magnet from the type 3 vertex is then flipped, one of four vertex states is possible. Figure 6.12 shows that the possible vertices are a type 4 vertex, a type 2b vertex, a type 1 vertex, or returning back to a type 2a vertex. This explains why, in Figure 6.10, type 3 vertices are the first vertices that are formed when the type 2a vertices start to decrease in number. Type 2b vertices also begin to appear before other type 2 vertices for the same reason.
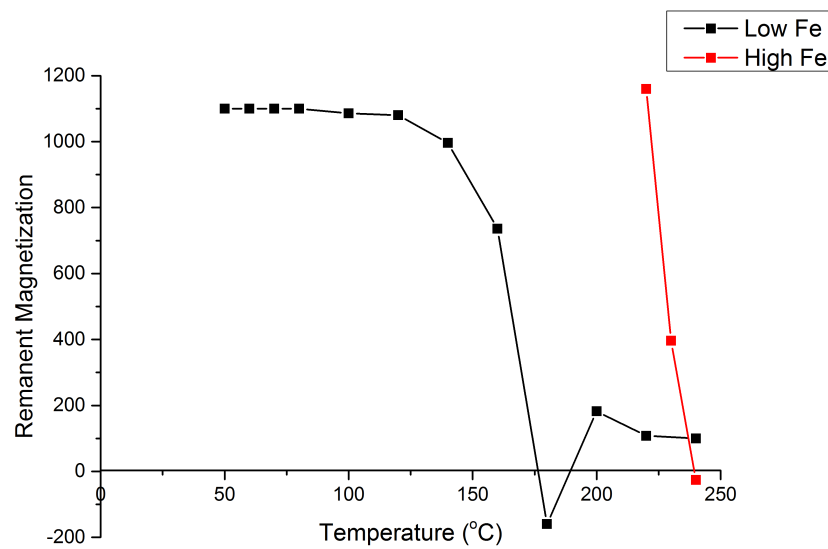
Figure 6.11: The remanent magnetization as a function of temperature for the high Fe and low Fe content samples with a 600 nm period. The high Fe sample shows a steep decline in remanent magnetization between the ordered type 2d vertices and the ground state vertices at 240°. The low Fe sample shows a more gradual change, although at 180°C there is a sharp decrease in the remanent magnetization, which corresponds to the decline in type 2a vertices shown in figure 6.10.
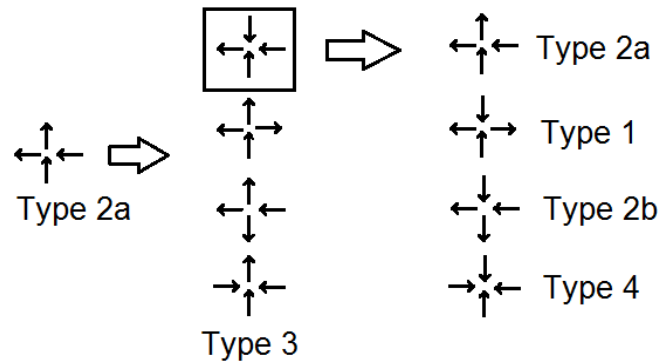
Figure 6.12: The transitions between different vertex types, commencing with a type 2a vertex. Flipping any one magnet results in a type 3 vertex, so the system has one less type 2a vertex but gains a type 3 vertex. Using the top type 3 vertex as an example, flipping any one of these magnets results in a different vertex type. The vertex can revert back to being a type 2a vertex, resulting in the zigzag shape seen in Figure 6.10 as the system gains a type 2a vertex. The type 3 vertex may change instead to a type 2b vertex, a ground state type 1 vertex, or a type 4 vertex. However, the type 4 vertices are unlikely to occur since this state requires more energy than the other states.

6.5 Summary

This chapter commenced with an overview of the fabrication process used to make these devices. VSM measurements were then performed on thin film sheets of our different FePd alloys from which we obtained the magnetizations of these materials at room temperature. We calculated the theoretical blocking temperatures of the materials but, owing to the limitations of the method used, our results were inaccurate by four orders of magnitude.

Measurements to record the thermal dynamics of the samples were taken using MFM. The samples were incrementally heated to higher temperatures and MFM measurements were performed after each temperature. The low magnetization and high magnetization samples showed very different behaviour upon heating. The low magnetization sample started to flip the magnetic moments at lower temperatures,

after which the vertices gradually changed to a mixture of types 1, 2, and 3. The high magnetization sample required a much higher temperature before any changes started to occur. However, the vertices then rapidly changed to form a long-range ground state configuration. We presented the first graphs demonstrating exactly how the proportions of each vertex configuration change as the samples thermalize.

Finally, we discussed the blocking temperature and the magnetization at this temperature for both materials.

Chapter 7

Conclusion

7.1 Summary

This thesis has extended the work previously carried out on hybrid semiconductor / ferromagnetic devices and incorporated the study of the transport properties of combined 2DEG / ASI structures into this field.

We have provided an indepth analysis of the effects of piezoelectric strain on the longitudinal resistance of a 2DEG. Strain manifests itself as electric commensurability oscillations which, for our samples, dominated the low-field oscillations and thus prevented the observation of magnetic COs. We showed that these acted on a period of 200 nm, corresponding to the width of the ferromagnetic stripes, so were caused by stress arising at the edges of the stripes.

We tried two methods to minimize the effects of strain – increasing the temperature, and realigning the stripes with respect to the wafer axes. Increasing the temperature was shown to be an ineffective method of minimizing strain, with the magnitude of the strain oscillations being largely independent of temperature. However, by realigning the stripes normal to the [100] axis, rather than the [111] axis, we were able to minimize the strain COs to the extent that magnetic COs could be observed.

Next, we measured the transport properties of combined 2DEG / ASI structures

and observed magnetic COs in the longitudinal resistance of the 2DEG. The locations of the oscillation minima and maxima were found to be dependent upon the length of the ASI elements rather than the period of the ASI. The COs were shown to become smaller in magnitude as the temperature increased. The angle of the applied magnetic field was found to have little effect on the COs for our sample owing to the depth of the 2DEG beneath the ASI. We also showed that the Hall resistance was not affected by the presence of the ASI arrays. However, we cannot be certain that these oscillations are due to the magnetic properties of the ASI, rather than the piezoelectric strain between the GaAs-AlGaAs wafer and the ASI elements. The oscillations being dependent upon the width, rather than the period, of the elements suggests that the oscillations may have a piezoelectric strain origin akin to the results obtained in chapter 4.

Finally, we investigated how the material composition and period of ASI affects their thermal dynamical properties. For this experiment, we used a SiO_2 wafer rather than a semiconducting substrate since there was no need to perform resistance measurements. We showed that the period of our arrays had little effect on either the temperature at which thermally-activated magnetization dynamics begins to occur, or on how the vertices change from one type to another as the ASI thermalizes.

We compared two different FePd alloys, one with a magnetization approximately 1.4 times the size of the other. The lower magnetization sample underwent slow, gradual thermal dynamical changes. Whilst the nanomagnets in this sample began to flip at temperatures 90°C lower than the high magnetization sample, it did not reach an overall ground state at the maximum tested temperature of 240°C. However, the high magnetization material underwent an abrupt change from an ordered state to the ground state.

7.2   Future Work

There is plenty of scope for future work based upon the results contained within this thesis. First, the origin of the observed commensurability oscillations needs to be ascertained, so that we can be confident that magnetic commensurability oscillations are present. To enhance the strength of the COs in the combined 2DEG / ASI structures, the transport measurements could be repeated on a wafer containing a shallower 2DEG to provide a stronger magnetic field at the 2DEG. The work by Nogaret *et. al.* showed there to be an angular dependence on the magnitude of the COs for ferromagnetic stripes [10], a phenomenon that was not witnessed in our samples. If we were to use a shallower 2DEG, we could then attempt to strengthen the ASI COs by altering the angle of applied magnetic field.

Enhancing the clarity of the COs will open up further avenues of research in this field. The vertices of the square ASI could be arranged into ordered, random, or ground states and the effects of the different resulting magnetic fields on 2DEG's transport properties could be investigated.

Furthermore, there is no need to limit this study to just square ASI. Combined 2DEG / kagome ASI structures could also be an interesting avenue of research. Unlike in square ASI, the kagome form has a net magnetic charge at every vertex. It could be interesting to see the effects that this has on the transport properties of a 2DEG, and to make comparisons between these two forms of ASI.

Regarding the thermal dynamics of ASI studies, further work could be undertaken on materials with a wider range of Fe/Pd ratios. With such different results obtained for the two materials studied, it could be interesting to see how the progression occurs from the abruptly changing high magnetization sample to the low magnetization sample that does not reach the ground state. The thermal dynamics of kagome and penrose ASI are also yet to be researched in this manner.

References

[1] W. Shockley and G. L. Pearson, "Modulation of conductance of thin films of semi-conductors by surface charges," *Phys. Rev.*, vol. 74, pp. 232–233, (1948).

[2] K. von Klitzing *et al.*, "New method for high-accuracy determination of the fine-structure constant based on quantized hall resistance," *Phys. Rev. Lett*, vol. 45, pp. 494–497, (1980).

[3] D. C. Tsui *et al.*, "Two-dimensional magnetotransport in the extreme quantum limit," *Phys. Rev. Lett*, vol. 48, p. 1559, (1982).

[4] R. B. Laughlin, "Anomalous quantum hall effect: an incompressible quantum fluid with fractionally charge excitations," *Phys. Rev. Lett*, vol. 50, p. 1395, (1983).

[5] J. P. Eisenstein and H. L. Stormer, "The fractional quantum Hall effect," *Science*, vol. 248, pp. 1510–1516, (1990).

[6] R. F. Wang *et al.*, "Artificial spin ice in a geometrically frustrated lattice of nanoscale ferromagnetic islands," *Nature*, vol. 439, pp. 303–306, (2006).

[7] W. F. Giauque and J. W. Stout, "The entropy of water and the third law of thermodynamics. The heat capacity of ice from 15 to 273K," *Journal of the American Chemical Society*, vol. 58, pp. 1144–1150, (1936).

[8] C. Castelnovo *et al.*, "Magnetic monopoles in spin ice," *Nature*, vol. 451, pp. 42–45, (2008).

[9] S. T. Bramwell *et al.*, "Measurement of the charge and current of magnetic monopoles in spin ice," *Nature*, vol. 461, pp. 956–960, (2009).

[10] A. Nogaret *et al.*, "Observation of giant magnetoresistance due to open orbits in hybrid semiconductor/ferromagnetic devices," *Phys. Rev. B.*, vol. 55, pp. 16037–16040, (1997).

[11] P. D. Ye *et al.*, "Fabrication and characterization of micromagnet arrays on top of GaAs/AlGaAs heterostructures," *Appl. Phys. Lett.*, vol. 67, pp. 1441–1443, (1995).

[12] M. Johnson *et al.*, "Hybrid Hall effect device," *Appl. Phys. Lett.*, vol. 71, pp. 974–976, (1997).

[13] B. L. Gallagher *et al.*, "Electrical transport of 2D electrons in non-uniform magnetic fields," *Physica E.*, vol. 11, pp. 171–176, (2001).

[14] C. W. J. Beenakker and H. van Houten, "Quantum transport in semiconductor nanostructures," *Solid state physics.*, pp. 1–228, (1991).

[15] C. Berger *et al.*, "Ultrathin epitaxial graphite: 2D electron gas properties and a route towards graphene-based nanoelectronics," *J. Phys. Chem.*, vol. 108, pp. 19912–19916, (2004).

[16] R. Fletcher *et al.*, "Thermoelectric and hot-electron properties of a silicon inversion layer," *Phys. Rev. B.*, vol. 56, pp. 12422–12428, (1997).

[17] T. Ando *et al.*, "Electronic properties of two-dimensional systems," *Reviews of Modern Physics*, vol. 54, pp. 437–672, (1982).

[18] F. F. Fang *et al.*, "Effective mass and collision time of (100) Si surface electrons," *Phys. Rev. B*, vol. 16, pp. 4446–4454, (1977).

[19] F. Stern and W. E. Howard, "Properties of semiconductor surface inversion layers in the electric quantum limit," *Phys. Rev.*, vol. 163, pp. 816–835, (1967).

[20] H. L. Stormer *et al.*, "Two-dimensional electron gas at a semiconductor-semiconductor interface," *Solid State Comms.*, vol. 29, pp. 705–709, (1979).

[21] C. H. W. Barnes, "Quantum electronics in semiconductors," *Cambridge University Press*, (2004).

[22] D. G. Schlom *et al.*, "Oxide electronics: Upward mobility rocks!," *Nature Materials*, vol. 9, p. 3, (2010).

[23] N. A. Dodoo-Amoo, "The nature of critical phenomena of the scaling theory of quantum Hall transitions in two-dimensional electron systems," *PhD thesis: University of Leeds*, (2013).

[24] D. K. Mistry, "On chip THz studies of low-dimensional semiconductor systems," *PhD thesis: University of Leeds*, (2013).

[25] R. Dingle *et al.*, "Electron mobilities in modulation-doped semiconductor heterojunction superlattices," *Appl. Phys. Lett.*, vol. 33, pp. 665–667, (1978).

[26] H. L. Stormer *et al.*, "Influence of an undoped (AlGa)As spacer on mobility enhancement in GaAs-(AlGa)As superlattices," *Appl. Phys. Lett.*, vol. 38, pp. 691–693, (1981).

[27] M. U. Shaukat, "Microwave and terahertz studies of the electron dynamics in two-dimensional electron systems," *PhD thesis: University of Leeds*, (2012).

[28] E. H. Hall, "On a new action of the magnet on electric currents," *J. Am. Math.*, vol. 2, pp. 287–292, (1879).

[29] A. Tzalenchuk *et al.*, "Towards a quantum resistance standard based on epitaxial graphene," *Nature Nano.*, vol. 5, pp. 186–189, (2010).

[30] W. F. Giauque and M. F. Ashley, "Molecular rotation in ice at 10K. Free energy of formation and entropy of water," *Phys. Rev.*, vol. 43, pp. 81–82, (1933).

[31] L. Pauling, "The structure and entropy of ice and of other crystals with some randomness of atomic arrangement," *Journal of the American Chemical Society*, vol. 57, pp. 2680–2684, (1935).

[32] J. D. Bernal and R. H. Fowler, "A theory of water and ionic solution, with particular reference to hydrogen and hydroxyl ions," *J. Chem. Phys.*, vol. 1, pp. 515–548, (1933).

[33] S. T. Bramwell and M. J. Harris, "Frustration in Ising-type spin models on the pyrochlore lattice," *J. Phys.: Condens. Matter*, vol. 10, pp. 215–220, (1998).

[34] M. J. Harris *et al.*, "Geometrical frustration in the ferromagnetic pyrochlore $Ho_2Ti_2O_7$," *Phys. Rev. Lett.*, vol. 79, pp. 2554–2557, (1997).

[35] A. P. Ramirez *et al.*, "Zero point entropy in 'spin ice'," *Nature*, vol. 399, pp. 333–335, (1999).

[36] S. T. Bramwell *et al.*, "Spin correlations in $Ho_2Ti_2O_7$: A dipolar spin ice system," *Phys. Rev. Lett.*, vol. 87, pp. 047205 1–4, (2001).

[37] T. F. Fennell *et al.*, "Neutron scattering investigation of the spin ice state in $Dy_2Ti_2O_7$," *Phys. Rev. B.*, vol. 70, pp. 134408 1–7, (2004).

[38] H. Kadowaki *et al.*, "Neutron scattering study of dipolar spin ice $Ho_2Sn_2O_7$: Frustrated pyrochlore magnet," *Phys. Rev. B.*, vol. 65, pp. 144421 1–8, (2002).

[39] S. T. Bramwell and M. J. P. Gingras, "Spin ice state in frustrated magnetic pyrochlore materials," *Science*, vol. 294, pp. 1495–1501, (2001).

[40] J. Snyder *et al.*, "How 'spin ice' freezes," *Nature*, vol. 413, pp. 48–51, (2001).

[41] P. M. Dirac, "Quantised singularities in the electromagnetic field," *Proc. R. Soc. A.*, vol. 133, pp. 60–72, (1931).

[42] K. A. Milton, "Theoretical and experimental status of magnetic monopoles," *Rep. Prog Phys.*, vol. 69, pp. 1637–1712, (2006).

[43] D. J. P. Morris *et al.*, "Dirac strings and magnetic monopoles in the spin ice $Ho_2Ti_2O_7$," *Science*, vol. 326, pp. 411–414, (2009).

[44] E. Mengotti *et al.*, "Real-space observation of emergent magnetic monopoles and associated Dirac strings in artificial kagome spin ice," *Nature Phys.*, vol. 7, pp. 68–74, (2011).

[45] S. Ladak *et al.*, "Direct observation of magnetic monopole defects in an artificial spin-ice system," *Nature Phys.*, vol. 6, pp. 359–363, (2010).

[46] L. D. C. Jaubert and P. C. W. Holdsworth, "Signature of magnetic monopole and Dirac string dynamics in spin ice," *Nature Phys.*, vol. 5, pp. 258–261, (2009).

[47] S. D. Pollard *et al.*, "Propagation of magnetic charge monopoles and Dirac flux in an artificial spin-ice lattice," *Phys. Rev. B*, vol. 85, p. 180402, (2012).

[48] R. C. Silva *et al.*, "Nambu monopoles interacting with lattice defects in a two-dimensional artificial square spin ice," *Phys. Rev. B.*, vol. 87, p. 014414, (2013).

[49] S. R. Giblin *et al.*, "Creation and measurement of long-lived magnetic monopole currents in spin ice," *Nature Phys.*, vol. 7, pp. 252–258, (2011).

[50] Y. Qi *et al.*, "Direct observation of the ice rule in an artificial kagome spin ice," *Phys. Rev. B*, vol. 77, p. 094418, (2008).

[51] J. P. Morgan *et al.*, "Thermal ground-state ordering and elementary excitations in artificial magnetic square ice," *Nature Phys.*, vol. 7, pp. 75–79, (2011).

[52] S. Zhang *et al.*, "Crystallites of magnetic charges in artificial spin ice," *Nature*, vol. 500, pp. 553–557, (2013).

[53] M. Tanaka *et al.*, "Magnetic interactions in a ferromagnetic honeycomb nanoscale network," *Phys. Rev. B.*, vol. 73, p. 052411, (2006).

[54] J. P. Morgan *et al.*, "Real and effective thermal equilibrium in artificial square spin ices," *Phys. Rev. B*, vol. 87, p. 024405, (2013).

[55] J. M. Porro *et al.*, "Exploring thermally induced states in square artificial spin-ice arrays," *New J. Phys.*, vol. 15, p. 055012, (2013).

[56] A. Farhan *et al.*, "Direct observation of thermal relaxation in artificial spin ice," *Phys. Rev. Lett.*, vol. 111, p. 057204, (2013).

[57] V. Kapaklis *et al.*, "Thermal fluctuations in artificial spin ice," *Nature nano.*, vol. 8, pp. 514–519, (2014).

[58] J. Drisko *et al.*, "Fepd$_3$ as a material for studying thermally acive artificial spin ice systems," *Phys. Rev. B.*, vol. 91, p. 224406, (2015).

[59] V. Kubrak *et al.*, "Magnetoresistance and Hall magnetometry of single submicron ferromagnetic structures," *J. Appl. Phys*, vol. 87, pp. 5986–5988, (2000).

[60] V. Kubrak *et al.*, "The transport of 2D electrons through magnetic barriers," *Physica E*, vol. 7, pp. 997–1000, (2000).

[61] A. K. Geim *et al.*, "Ballistic Hall micromagnetometry," *Appl. Phys. Lett.*, vol. 71, pp. 2379–2381, (1997).

[62] F. M. Peeters and P. Vasilopoulos, "Quantum transport of a two-dimensional electron gas in a spatially modulated magnetic field," *Phys. Rev. B.*, vol. 47, pp. 1466–1473, (1993).

[63] R. R. Gerhardts, "Quasiclassical calculation of magnetoresistance oscillations of a two-dimensional electron gas in spatially periodic magnetic and electrostatic fields," *Phys. Rev. B.*, vol. 53, pp. 11064–11075, (1996).

[64] P. Vasilopoulos and F. M. Peeters, "Periodic magnetic modulation of a two-dimensional electon gas: Transport properties," *Superlatt. Microstruc.*, vol. 7, pp. 393–395, (1990).

[65] C. W. J. Beenakker, "Guiding-center-drift resonance in a periodically modulated two-dimensional electron gas," *Phys. Rev. Lett.*, vol. 62, pp. 2020–2023, (1989).

[66] K. W. Edmonds *et al.*, "Magnetoresistance oscillations due to internal landau band structure of a two-dimensional electron system in a periodic magnetic field," *Phys. Rev. B.*, vol. 64, p. 041303, (2001).

[67] R. R. Gerhardts *et al.*, "Novel magnetoresistance oscillations in a periodically modulated two-dimensional gas," *Phys. Rev. Lett.*, vol. 62, p. 1177, (1989).

[68] A. Nogaret, "Electron dynamics in inhomogeneous magnetic fields," *J. Phys.: Condens. Matter*, vol. 22, p. 253201, (2010).

[69] P. D. Ye *et al.*, "Electrons in a periodic magnetic field induced by a regular array of micromagnets," *Phys. Rev. Lett.*, vol. 74, pp. 3013–3017, (1995).

[70] R. R. Gerhardts *et al.*, "Magnetoresistance oscillations in a grid potential: Indication of a Hofstadter-type energy spectrum," *Phys. Rev. B.*, vol. 43, pp. 5192–5195, (1990).

[71] D. E. Grant *et al.*, "Commensurability oscillations due to pinned and drifting orbits in a two-dimensional lateral surface superlattice," *Phys. Rev. B.*, vol. 61, pp. 13127–13130, (2000).

[72] D. Pfannkuche and R. R. Gerhardts, "Theory of magnetotransport in two-dimensional electron systems subjected to weak two-dimensional superlattice potentials," *Phys. Rev. B.*, vol. 46, pp. 12606–12626, (1992).

[73] P. D. Ye *et al.*, "Magnetoresistance oscillations induced by periodically arranged micromagnets," *J. Appl. Phys.*, vol. 81, pp. 5444–5448, (1997).

[74] R. J. Winkler *et al.*, "Landau band conductivity in a two-dimensional electron system modulated by an artificial one-dimensional superlattice potential," *Phys. Rev. Lett.*, vol. 62, p. 1173, (1989).

[75] A. W. Rushforth *et al.*, "Anisotropic magnetoresistance in a two-dimensional electron gas in a quasi-random magnetic field," *Phys. Rev. B.*, vol. 70, p. 193313, (2004).

[76] A. Nogaret *et al.*, "Giant magnetoresistance and hysteretic effects in hybrid semiconductor/ferromagnet devices," *Physica E*, vol. 2, pp. 421–425, (1998).

[77] N. Overend *et al.*, "Giant magnetoresistance and possible miniband effects in periodic magnetic fields," *Physica B*, vol. 249-251, pp. 326–329, (1998).

[78] N. Overend *et al.*, "Temperature dependence of large positive magnetoresistance in hybrid ferromagnetic/semiconductor devices," *Appl. Phys. Lett.*, vol. 72, pp. 1724–1726, (1998).

[79] H. L. Carmona *et al.*, "Two-dimensional electrons in a lateral magnetic superlattice," *Surface science*, vol. 361, pp. 328–332, (1995).

[80] M. Pohlit *et al.*, "Nanocluster building blocks of artificial square spin ice: stray-field studies of thermal dynamics," *J. Appl. Phys.*, vol. 117, p. 17C746, (2015).

[81] M. Pohlit *et al.*, "Magnetic stray-field studies of a single cobalt nanoelement as a component of the building blocks of artificial square spin ice," *J. Magnetism and Magnetic Materials.*, vol. 400, pp. 206–212, (2015).

[82] A. Y. Cho and J. R. Arthur, "Molecular beam epitaxy," *Progress in Solid State Chemistry*, vol. 10, pp. 157–191, (1975).

[83] I. Haller *et al.*, "High resolution postive resists for electon-beam exposure," *IBM J. Res. Dev.*, vol. 12, p. 251, (1968).

[84] M. Hatzakis, "Electron resists for microcircuit and mask production," *J. Electrochem. Soc.:Electrochemical Technology*, vol. 116, p. 1033, (1969).

[85] H. Y. Ku and L. C. Scala, "Polymeric electron beam resists," *J. Electrochem. Soc.: Solid State Science*, vol. 116, p. 980, (1969).

[86] C. Vieu, "Electron beam lithography: resolution limits and applications," *Appl. Surface. Science*, vol. 164, pp. 111–117, (2000).

[87] J. P. Morgan, "Ordering and defects in artificial magnetic square ice: thermodynamic and field-driven processes," *PhD thesis: University of Leeds*, (2011).

[88] D. McMullan, "Scanning electron microscopy 1928-1965," *Scanning*, vol. 17, pp. 175–185, (1995).

[89] E. H. Synge, "A suggested method for extending microscopic resolution into the ultra-microscopic region," *Phil. Mag.*, vol. 6, pp. 356–362, (1928).

[90] G. Binnig *et al.*, "Atomic force microscope," *Phys. Rev. Lett.*, vol. 56, pp. 930–933, (1986).

[91] G. Binnig *et al.*, "Surface studies by scanning tunneling microscopy," *Phys. Rev. Lett.*, vol. 49, pp. 57–61, (1982).

[92] Y. Martin and H. K. Wickramasinghe, "Magnetic imaging by 'force microscopy' with 1000 Å resolution," *Appl. Phys. Lett.*, vol. 50, pp. 1455–1457, (1987).

[93] J. Mamin *et al.*, "Magnetic force microscopy of thin permalloy films," *Appl. Phys. Lett.*, vol. 55, pp. 318–320, (1989).

[94] N. A. Porter, "Magnetoresistance in n-type silicon," *PhD thesis: University of Leeds*, (2010).

[95] J. Klem *et al.*, "Persistent photoconductivity in (Al,Ga)As/GaAs modulation doped structures: Dependence on structure and growth temperature," *J Appl. Phys.*, vol. 54, pp. 5214–5217, (1983).

[96] J. Li *et al.*, "Two-dimensional electron gas in AlGaN/GaN heterostructures," *J. Vac. Sci. Technol.*, vol. 15, pp. 1117–1120, (1997).

[97] H. Wei *et al.*, "Persistent photoconductivity and the quantized Hall effect in In0.53Ga0.47As/InP heterostructures," *Appl. Phys. Lett.*, vol. 45, pp. 666–668, (1984).

[98] D. Lang and R. Logan, "Large-lattice-relaxation model for persistent photoconductivity in compound semiconductors," *Phys. Rev. Lett.*, vol. 39, pp. 635–639, (1977).

[99] D. E. Lacklison *et al.*, "A comparison of photoconduction effects in (Al, Ga)As and GaAs/(Al, Ga)As heterostructures," *Semicond. Sci. Technol.*, vol. 3, pp. 633–640, (1988).

[100] R. Fletcher *et al.*, "Persistent photoconductivity and two-band effects in GaAs-$Al_xGa_{1-x}As$ heterojunctions," *Phys. Rev. B.*, vol. 41, pp. 649–666, (1990).

[101] N. G. Semaltianos *et al.*, "Deep-level defects responsible for persistent photoconductivity in Ga-doped $Cd_{1-x}Mn_xTe$," *Phys. Rev. B*, vol. 51, pp. 17499–17505, (1995).

[102] P. M. Mooney, "Electrical properties of DX centers in GaAs and AlGaAs," *Radiation effects and defects in solids*, vol. 111, pp. 281–298, (1989).

[103] H. L. Carmona *et al.*, "Two-dimensional electrons in a lateral magnetic superlattice," *Phys. Rev. Lett.*, vol. 74, pp. 3009–3012, (1995).

[104] S. Izawa *et al.*, "Magnetoresistance oscillation in two-dimensional electron gas under spatially modulated magnetic field," *Jpn. J. Appl. Phys.*, vol. 34, pp. 4306–4308, (1995).

[105] R. Yagi and Y. Iye, "Oscillatory magnetoresistance in two-dimensional electron systems in a periodically modulated magnetic field," *Jpn. J. Appl. Phys.*, vol. 62, pp. 1279–1285, (1993).

[106] J. H. Davies and I. A. Larkin, "Theory of potential modulation in lateral surface superlattices," *Phys. Rev. B.*, vol. 49, pp. 4800–4812, (1994).

[107] P. D. Ye *et al.*, "Strain-induced magnetoresistance oscillations in GaAs-AlGaAs heterojunctions with ferromagnetic and superconducting submicrometre gratings," *Semicond. Sci. Tech.*, vol. 10, pp. 715–719, (1995).

[108] P. H. Beton *et al.*, "Effects of atomic ordering on the Curie temperature of FePd L1$_0$ type alloys," *J. Appl. Phys.*, vol. 42, pp. 9689–9692, (1990).

[109] E. Skuras *et al.*, "Anisotropic piezoelectric effect in lateral surface superlattices," *Appl. Phys. Lett.*, vol. 70, pp. 871–873, (1997).

[110] I. A. Larkin *et al.*, "Theory of potential modulation in lateral surface superlattices. II. Piezoelectric effect," *Phys. Rev. B.*, vol. 56, pp. 242–251, (1997).

[111] A. Aharoni, "Demagnetizing factors for rectangular ferromagnetic prisms," *J. Appl. Phys.*, vol. 83, pp. 3432–3434, (1998).

[112] A. A. Bykov *et al.*, "Hall effect in a spatially fluctuating magnetic field with zero mean," *Phys. Rev. B.*, vol. 61, pp. 5505–5510, (2000).

[113] S. A. Morley, "The dynamics of artificial spin ice in real and reciprocal space," *PhD thesis: University of Leeds*, (2015).

[114] H. Kiessig, "Interference of x-rays in thick layers," *Annalen Der Physik.*, vol. 10, p. 769, (1931).

[115] J. A. Osborn, "Demagnetizing factors of the general ellipsoid," *Phys. Rev.*, vol. 67, pp. 351–357, (1945).

[116] L. Wang *et al.*, "Temperature dependence of magnetoresistance oscillations in a two-dimensional electron gas subjected to a periodic potential," *Phys. Rev. B*, vol. 95, pp. 7483–7485, (2004).

[117] J. Lyubina *et al.*, "Phase transformations and magnetic structure of nanocrystalline Fe-Pd and Co-Pt alloys studied by in situ neutron powder diffraction," *J. Appl. Phys*, vol. 105, p. 07A717, (2009).

[118] J. Crangle, "Ferromagnetism in Pd-rich palladium-iron alloys," *Phil. Mag.*, vol. 5, pp. 335–342, (1960).